University of Derby

COLLEGE OF SCIENCE AND ENGINEERING

STRANGENESS PRODUCTION ANALYSIS IN SIMULATED PROTON-PROTON COLLISIONS AT THE LHC WITH THE NEW ALICE RUN 3 COMPUTING ENVIRONMENT

Aimeric LANDOU

A submission in partial fulfillment of the requirements of the University of Derby for the award of the degree of Doctor of Philosophy

SUPERVISOR:

Dr. Lee BARNBY

November 2018 – August 2022

Preface

This thesis was written solely by me. My contribution to the ALICE collaboration was the development of the V0 analysis workflow inside the new O2Physics framework, and the analysis detailed in the third chapter of this thesis. This analysis makes use of those workflows and of post-processing macros written by my hand to produce the histogram presented in the third chapter of this thesis and their uncertainties.

I also carried out tests of the new DCA propagation algorithm used in the new Run 3 framework, and made sure that the new analysis framework gave similar results when analysing the V0 decays of Run 2 data converted into the new Run 3 framework format. Those tests were done as a pre-requisite to the work presented in this thesis.

The first results obtained with the pilot beam data were approved as performance figures for the International Conference on High Energy Physics 2022, and I gave a talk during this conference to present those results along with other pilot beam results obtained by the collaboration.

This research was ethically approved. The request for ethical approval and its confirmation can be found at the end of this document.

Acknowledgments

Abstract

During the second long shutdown of the Large Hadron Collider (end of 2018 to middle of 2022), the ALICE detector was the subject of a complete reworking of its detector, reconstruction and analysis software, to prepare for the analysis of collisions happening at an increased interaction rate and recorded continuously, without trigger. The recording in October 2021 of the pilot beam proton-proton collisions at $\sqrt{s} = 900\,\text{GeV}$ and the production of Monte Carlo data simulating those beam conditions allowed an extensive test of this new detector as well as of the reconstruction and analysis tools. This work focuses in this context on the analysis of the V0 decays K^0_S and Λ in a Monte Carlo simulation of the pilot beam collisions. Those decays are building blocks for the analysis of strange decays in general, a valuable probe of the quark-gluon plasma. Their transverse momentum spectra are computed from the data reconstructed using the new analysis software, and compared to the initial spectra generated by the simulation. The analysis suite succeeds in reproducing the generated spectrum. The lower reconstruction efficiency compared to analyses done before the upgrade prompted a loosening of the reconstruction cuts despite leading to additional computing load. An imperfection in the calibration of the first preliminary results from real data is also observed.

Contents

Glossary:

- ALICE - A Large Ion Collider Experiment

- AO2D - Analysis Object Data file format in O2

- DCA - distance of closest approach

- FIT - Fast Interaction Trigger detector

- FT0 - plastic scintillator detector, FIT subdetector

- FV0 - Cherenkov detector, FIT subdetector

- ITS - Inner Tracking System detector

- LHC - Large Hadron Collider

- O2 - new Online-Offline reconstruction framework used by ALICE in Run 3

- Pb-Pb collision - lead-lead collision

- PCA - point of closest approach

- PID - particle identification

- pp collision - proton-proton collision

- p_T - transverse momentum, perpendicular to the beam direction

- QCD - quantum chromodynamics

- QED - quantum electrodynamics

- QGP - quark-gluon plasma

- ROOT - framework for data processing used by CERN and many (particle) physics experiments

- TPC - Time Projection Chamber detector

- V0 - decay topology of a neutral particle, with characteristic V shape

List of Figures

Introduction

Several signs of an unconventional state of matter have been spotted in multiple high-energy physics experiments at the end of last century, which led to the European Organization for Nuclear Research (known as CERN) announcing the discovery of the quark-gluon plasma in February 2000. The quark-gluon plasma, which is assumed to have existed in the very first instants of the universe, consists of unconfined quarks and gluons interacting with each other, as opposed to their bound states that is the norm in colder matter. This state can be reached in the first instants of a nuclei collision at ultrarelativistic energies.

The study of this quark-gluon plasma is one of the main missions of ALICE, which probes matter through high-energy lead-lead collisions as well as proton-proton collisions for comparison with the former.

The experiment exited this year a phase of shutdown that allowed for the upgrade of the detector. Run 3, the name of the period of activity ALICE entered this year after the restart of the Large Hadron Collider, will witness lead-lead collision events inside the detector at a rate a hundred time higher than in Run 2. The new physics objectives involve the detection of rare events. In this context, the processing of data significantly changed, with a switch to a continuous readout to record all collisions without dead time, and the development of a new reconstruction framework with a first online analysis step to compress the data from the detector before storage.

Proton-proton collisions were recorded in October 2021 as part of a pilot beam at a total collision energy of $\sqrt{s} = 900\,\mathrm{GeV}$. It was used by ALICE, along with Monte Carlo data simulating the same beam conditions, to do an extensive test of the new detector as well as of the reconstruction and analysis tools. This work focuses on the pilot beam Monte Carlo data and investigates the analysis of the V0 decays K_S^0 and Λ. Those decays are the building blocks for the analysis of strange decays in general, a valuable probe of the quark-gluon plasma. The transverse momentum spectra of K_S^0 and Λ are computed from the data reconstructed using the V0 analysis workflows developed for this thesis, and compared to the initial spectra generated by the simulation.

A theoretical overview of particle physics, of the quark-gluon plasma and of the strangeness probe will be first presented, followed by a short presentation of a few kinematic concepts necessary to the understanding of the study. Then the ALICE experiment will be presented and the reconstruction process given an overview. Finally, the analysis undertaken for this thesis will be detailed and the results discussed.

I – Theoretical overview

The following chapter will give a summary of theoretical physics concepts necessary to the understanding of the work undergone in this thesis.

1.1 Standard Model

Particle Physics saw the start of its modern formulation during the first half of the last century with the establishment of quantum physics and special relativity. Using this framework that was refined into the Quantum Field Theory, the Standard Model was developed throughout the second half of the 20th century. It unifies three of the four fundamental forces at play in our world: electromagnetism, weak and strong interactions.

These forces dictate all the possible processes involving the different particles described in the Standard Model. The fundamental particles (as opposed to composite) are divided in two families, the fermions and the bosons, distinguished by their quantum statistics: fermion distributions follow Fermi-Dirac statistics, as fermions obey the Pauli exclusion principle and thus are forbidden from occupying the same quantum states, while bosons follow Bose-Eistein statistics, because they are not limited by the same exclusion principle and thus are allowed to occupy the same states. Fermions have a half integer spin quantum number, while bosons have an integer spin. This quantum number is an intrinsic property of particles that gives rise among other things to magnetic moments for charged particles.

The fundamental bosons encompass the scalar (spin-0) Higgs boson, which is behind the mass of the fundamental particles, and the vector bosons (spin-1), or gauge bosons, carriers of the three fundamental forces. The photon for the electromagnetic force which acts on the quantum number electric charge of involved particles and is described by quantum electrodynamics (QED). Eight gluons for the strong interaction, which acts on the quantum number colour charge. The strong interaction is responsible for the binding of quarks into hadrons like protons and neutrons and for the binding of those into atomic nuclei, and is described by quantum chromodynamics (QCD). And the Z^0 and W^+ and W^- bosons for the weak force responsible for the radioactive beta decay, where a neutron decays into a proton, an electron and a neutrino. The weak interaction is also the force that creates bridges between the fundamental fermion generations by breaking the conservation of those generations.

The fundamental fermions are divided in two families. The quarks (with the six flavour states up, down, charm, strange, top, bottom, and the three colour charge states green, red and

blue), which together build the composite hadrons bound by the strong interaction (proton, neutron, pions, etc). And the leptons, particles blind to the strong interactions, that can be further divided in two classes, charged leptons (electron, muon and tau) and neutral leptons (electron neutrino, muon neutrino, tau neutrino). All those fermions are ordered in three generations, characteristic of the flavour quantum numbers the weak interaction acts upon and of the energy scales they appear in: electron, electron neutrino, quark up and quark down form the first generation; muon, muon neutrino, quark charm and quark strange form the second generation; tau, tau neutrino, quark top and quark bottom form the third generation. Those generations and families are conserved in strong interactions, who are notably blind to leptons, or electromagnetic interactions: if a system does not have strange quarks for example, the only way strange quarks are going to be created through the strong or electromagnetic interaction is with the creation of strange quark-antiquark pairs. The weak interaction is the force that allows mixing of those fermions from the same family and generation. In addition to that, the weak interaction sees the quarks transition between different generations due to the fact that the eigenstates for the weak interaction are not the free quarks (the mass eigenstates) but a superposition of them, described by the CKM (Cabibbo-Kobayashi-Maskawa) matrix. [Griffiths (2008)] gives a good introduction to particle physics for more details.

Quarks have yet to be observed in isolation experimentally. This phenomenon, named colour confinement, means that the study of quarks can only be carried indirectly, by looking at composite particles, hadrons. The Quark Model describes the way quarks combine to form those hadrons, divided in two families: the mesons, bound states of a quark and an antiquark, and the baryons, bound states of three quarks (plus any number of quark-antiquark pairs). The proton p, superposition of two up quarks and one down quark (written uud) is an example of a baryon. The pion π^-, superposition of an up antiquark and a down quark ($d\bar{u}$) is an example of a meson.

1.2 Colour confinement

In contrast to photons for the electromagnetic force, the gluons interact with each other via the strong interaction that they mediate. They carry a colour charge. This has very strong implications in that gluons interact with themselves as they propagate. Phenomenologically, the description is that they form flux tubes between two coloured objects, of nearly constant cross-sectional area into which all the colour electric field is squeezed [Greensite (2011)]. This translates into a potential energy between two coloured objects that increases as the distance between them grows. The effective colour charge potential V_{QCD} is usually taken to be of the form shown in Eq. 1.1 [Perkins (2000)]:

$$V_{QCD}(r) = -\frac{4}{3}\frac{\alpha_S}{r} + k \cdot r \qquad (1.1)$$

where r is the distance between two coloured objects, k is an effective flux tube constant for the long distance interaction, and α_S is the strong coupling constant that dictates the strength of the interactions between coloured particles.

While at small distances the behaviour is identical to that in a Coulombian field like in electromagnetism, at higher distances the linear term $k \cdot r$ becomes dominant and the potential energy never stops growing. As two coloured objects q_a and q_b keep moving apart, it eventually reaches a point where it is more energetically favourable to create a new quark-antiquark pair q_c-$\overline{q_c}$. One of the newly created quarks will bind itself with q_a, the other one with q_b, such that the total colour charge of each bound state is zero. Hence the observed colour confinement. This is illustrated in Fig. 1.1.

1.3 Deconfinement and quark-gluon plasma

In the 1980s a hypothetical new state of matter was postulated, in which the deconfinement of quarks and gluons could be observed: the quark-gluon plasma, or QGP for short [Rafelski (2020)].

When gluons and new quarks are added to the system of the two quarks q_a and q_b that are being studied, and when the density of those colour charges gets higher and higher, a new effect begins to show. A screening of the colour charges of q_a and q_b by the surrounding ones, similar to the Debye screening described in QED [Shuryak (2004)]. The modified potential energy V_S between q_a and q_b can be described by Eq. 1.2:

$$V_S(r) = -\frac{\alpha_S}{r} \cdot e^{-\frac{r}{r_D}} \tag{1.2}$$

where r is the separation between two quarks and r_D the Debye screening length of the system.

As the density of charges in the system increases (through compression or creation of new colour charged particles by an increase of temperature), the Debye screening length goes down. Once it decreases below the size of hadrons, the latter lose their integrity. This is the QGP,
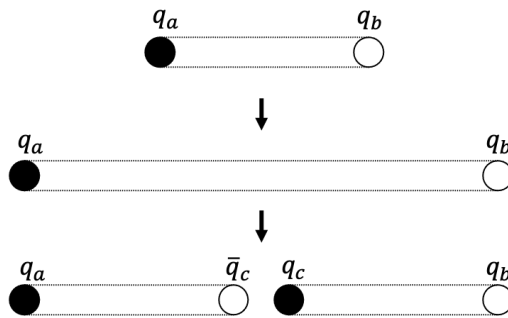
Figure 1.1: Colour flux tube breaking by quark-antiquark pair production as two quarks are pulled apart from each other.

in which quarks and gluons still interact with other nearby colour charges but are not bound inside hadrons anymore.

This state of matter presents multiple points of interest that motivate an in-depth study of its properties. It is first a new frame for the study of the strong interaction of the Standard Model, that of a medium of free quarks and gluons, where hadrons and nuclei are deconstructed. It brings the possibility to study the collective behaviour of quarks, or the hadronisation of quarks as the medium cools down out of the QGP state. In addition, this state of matter is of great interest in cosmology. Indeed, studying the QGP phase should help understand the early universe as it is believed to have gone through a similar phase during its early life [Lange (2004)]. Likewise, the density of the core of neutron stars can reach values two to three orders of magnitude higher than that of a neutron: it is expected those hadrons overlap, and thus the QGP could be a natural phase of a neutron star's core [J. C. Collins and Perry (1975)].

Reaching the high density and temperature conditions necessary to enable the formation of a plasma of quark and gluons is no trivial task. The heavier atoms have several nuclei with many hadrons, and colliding such nuclei together at very high energies constitutes the best way that has been found to reach the high quark densities necessary to this task.

1.4 Creating a QGP with heavy-ion collisions

What happens when two heavy ion nuclei collide after they each have been accelerated to energies high enough for the formation of plasma of quarks and gluons?

Moments before the collision, the two incident large nuclei, spherical in their rest frame, take for an observer in the lab frame the shape of two discs. Their velocity is very high and thus their dimension is greatly Lorentz contracted in the direction they travel, the relativistic factor gets as high as ~2900 in a lead-lead collision at the Large Hadron Collider experiment [Brüning et al. (2004)], for an apparent longitudinal to transverse diameter ratio of 1/2900. Each of the disks is made of a great number of nucleons, each made of quarks and antiquarks. As they collide, a few of the quarks and gluons in the nuclei will interact in hard processes with high transverse momentum transfer. Those interactions are not of interest for this introduction to the QGP formation in a heavy ion collision. Most of the interactions will only involve small momentum transfer and the nuclei will for the most part continue their course along the initial trajectory. In their wake, between the two propagating discs, colour fields are produced from the colour interaction of the disks. Those fields have very high energy densities and decay into many quark-antiquark pairs and gluons that will begin to interact with each other. If the initial collision energy was high enough to allow the energy density of the system between the two discs to reach the critical value necessary for the QGP formation, $\sim 1\,\mathrm{GeV/fm^3}$ according to [Andronic et al. (2018a))], a QGP should form. The quarks and gluons inside it are strongly coupled to each other, so much so that they form a medium that expands and flows like a

relativistic hydrodynamical fluid with very low viscosity [Busza, Rajagopal, and Schee (2018)]. As the discs keep moving apart, the QGP in expansion cools down, but new QGP keeps being produced in the wake of the discs. Each element of volume in which the QGP cools down soon reaches a phase transition, a chemical freeze-out around a temperature of ~155 MeV[1] [Bazavov et al. (2019), Andronic et al. (2018b)], that sees the deconfined quarks and gluons hadronise back into hadrons. The gas of elastically interacting hadrons keeps expanding and cooling until the thermal freeze-out temperature of ~95 MeV, after which the hadrons cannot interact anymore and propagate freely outwards, into the detector [Busza, Rajagopal, and Schee (2018)]. Those steps are pictured in Fig. 1.2, with a space-time graph of the heavy-ion collision in the (z, t) plane (the z-axis following the direction of the incident particles, and the t-axis being the axis of time in the lab frame) and snapshots of a simulation of the same collision.

While the distribution of the transverse velocities are low initially due to the collision being frontal, the expansion of the fluid medium that is the QGP builds up, due to pressure, large transverse velocities, up to the order of half the speed of light. And it is those transverse velocities created by this hydrodynamical expansion that will be detected in the detectors through the particles that are driven by them.

The scenario presented was that of a completely frontal collision. In practice, the two discs are not perfectly aligned as they collide. This nonalignment is described by an impact parameter, often called b, the distance between the centres of the two discs. Because b cannot be directly measured, another quantity is used to describe this nonalignment: the centrality of the collision, expressed as a percentile range and obtained by fitting the distribution of a collision observable indicative of the alignment (for example the collision particle multiplicity distribution) to a model [Acharya et al. (2018)]. The centrality of a collision is correlated to the number of nucleons from the two ions that actually participate in the collision and the transfer of energy to the potential QGP system.

In February 2000, the European Organization for Nuclear Research (known as CERN) announced that *"The data provide evidence for colour deconfinement in the early collision stage and for a collective explosion of the collision fireball in its late stages. The new state of matter exhibits many of the characteristic features of the theoretically predicted quark-gluon plasma."* [U. Heinz and Jacob (2000)]. Those evidence are the suppression of the abundance of J/ψ in heavy-ion collisions [Matsui and Satz (1986), Abreu et al. (2000)] and the enhancement of that of strange hadrons [Fini et al. (2001)]. Since then, other observables have further solidified the evidence. The observation of the low viscosity hydrodynamical behaviour of the QGP [U. W. Heinz (2005)]. The observation of the quenching of jets, the manifestation in the detector of the hard processes briefly mentioned at the beginning of this subsection: those same process happen in the simpler proton-proton collisions that QCD describes really well at high energy,

---

[1]the temperatures in this thesis are multiplied by the Boltzmann constant $k_B =8.617 \times 10^{-5}$ eV/K to allow a more convenient comparison to the energy units encountered in it
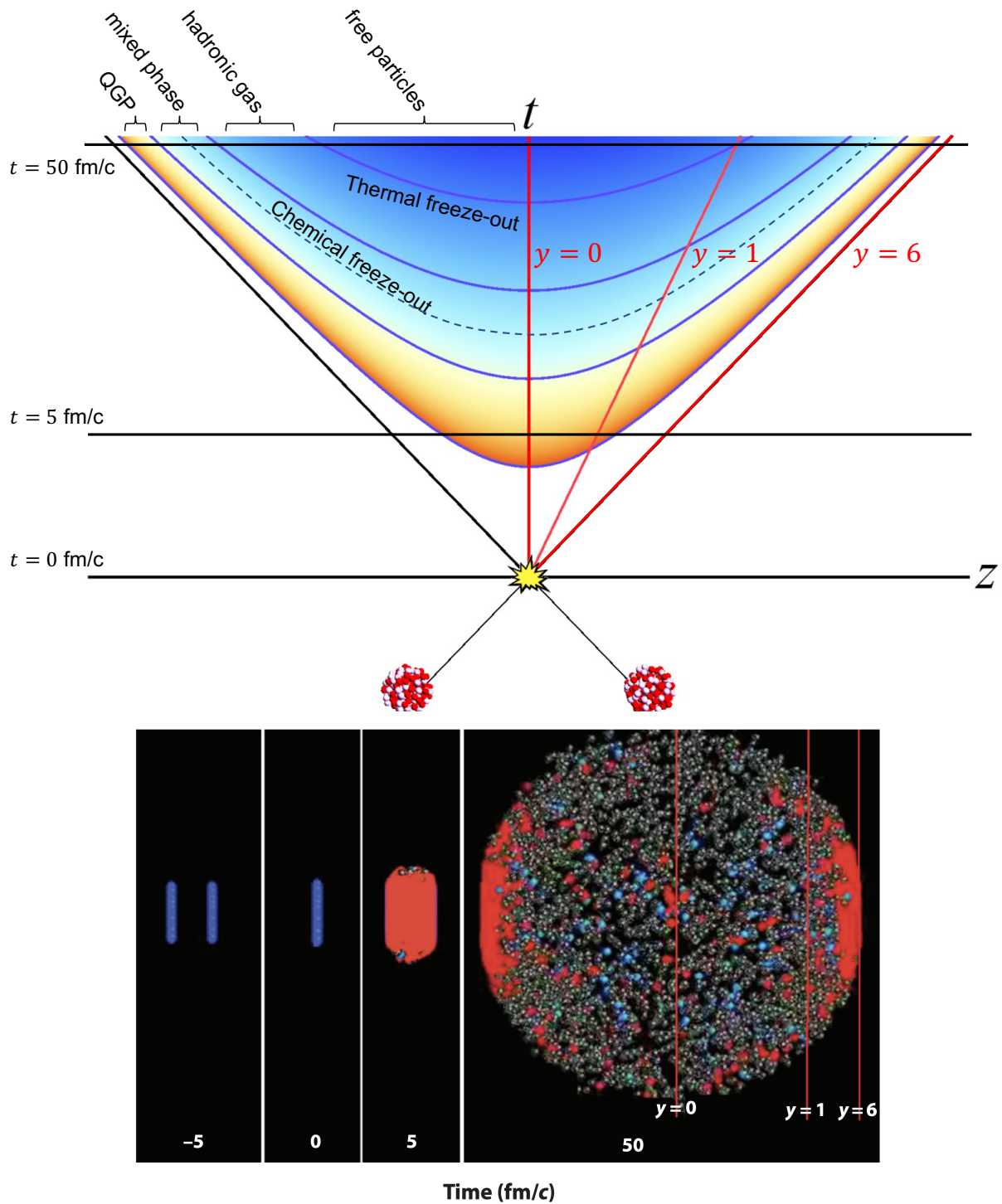
Figure 1.2: Space-time graph of the evolution of a heavy-ion collision in the (z, t) plane (top) and snapshots of a simulation of the same collision with regions of QGP represented in red and hadrons represented in blue and grey (bottom) — the blue curves in the space-time plot are isolines of proper time $\tau = \sqrt{t^2 - z^2}$ of the system whose evolution is a function of, the three frames at $t = 0$, 5 and 50 fm/c in the bottom figure are represented in the space-time graph by the three horizontal black lines, and the red lines in the last snapshot represent the rough position of particles with rapidities $y = 0$, 1 and 6 — adapted from [Busza, Rajagopal, and Schee (2018)].

and the presence of a QGP medium has them lose energy differently as they propagate through it than in a vacuum [Adcox et al. (2001))].

1.5   Strangeness

Strangeness is the third lightest flavour of quarks, after the quarks up and down that made up the world we see and touch, and yet they are absent from most of the matter around us, the strange hadrons they inhabit being too unstable in non-exotic conditions. The single strange hadrons K^+ ($u\overline{s}$), K_S^0 (a superposition of $d\overline{s}$ and $s\overline{d}$), Λ (uds), and the multi strange hadrons ϕ ($s\overline{s}$), Ξ^- (dss) and Ω (sss), and their antiparticles, are the most common strange hadrons detected in the largest heavy ion colliders, the LHC.

1.5.1   Strangeness enhancement: a probe of QGP

The enhanced abundance of observed strange hadrons is one of the initial pieces of evidence that has brought CERN to announce the discovery of the QGP. The theoretical basis of this evidence relied on the difference in expected strangeness abundance between a gas of hadrons at high temperature and a QGP [Rafelski (2020)].

The first argument is that the temperature necessary for QGP formation is indeed close to the energy required for the thermal production of $s\overline{s}$ pairs: close to ~200 MeV, twice the bare mass of a strange quark [Tanabashi et al. (2018)]. Thus, the processes of quark-antiquark annihilation and gluon fusion to $s\overline{s}$ pair production ($q\overline{q} \rightarrow s\overline{s}$ and $gg \rightarrow s\overline{s}$) are remarkably favoured, as the gluons and quarks in the medium are excited to the QGP temperatures. Though new strange quarks are created, the strangeness quantum number is conserved in the system, as required by conservation laws for strong interactions, as it is defined as proportional to the difference between the number of strange quarks and antiquarks. [Rafelski and Muller (1982)] showed that the gluon fusion process is the main contributor to this enhancement thanks to its quicker $s\overline{s}$ production rate, but also thanks to its quicker characteristic time to reach equilibrium as the $s\overline{s}$ annihilation process competes with the production. This time constant is such that an equilibrium could indeed be reached within the QGP lifetime above energy densities of $1\,\text{GeV/fm}^3$ (the critical value mentioned in section 1.4). The second idea is that while a medium of hot hadrons would technically see some strangeness enhancement, compared to the yields from a single nucleon-nucleon collision, from subsequent hadron inelastic scattering through internal $q\overline{q} \rightarrow s\overline{s}$ processes where the other quarks in the hadrons are spectators, it has been shown by [Koch and Rafelski (1985)] that said enhancement was expected to be much lower than the one from the quark-antiquark annihilation process alone in a QGP, up to several orders of magnitude for multi-strange hadrons, without even considering the much increased enhancement due to gluon fusion. Thus, the potential background of strangeness enhancement

from hadron gas is expected to be low, and especially more distinguishable for multi-strange hadrons.

A more qualitative way to look at this can be to consider the difference in energy cost required to create strange quarks for hadron interactions to that for a QGP. Typical strangeness production processes that can occur in a hadron gas are $\pi + N \to K + \Lambda$, with N a nucleon and K either $K^{\pm}$ or K^0_S, or $\pi + \overline{\pi} \to K + \overline{K}$ [Koch and Rafelski (1985)] and the energy cost of such processes are $\Delta E = m_K + m_{\Lambda} - (m_{\pi} + m_N) = {\sim}540\,\text{MeV}$ and $\Delta E = 2 \cdot m_K - 2 \cdot m_{\pi} = {\sim}720\,\text{MeV}$. In a QGP, there is no longer any quark confinement requirement, and thus $s\overline{s}$ pairs can be created as is, and the energy threshold involved is quite lower at ${\sim}200\,\text{MeV}$.

The investigation of QGP creation with high quark density heavy-ion collisions require comparing the results obtained with collisions in which a QGP is not created. To compare strangeness enhancement in a QGP and in a hadron gas, collisions of a proton with a heavy ion can be studied, while proton-proton collisions will allow for a calibration of the probe used without any surrounding nuclear matter.

1.5.2 Experimental evidence for strangeness enhancement in heavy-ion collisions

The Super Proton Synchrotron (SPS) at CERN was host to many experiments dedicated to the investigation of the QGP. Strangeness enhancement was indeed observed, as shows for example Fig. 1.3, in which the experiment WA97 [Fini et al. (2001)] at the SPS compared the strangeness yields between Pb-Pb and p-Be collisions at the same beam momentum per nucleon of $158\,\text{GeV/c}$ with a fixed lead target, for a total collision energy in the centre of mass of about $\sqrt{s_{NN}} \approx 17\,\text{GeV}$. The enhancement is calculated as the ratio between the strange particle yield per nucleon participants $< N_{wound} >$ in the collision for Pb-Pb, where a QGP is expected, and that for p-Be, where the gas of hadron is expected to not form a QGP. This is translated in Eq. 1.3. In particular, it can be seen that, as expected if Pb-Pb reaches a QGP, the enhancement increases with the number of strange quarks in the hadron, with the triple strange Ω showing an enhancement of an order of magnitude. The same enhancement observable would be measured in the STAR experiment at RHIC and in ALICE in the following years, the result of these measurements are shown in Fig. 1.4 as a function of $< N_{wound} >$ (renamed $< N_{part} >$ in the figure). The trends observed above are still valid. One can notice that the enhancement decreases as the energy of the collision increases: this is according to [Abelev (2012)] due to the fact that the baseline yields increase following a power-law as the collision energy increases.

$$E = \left(\frac{< yields >}{< N_{wound} >} \right)_{Pb-Pb} \Bigg/ \left(\frac{< yields >}{< N_{wound} >} \right)_{p-Be} \tag{1.3}$$

From the same experiment, came Fig. 1.5 that was acknowledged as a definite proof that
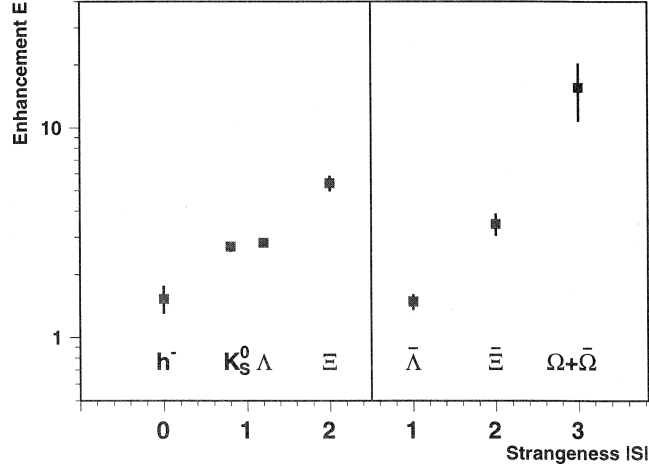
Figure 1.3: Strangeness yield enhancement as a function of the number of strange quarks per hadron — h^- all non strange negative hadrons — taken from [Fini et al. (2001)].
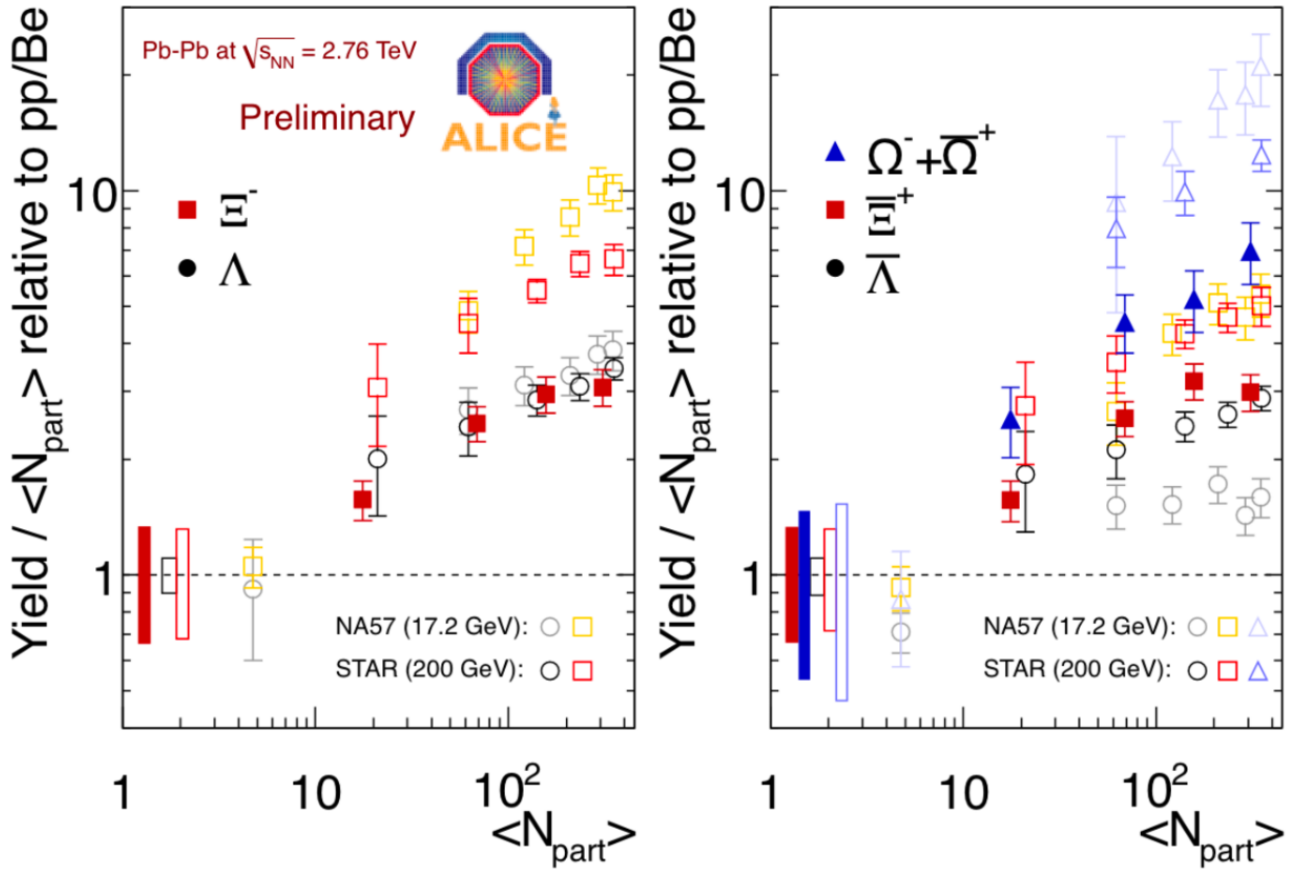
Figure 1.4: Strange particle production as a function of the number of participant nucleons $< N_{part} >$ for $\sqrt{s_{NN}} = 0.017$, 0.2, and 2.76 TeV collisions relative to p-Be (NA57) and pp (STAR, ALICE) — taken from [Abelev (2012)].

a QGP phase had been observed [Rafelski (2020)]. In it, is plotted for Pb-Pb collisions at a beam momentum per nucleon of 158 GeV/c (centre of mass total collision energy $\sqrt{s_{NN}} \approx$ 17 GeV) the transverse mass distribution of the hadrons Λ, Ξ^- and Ω^- (and their antiparticles), with the transverse mass defined as $m_T^2 = \sqrt{m^2 + p_T^2}$ where p_T is the momentum component transverse to the beam direction at the collision point. The identical slopes (corresponding to identical exponential coefficient as the y-axis is plotted in a logarithmic scale) are indicators of an identical production mechanism, and of the free-moving. They are visibly independent of the quark content, and of the matter-antimatter nature of the particles (within small errors). Those two points are not explainable with a gas of hadron production source [Torrieri (2004)] in which, for example, antiparticles should show a very different slope than their counterparts, as they annihilate at a rate that varies strongly with p_T, and the apparent temperatures (the slopes) should be quite dependent on mass as equilibrium is reached a lot slower than in a QGP system.

In the continuity of this, those transverse mass measurement have been used to fit the thermal freeze-out temperature. [Torrieri and Rafelski (2001)] use the following formula (Eq. 1.4) to model the transverse mass distributions of strange particles, under the assumption of a QGP with a sudden freeze-out, after which the hadrons will not interact anymore:

$$\frac{\mathrm{d}^2 N}{\mathrm{d}m_T \mathrm{d}y} \propto \left(1 - \frac{\mathbf{v_f^{-1}} \cdot \mathbf{p}}{E}\right) \cdot \gamma \cdot m_T \cdot \cosh y \cdot \exp\left\{-\gamma \frac{E}{T}(1 - \frac{\mathbf{v} \cdot \mathbf{p}}{E})\right\} \tag{1.4}$$

with $\mathbf{v}$ the local flow velocity of the fireball matter where particles emerge, $\gamma = 1/\sqrt{1 - \mathbf{v}^2}$, $\mathbf{p}$ the momentum of the particle and $\mathbf{v_f^{-1}}$ being the hadronisation surface velocity.

The fit of this model they produced can be seen in Fig. 1.6 for the 4 centrality bins analysed by the WA97 experiment, for Λ, Ξ^-, Ω^- and their respective antiparticles, and for K_S^0. The distributions are remarkably well reproduced by the fit. The thermal freeze-out temperature of the fireball that they obtained was of ~145 MeV, not far from the ~156 MeV value calculated with more recent results [Bazavov et al. (2019), Andronic et al. (2018b)].

1.5.3 Recent observations on strangeness production in hadron collisions in ALICE

QGP studies at the LHC have been able to explore hadron collisions at much higher energies. The ALICE experiment, designed primarily for the study of the QGP, saw proton-proton, lead-lead and other ion-ion collisions at total collision energies per nuclei ranging from $\sqrt{s_{NN}} =$5.02 TeV to 13 TeV. Figure 1.7 shows one preliminary result from ALICE that looks at the ratios of strange particle yields to charged pion particle yields as a function of the charged particle multiplicity of the collision, i.e. the number of charged particles generated in the collision. At those energies, this plot shows that pp, p-Pb and ion-ion collisions do not
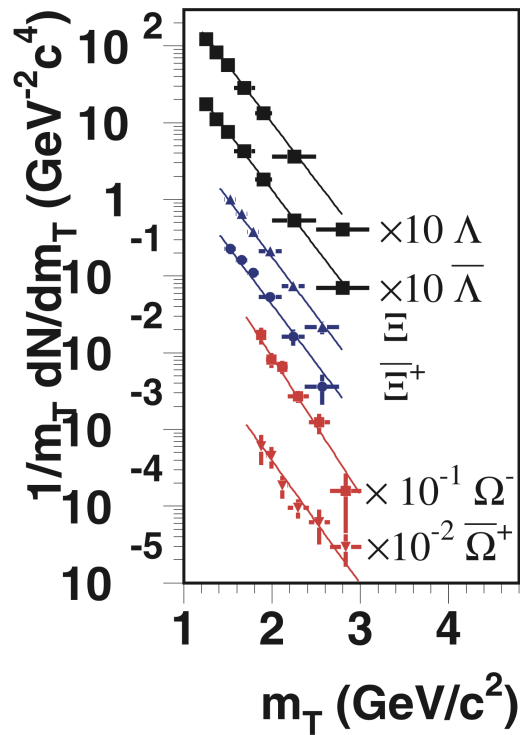
Figure 1.5: Transverse mass distributions for Λ, Ξ^-, Ω^- and their antiparticles — taken from [Fini et al. (2001)].

show differences in behaviour: all collision types superpose very well on a smooth line for each particle type. Likewise, the ratio of strange yields to pion yields does not seem to show a change with the total energy of the collision. Instead the ratio seems to depend on the final charged particle multiplicity. ALICE understands the striking similarities between pp and p-Pb systems and Pb-Pb systems *"to be connected to the formation of a deconfined QCD phase at high temperature and energy density"* in the former [Adam et al. (2017)]. The formation of a QGP phase might thus not be limited to central heavy-ion collisions, with proton-proton collisions showing QGP-like signatures at high multiplicities.

Another observable tied to strangeness and to the presence of QGP is the Λ/K_S^0 ratio, measured in Fig. 1.9 as a function of p_T for central and more peripheral Pb-Pb collisions at $\sqrt{s_{NN}} = 2.76\,\text{GeV}$ in ALICE. The measurement of this ratio historically reinforced the hydrodynamical models used to describe the QGP [Hanratty (2014)], with the hydrodynamical description fitting the low-p_T part of the Λ/K_S^0 ratio quite well in the figure. It also contributed to highlighting a new mechanism for hadronisation in the QGP to explain the behaviour of this ratio at intermediate p_T: the recombination process, where two or three quarks combine to form a hadron. This recombination model, along with one called EPOS combining the hydrodynamical description and the recombination are also shown in the same figure. EPOS fits the data very nicely. This ratio was also measured in pp collisions and in more centrality classes of Pb-Pb collisions in ALICE as seen in Fig. 1.8. While central Pb-Pb collisions show indeed a significant enhancement of this ratio at low and intermediate p_T, the most peripheral
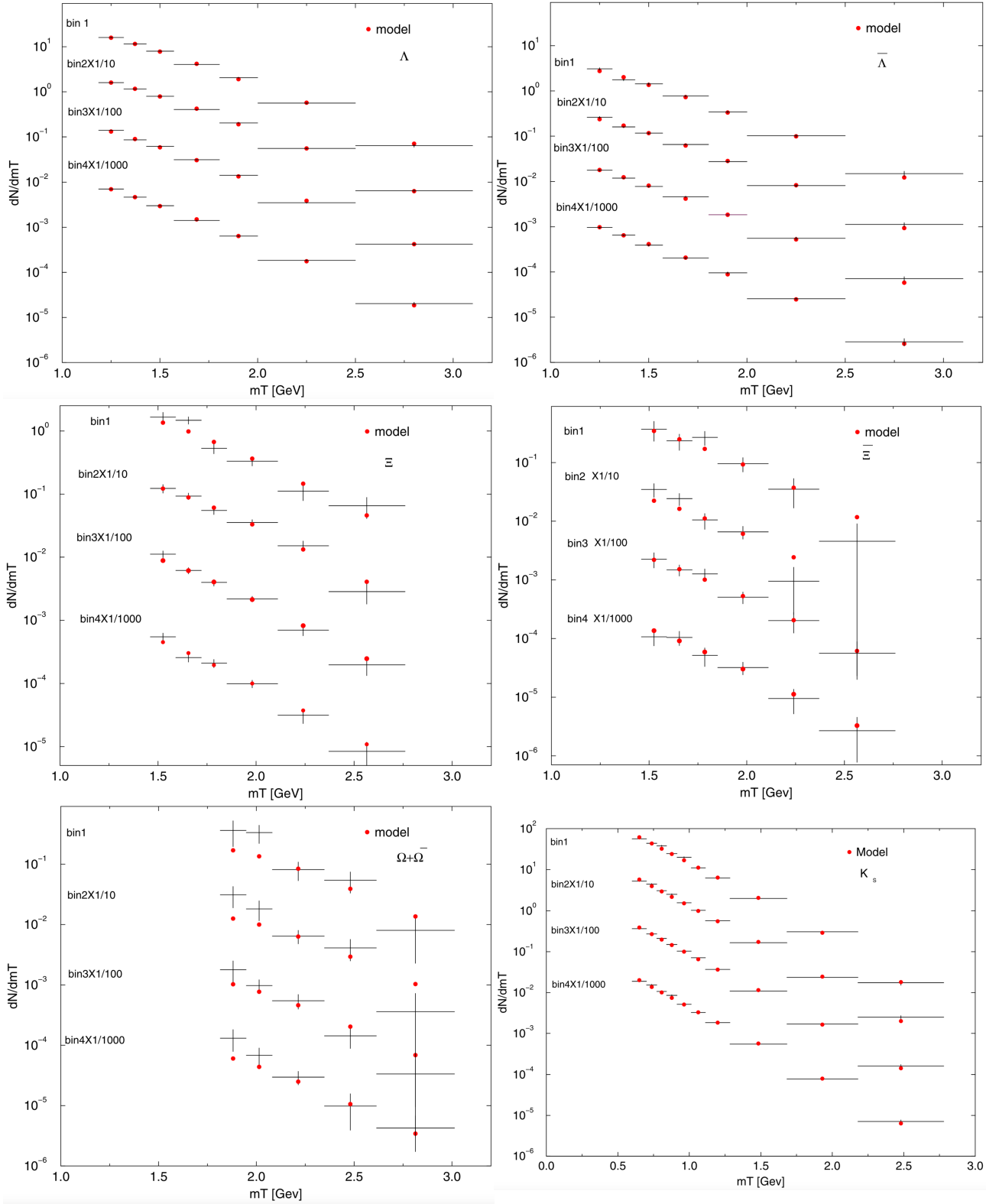
Figure 1.6: Fit of the transverse mass spectra measured by the WA97 experiment over 4 centrality bins, for Λ, $\overline{\Lambda}$, Ξ^-, $\overline{\Xi}^+$, $\Omega^- + \overline{\Omega}^+$, and K_S^0 — taken from [Torrieri and Rafelski (2001)]

13
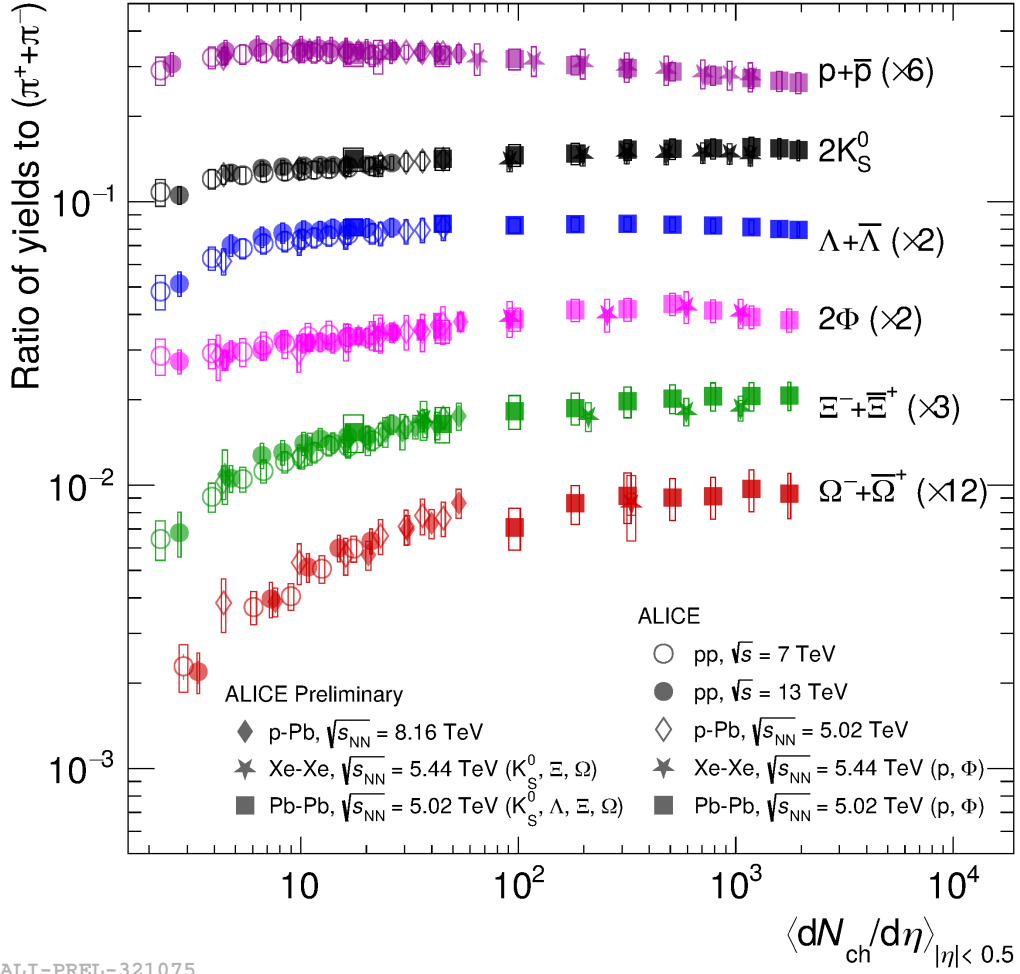
Figure 1.7: Particle yield ratios to pions as a function of charged multiplicity for different collision systems and energies.

class of Pb-Pb collisions seldom show any difference compared to the pp results within the uncertainties: the evolution of the ratio distribution with centrality is very smooth, and a peak is still present in pp collisions, if smaller. This is studied in further detail in [Acharya et al. (2019)] in Fig. 1.10, where the Λ/K_S^0 ratio is measured in pp, p-Pb and Pb-Pb collisions for two classes of particle multiplicity: one where the average is high and one where it is low. The ratio increases at high multiplicity regardless of the collision system. Here as well, one feature that was explained before as characteristic of the formation of the QGP is also observed in a small collision systems like pp at the LHC energies [Bhasin and Sharma (2022)] when looking at high multiplicity final states. Further studies are needed to explain the mechanisms responsible for those effects in small collision systems.

A very recent analysis done by ALICE was the measurement of the production of strange hadrons inside jets and the comparison of this production to that outside of jets [Cui (2022)]. The reconstructed strange decays where tagged as belonging to a jet if the reconstructed strange particle direction fell within the jet cone (defined with a radius fixed as a parameter of the jet reconstruction algorithm). This measurement was carried out in order to study those QGP-like behaviours seen in pp collision systems at the LHC energies. The Λ/K_S^0 ratio was plotted for the strange production inside the jet cone, outside the jet cone (the underlying event) and on average in the whole collision (the inclusive result) in Fig. 1.11. The peak observed in inclusive measurements is not seen inside jets, while the distribution from the underlying event matches that from the inclusive measurement very well. This indicates that the processes behind the Λ/K_S^0 ratio peak (hydrodynamical effects interacting with the recombination process) are limited to the soft particle production processes, as opposed to the hard processes at play in jets.

1.6 Particle kinematics - Short overview

This section will give a short presentation of a few kinematic concepts necessary to the understanding of particle detection techniques presented later in the next chapter and to the analysis.

1.6.1 Invariant Mass

The invariant mass is, in the case of a single object, what is referred to as the mass in the everyday life. It is, more precisely, the mass of a particle in a frame where this particle is at rest (for particles of non-zero mass). The invariant mass M_0 of a particle or system can be defined using the energy E_0 and momentum $\mathbf{p_0}$ of this particle or system in a chosen, as written in Eq. 1.5 [Tanabashi et al. (2018)].
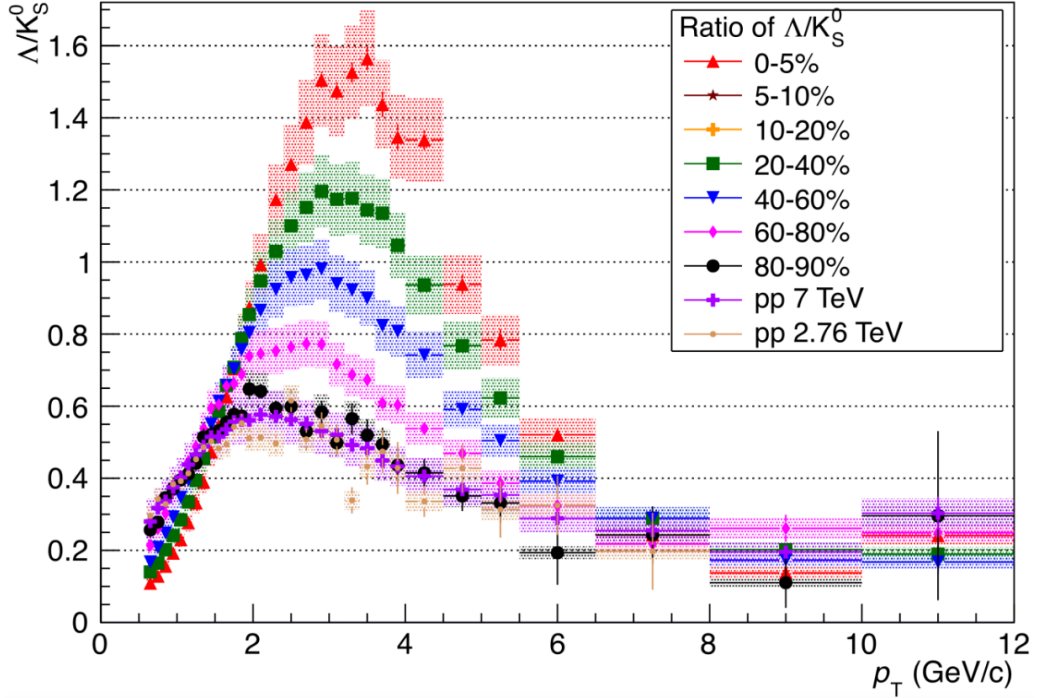
Figure 1.8: The Λ/K_S^0 ratio for Pb–Pb at $\sqrt{s} = 2.76\,\mathrm{TeV}$ for various centralities and for pp collisions — taken from [Hanratty (2014)]
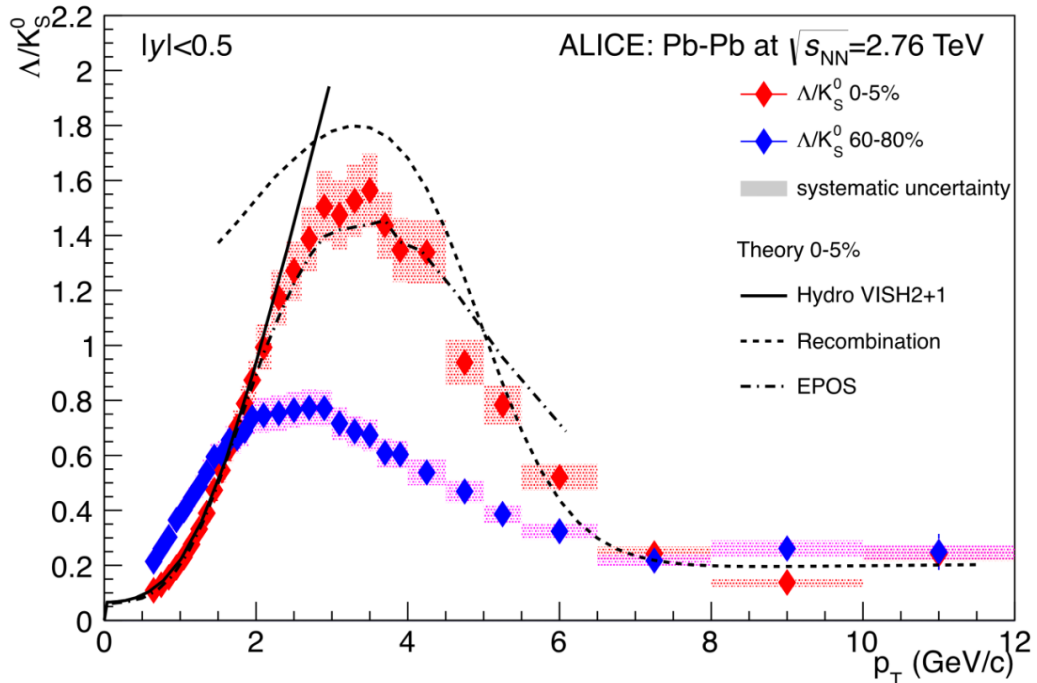
Figure 1.9: The Λ/K_S^0 ratio, as measured in Pb-Pb collisions at $\sqrt{s} = 2.76\,\mathrm{TeV}$ in 0-5% (most central) and 60-80% (more peripheral) centrality bins, as compared to theoretical predictions for the 0-5% centrality — taken from [Hanratty (2014)]

16
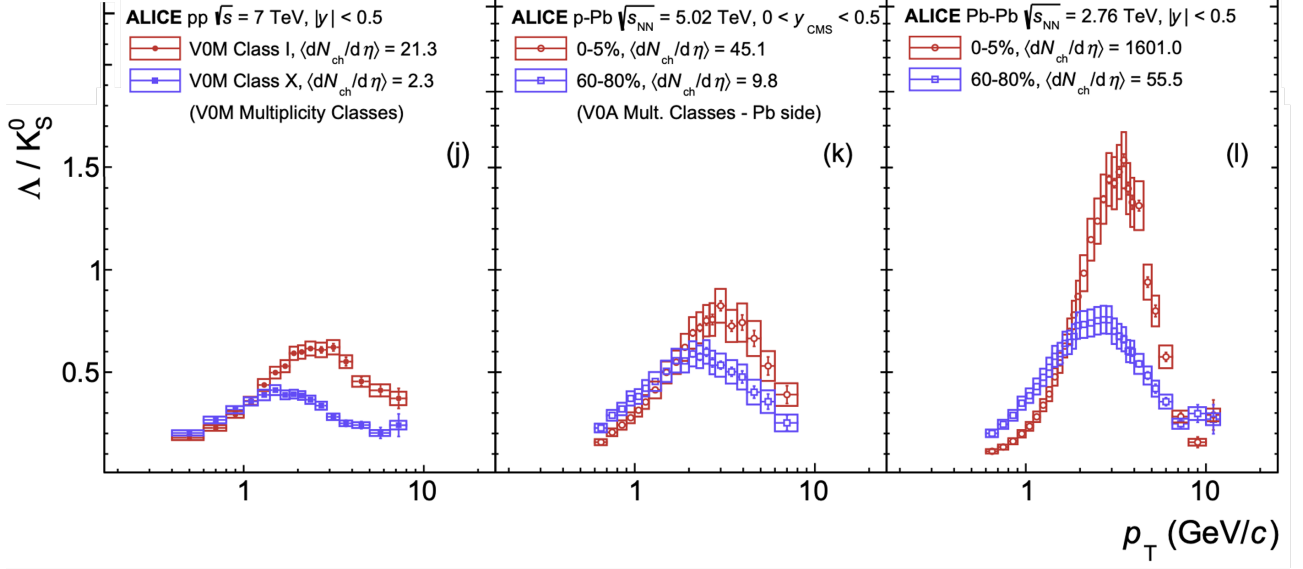
Figure 1.10: Transverse momentum dependence of the Λ/K_S^0 ratio, as measured in a high-multiplicity class in red and in a low-multiplicity class in blue for pp (j), p-Pb (k), Pb-Pb (l) collisions at $\sqrt{s} = 7\,\text{TeV}$, $\sqrt{s} = 5.02\,\text{TeV}$ and $\sqrt{s} = 2.76\,\text{TeV}$ respectively — taken from [Acharya et al. (2019)]
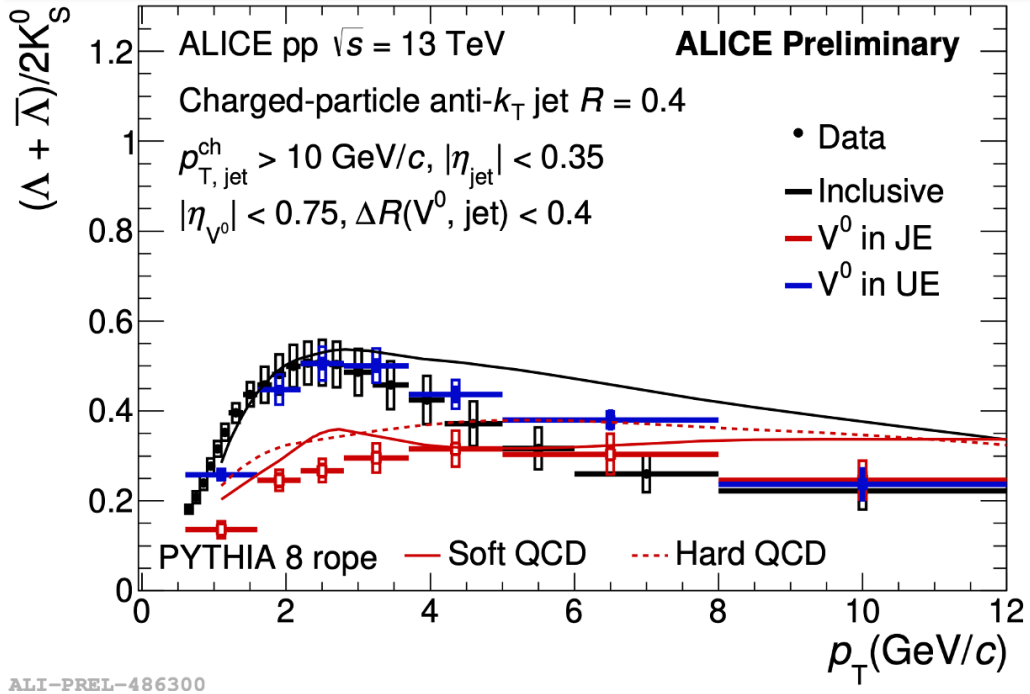
Figure 1.11: Transverse momentum dependence of the Λ/K_S^0 ratio, measured inside jets (red), in the underlying event (blue) and without distinction (black), for pp collisions at $\sqrt{s} = 13\,\text{TeV}$ — taken from [Cui (2022)]

$$M_0^2 c^2 = \left(\frac{E_0}{c}\right)^2 - ||\mathbf{p_0}||^2 \tag{1.5}$$

where c is the speed of light.

The invariant mass is an important property of particles, that does not change with a change of frame, and which measurement helps greatly with their identification in an experiment.

1.6.2 Particle Decay

Most particles are not eternal, be they elementary or not, and in fact the stability of particles like the electron and photon (which are described as completely stable) or the proton (which at a minimum has a supposed lifetime longer than the life of the universe) are more of an exception. Most of them decay in a matter of a small fraction of a second. To give some examples, a free neutron n has a mean lifetime τ of about 15 minutes, a pion π^+ a mean lifetime of the order of ~10^{-8} s, and a xi baryon Ξ^- a mean lifetime of the order of ~10^{-10} s.

The mean lifetime of a particle at rest corresponds to the length of time after which the probability that the particle has survived is $1/e \approx 0.37$. The probability $P(t)$ that a particle at rest with a mean lifetime τ has not yet decayed after a time t is given by Eq. 1.6 [Tanabashi et al. (2018)].

$$P(t) = \exp\left\{\frac{-t}{\tau}\right\} \tag{1.6}$$

Those decays appear to have rules, and most of them are so far well described by the Standard Model. Among them: a particle decays into particles of smaller invariant mass (called daughters as opposed to the mother particle that decayed into them); the invariant mass is conserved throughout a decay, that is the invariant mass of the system made out of all the daughter particles is equal to the one of the mother particle. The latter is a consequence of the conservation of energy and momentum.

A decay of one mother particle A into n daughter particles $B_1, B_2, ..., B_n$ is noted as in Eq. 1.7.

$$A \rightarrow B_1 + B_2 + ... + B_n \tag{1.7}$$

In the case of a two-body decay like the V0 decays studied here, the invariant mass M_0 of the mother particle, also invariant mass of the system made out of the two daughter particles, and the invariant masses m_1 and m_2 of the individual daughters are linked by Eq. 1.8.

$$M_0^2 c^2 = m_1^2 c^2 + m_2^2 c^2 + 2\left(\frac{E_1}{c}\frac{E_2}{c} + \mathbf{p_1} \cdot \mathbf{p_2}\right) \tag{1.8}$$

where E_1, E_2, $\mathbf{p_1}$ and $\mathbf{p_2}$ are the energies and the momenta of the daughters.

While the invariant mass of a particle has a unique value, the measurement of the invariant mass m_0 of a particular decay will give values m randomly distributed around m_0. Without experimental errors (which add to the spread of the distribution), the width of the distribution of this variable m is dictated by that of the energy E at which it has been produced, itself described by a Breit-Wigner distribution with a non-zero half-width at half-maximum equals to the decay width of the decaying particle [Tanabashi et al. (2018)]. This intrinsic decay width Γ is linked to the lifetime τ by the relation 1.9:

$$\Gamma\tau = \hbar \tag{1.9}$$

where $\hbar$ is the reduced Planck constant.

This non-zero width can be related to Heisenberg's uncertainty principle, stating that the product of the uncertainties in position and in momentum (that can be translated into an uncertainty in time and in energy) of a measurement cannot be smaller than $\hbar/2$ [Cohen-Tannoudji, Diu, and Laloë (1977)].

1.6.3   Rapidity and transverse momentum

The rapidity y is a common variable in particle collider physics that is usually defined as per Eq. 1.10. It is a measure of the boost of a system (usually in the lab frame) from its rest frame along the z-axis defined as the beam axis.

$$y = \frac{1}{2}\ln\frac{E + p_z c}{E - p_z c} \tag{1.10}$$

where p_z is the component of the momentum of the system parallel to the beam axis and E its energy.

The difference in rapidity between two frames is Lorentz invariant under boosts along the beam axis. As particles are produced at high velocities, they are boosted along the beam direction, and thus particle production will not be uniform in polar angle but will be in rapidity [J. Collins (1997)].

The transverse momentum $\mathbf{p}_\mathrm{T}$ of a particle is another Lorentz invariant quantity under a boost along the beam axis, by virtue of being the momentum component perpendicular to said axis. It is most often used as a the norm $p_\mathrm{T} = \sqrt{\mathbf{p_\mathrm{T}}^2}$ of the vector rather than as the vector itself. It is a very practical variable that can be measured directly for charged particles by observing the curvature of particle traces in a magnetic field parallel to the beam axis in experiments like ALICE.

Transverse momentum p_T and rapidity y, usually together with an azimuth angle φ, encode

if the mass m is known the full four-momentum $(E, \mathbf{p}) = (E, \mathbf{p_T} + \mathbf{p_z})$ of a particle into Lorentz invariant quantities under longitudinal boosts, thanks to Eq. 1.11 and 1.12. Thus, rapidity- and p_T-differentials of invariant quantities like the cross section remain invariant under such a change of frame.

$$E = \sqrt{m^2 c^4 + p_T^2 c^2} \cdot \cosh(y) \tag{1.11}$$

$$p_z c = \sqrt{m^2 c^4 + p_T^2 c^2} \cdot \sinh(y) \tag{1.12}$$

II – The ALICE Experiment

The theoretical context has been set, now the ALICE experiment at the LHC will be presented.

2.1 The Large Hadron Collider

The Large Hadron Collider (LHC) is a 27-kilometre-perimeter double ring of vacuum tubes, the beam pipes, nested inside a magnetic field created by superconducting magnets that guides and accelerates two beams of protons and ion nuclei close to the speed of light in opposite directions [Brüning et al. (2004)]. The two beams intersect in four points, where the particles in the beam are focused down to a ~70 µm transverse radius to allow for collisions to happen [Brüning et al. (2004)]. It is located below France and Switzerland near Geneva, inside a tunnel whose depth varies between 50 m and 157 m. This depth helps reduce the pollution of experiments by the radiation from the atmosphere. Its design was approved by the European Organization for Nuclear Research (CERN) in 1994, and following about a decade of construction the LHC saw its first collision in 2010.

The protons are initially hydrogen atoms H in a pressurised hydrogen bottle. They are ionised into H^- and accelerated to 160 MeV in a linear particle accelerator that feeds them to the Proton Synchrotron Booster (PSB) that in turn strips them of their electrons and brings them to 2 GeV. They are then moved into the Proton Synchrotron (PS) that accelerates them to 25 GeV, then into the Super Proton Synchrotron (SPS) that accelerates them one last time before injection into the LHC to an energy per proton of 450 GeV, ie 900 GeV of total collision energy [Damerau et al. (2014)]. The LHC will then accelerate them all the way to the final collision energy, at a maximum of 7 TeV per proton, a limitation due to the magnetic field available to restrain the trajectory of the high momentum protons. Those elements can be visualised in Fig. 2.1.

The four interaction points where the two rings intersect are home to four major experiments. The CMS experiment (Compact Muon Solenoid) and the ATLAS experiment (A Toroidal LHC Apparatus), general purpose detectors known for their discovery of the Higgs Boson. The LHCb experiment (Large Hadron Collider beauty), an asymmetric detector that tracks high forward rapidity particles and whose main field of study is that of the matter-antimatter asymmetry in the universe. And, last but not least, ALICE, focused on the study of the QGP. Figure 2.2 displays the layout of the four LHC experiments presented above.
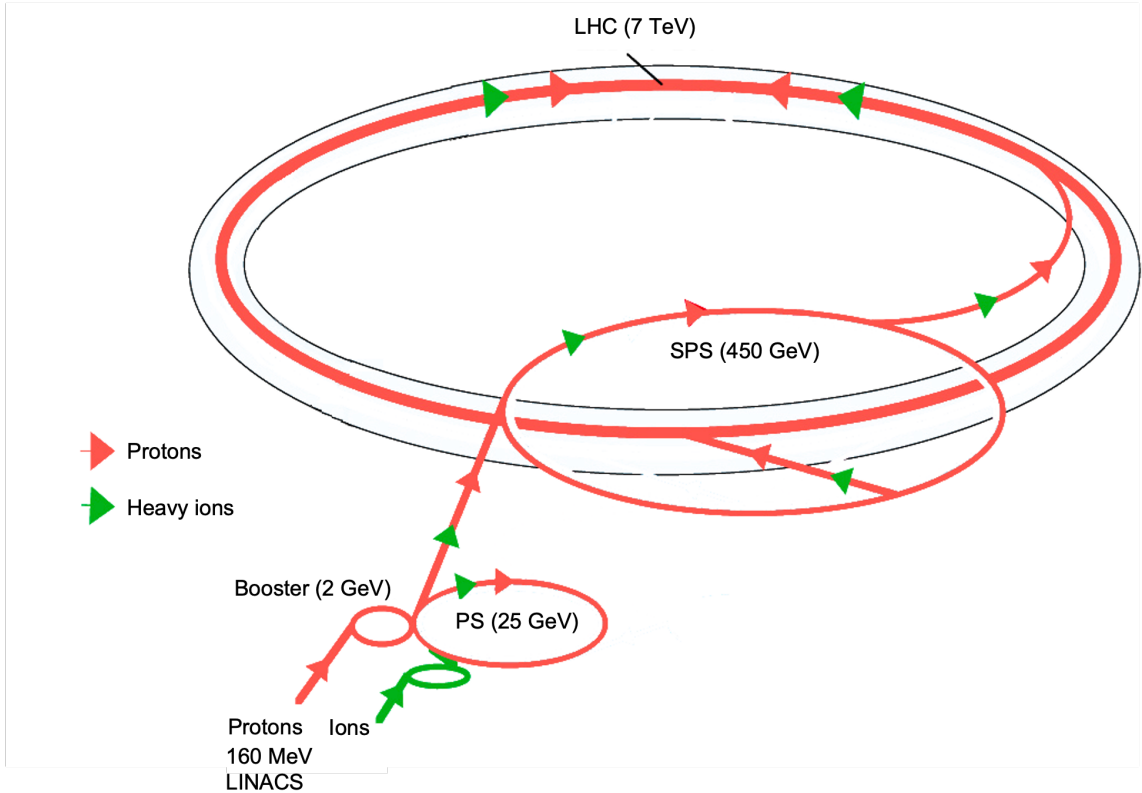
Figure 2.1: The LHC injection complex — taken from [Caron (1993)] and adapted.

2.2 ALICE detector

ALICE (A Large Ion Collider Experiment) is one of the giant detectors built at one of the beam pipes intersection points of the LHC. The general-purpose detector was designed to study the properties of the QGP through the collisions of high energy beams of heavy-ion nuclei. The ALICE programme also includes proton-proton (pp) collision runs to use as a baseline measurement, and proton-nucleus (p-A) collisions, which were originally thought of as a way to distinguish the effect of the initial large nucleus, also called cold nuclear matter effect, from the effect of the quark-gluon plasma, presuming it was not present in p-A collisions. Recent results show a more complex reality, with hints of QGP signatures where they were not expected both in pp and p-A collisions [Adam et al. (2017) for the example of pp].

The detector gives insight into the quark-gluon plasma properties thanks to various probes, making use of its superb particle identification capabilities and p_{T} resolution at low transverse momentum. The strangeness production enhancement has been presented in section 1.5, and the suppression of J/ψ and the quenching of jets have been briefly mentioned in the same section.

With the recent upgrade of the detector, ALICE will be doing precision measurements of charm and beauty quarks in the QGP [Noferini (2018)].
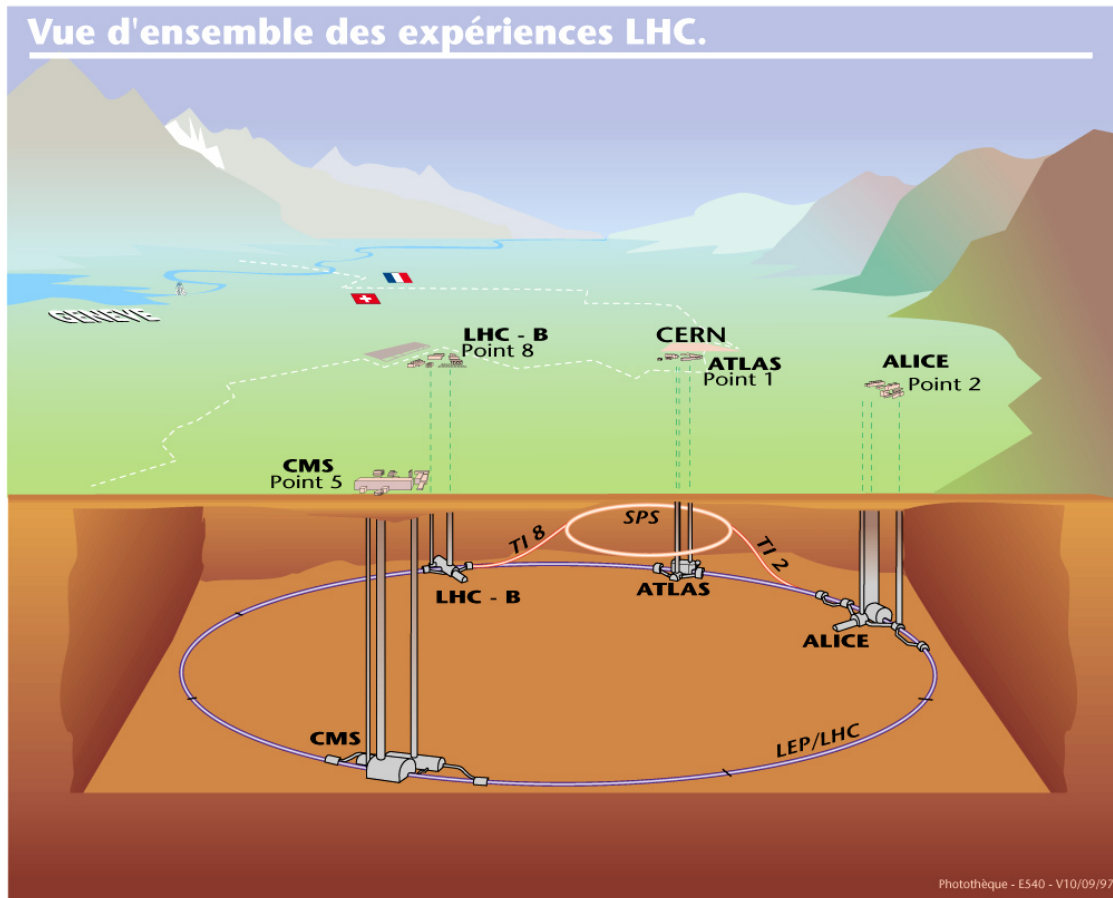
Figure 2.2: Overall view of the LHC and its experiments — taken from [Caron (1998)].

2.2.1 Upgrade of ALICE

The LHC underwent a three-and-a-half-year-long break, during which the whole facility underwent maintenance and upgrades with the LHC Injector Upgrade (LIU) preparing the way for the High-Luminosity LHC. The main change that had to be addressed by an upgrade of ALICE in parallel is the increase in the average interaction rate from 500 Hz to 50 kHz for lead-lead collisions [Abelev et al. (2014b)] in Run 3, the name of the period of activity ALICE enters in 2022 after the restart of the LHC. Detectors had to be upgraded to handle this high rate and the processing of data significantly changed. The new physics objectives involve very rare events, i.e. requiring a lot of data. For that reason, all collisions should ideally be recorded [Buncic et al. (2015)]. The trigger method previously used has a lot of advantages in that it allows for example to easily distinguish between two collision events. Unfortunately, this method introduces a lot of dead time. Dead time is the fraction of time spent by the detector not recording data. It arises from an intrinsic recovery time of the electronics or detector medium, from data-processing and storage or various other causes, and reduces the number of collision events actually seen. This is where a continuous readout environment steps in. The detector outputs are read continuously, regardless of the detection of the occurrence of an interaction, and are attributed data frames. This removes the dead time currently introduced by the trigger process. Unfortunately, this introduces an ambiguity in the attribution of a track to a collision event, as two collision events can happen within a time interval smaller than the readout time of a detector, whereas the trigger method made sure to capture only single collision events.

To process all this data, the Run 2 offline reconstruction would ask for much more data storage than what could be realistically made available, as storing every event for an offline analysis would require facilities that could handle more than 1TB/s of data flow accumulating over several years for events estimated to represent approximately 20 Mbytes of data each [Abelev et al. (2014b)] (in the case of Pb-Pb collisions). A new reconstruction framework named O2 [Eulisse et al. (2018)] has been designed that sees the data of every event compressed into a limited number set of its important characteristics, for a planned event size of about 1 MByte per event, i.e. a reduction of a factor 20 [Abelev et al. (2014b)]. This online reconstruction will see part of the analysis done before storage of the data.

2.2.2 Luminosity, beam structure and event rate

The event rates of 50 kHz that have been mentioned so far do not reflect a precise clock of collisions happening every 20 µs. They are averages of a more complex structure dictated by the LHC design.

The beams are not streams of uniform particle density. They are organised in regularly

spaced and focused bunches of particles, in a structure that arises from the injection scheme that oversees how protons or ion nuclei are injected in the LHC beam. A simplified version of one possible such scheme in Run 3 for Pb-Pb, that has been used by [Lippmann (2014)] as a baseline to look at the effect of the continuous readout on particle reconstruction, and is currently used for the Run 3 Monte Carlo simulations, is pictured in Fig. 2.3. A total of 12 identical bunch trains each made out of 48 bunches separated from each other by an empty bunch slot and followed by 96 empty bunch slots, with an additional gap of 630 empty bunch slots after the trains, make for an orbit. The charge distribution inside an occupied bunch slot follows, as a first approximation, a sharp Gaussian distribution of standard deviation 0.2 ns [Efthymiopoulos et al. (2021)], and bunch slots are separated from each other by 25 ns. Each train is thus 4.8 µs-long, and a whole orbit around the LHC ring takes a proton or lead bunch 89 µs.

A more recent scheme is presented in the design report of the LHC Injector Upgrade (LIU, [Coupard et al. (2016)]), the projected scenario has 1152 bunches spread among the bunch slots per orbit. A little more than double the number of bunches as in the simplified scheme that has been detailed, but the general structure of trains of bunches and the spacing between two bunch slots remains the same.

Given this beam structure, and using the concept of luminosity, the interaction rate per bunch crossing can be calculated, and from this the average interaction rate.

The luminosity $\mathcal{L}$ of a beam is a measure of the focus and intensity of the beam. It is a characteristic of the beam itself and determined by the experimental setup. It is the convolution of the two beam density distributions multiplied by a kinematic factor that accounts for their relative speed, in the simplified scenario of head-on colliding bunches, two times the revolution frequency of the beams. The luminosity is the proportionality factor between the number of event per second $\frac{dR}{dt}$ and the cross section σ_{event} of such an event, as shown in Eq. 2.1 [Herr and Muratori (2006)]. The cross section in particle physics represents an effective area for a particle when computing the probability for a physical process, involving said particle, to happen in a scattering experiment. It does not represent an actual particle size, and varies with the energy of the particle and the physical process being probed.

$$\frac{dR}{dt} = \mathcal{L} \cdot \sigma_{event} \tag{2.1}$$

It is a very practical variable: once integrated over a period of time, the luminosity allows a count of the expected number of events of a physical process by multiplying the luminosity by the cross section of that process, if it is known. The processes that can be counted that way can be for example the production of a pion starting from a proton-proton interaction, or simply the interaction between two protons from the colliding beams. This is useful when a rare process is being considered for new measurements: the expected number of such event
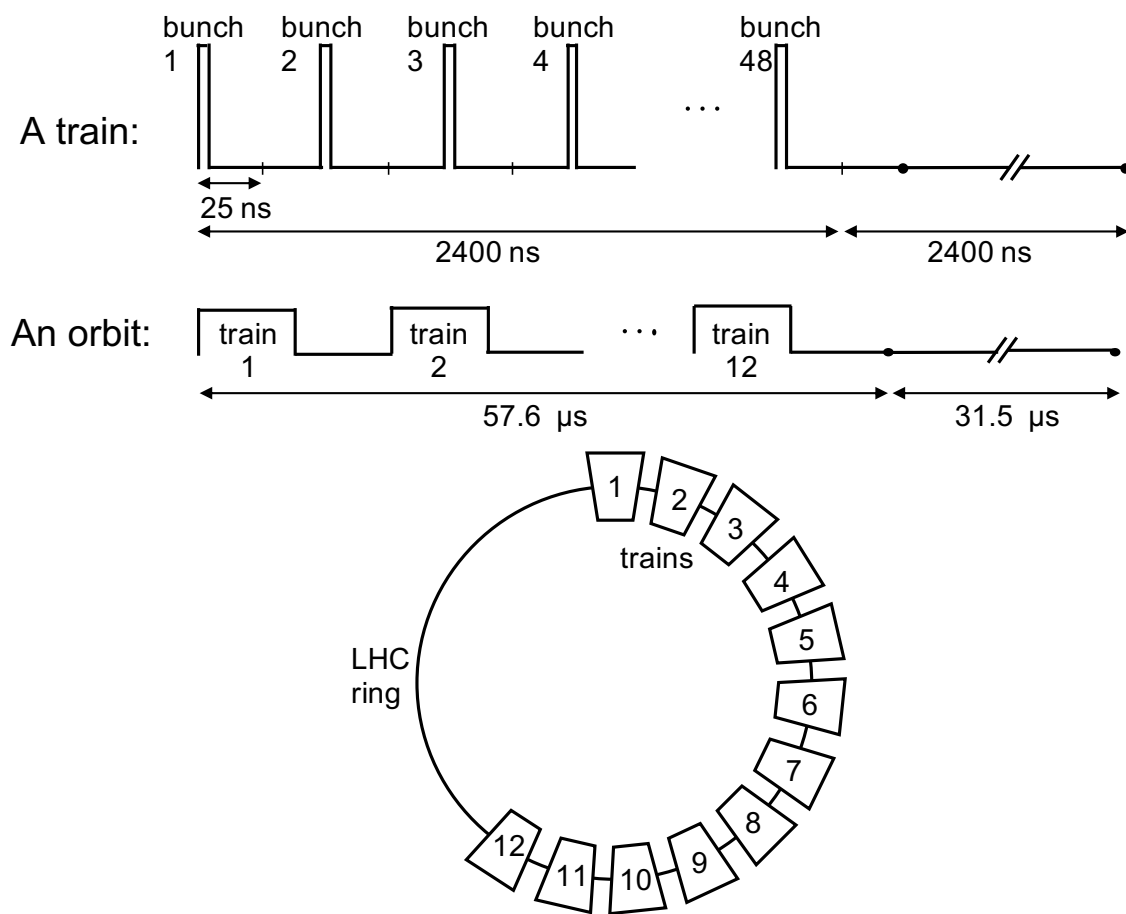
Figure 2.3: Schematic of the LHC filling scheme example given.

with the available or upcoming data can be deduced, and the feasibility of an analysis of it can be assessed accordingly.

A formula for $\mathcal{L}$ can be derived given some assumptions about the configuration of the accelerated beams. Figure 2.4 shows a schematic view of two bunches about to cross. Each bunch is described by a moving 3-D density distributions $N_1\rho_1(x, y, s, s_0)$ and $N_2\rho_2(x, y, s, s_0)$, with $s_0 = c \cdot t$ where c is the speed of light encoding the translation with time of those distributions along their trajectory, here assumed to be a straight line (in reality, the beams collide at a slight angle to allow crossing of the beams). $\mathcal{L}$ is defined as Eq. 2.2:

$$\mathcal{L} = 2N_1 N_2 N_b \cdot f \cdot \iiiint\limits_{x,y,s,s_0} \rho_1(x, y, s, s_0)\rho_2(x, y, s, -s_0)\, dx\, dy\, dz\, ds_0 \qquad (2.2)$$

where N_b is the number of bunches in an orbit and f is the revolution frequency of bunches around the collider.

[Herr and Muratori (2006)] shows that the formula in Eq. 2.2 can be simplified into Eq. 2.3 by assuming head-on collisions and identical uncorrelated Gaussian densities in all planes for every bunch:

$$\mathcal{L} = \frac{N^2 f N_b}{4\pi \sigma_x \sigma_y} \qquad (2.3)$$

where N is the number of particles in a bunch, and σ_x and σ_y the standard deviations of the Gaussian-shaped bunches in the transverse plane. The planned number of particles per bunch is $\sim 1.7 \times 10^8$ for Pb-Pb, and typical standard-deviations in Run 2 were $\sim 17\,\mu m$. With an orbit $T = \frac{1}{f} = 89\,\mu s$ as presented above and the $N_b = 1152$ bunches in an orbit, one can calculate a luminosity $\mathcal{L}$ of $\sim 1 \times 10^{28}\,\mathrm{cm^{-2}s^{-1}}$. Which is in line with the figure given by [Abelev et al. (2014b)]: $6 \times 10^{27}\,\mathrm{cm^{-2}s^{-1}}$. A formula closer to reality for $\mathcal{L}$, with fewer assumptions, can be found in [Aberle et al. (2020)].

The number of collisions per bunch crossing μ_{BC} can also be expressed as a function of the beam parameters by decomposing the average collision rate as done in Eq. 2.4:
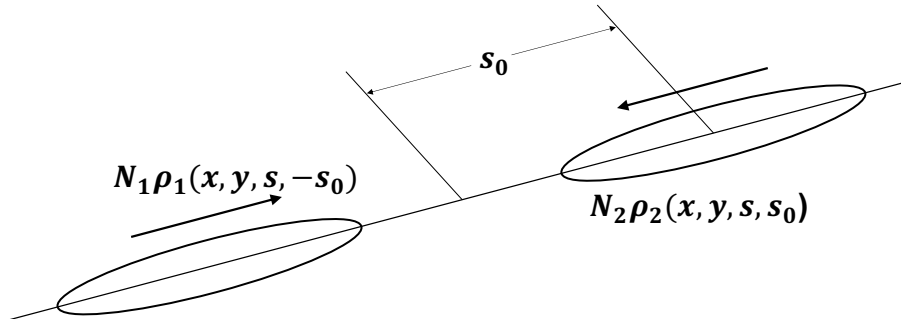
Figure 2.4: Schematic view of a colliding beam interaction — inspired by [Herr and Muratori (2006)].

$$\frac{dR}{dt} = f N_b \cdot \mu_{BC} \qquad (2.4)$$

and combining Eq. 2.4, Eq. 2.1 and Eq. 2.3 into Eq. 2.5:

$$\mu_{BC} = \sigma \cdot \frac{N^2}{4\pi\sigma_x\sigma_y} \qquad (2.5)$$

It should be noted that this number of collisions per bunch crossing μ_{BC} is an average. For the actual distribution, one can consider the count of collisions observed per bunch crossing as a Poisson distribution, that can model a Binomial distribution in the limit of fixed average (μ_{BC}) and very large number of trials (the evaluation of which is very difficult) according to the Poisson limit theorem [Papoulis and Pillai (2002)]. Thus is written the probability $I\!\!P(k)$ of having exactly k collisions in a bunch crossing in Eq. 2.6:

$$I\!\!P(k) = \mu_{BC}{}^k \cdot \frac{e^{-\mu_{BC}}}{k!} \qquad (2.6)$$

Of interest for the design of the tracking algorithm in an online reconstruction is the distribution of time differences between two consecutive collisions. It will dictate the ambiguity of the attribution of a collision to the reconstructed tracks. Figure 2.5 shows this distribution for an average interaction rate of 50 kHz.

2.2.3   Detector Layout

The ALICE detector, of a size of about $16\times16\times26\,\mathrm{m}^3$, is made out of several parts [Aamodt et al. (2008)]. The main tracking detectors are the Inner Tracking System (ITS) made of staves of silicon detectors with high position resolution arranged in seven concentric cylindrical layers and the Time-Projection Chamber (TPC), a gas-filled chamber where the passage of the charged products of the collision is measured. Enveloping the TPC are additional detectors that help with the tracking of the particles, their identification, the measurement of their energy and many other observables, or the reduction of background. Those central barrel detectors are embedded in the magnetic field of a strength of $0.5\,\mathrm{T}$ generated by a solenoid magnet, that bends the trajectories of charged particles, the curvature of which can help identify the charge and momentum of such particles. On both side of the central barrel, the Fast Interaction Trigger detector (FIT) monitors the luminosity, the collision timestamps and the centrality of Pb-Pb collisions, i.e. how head-on they are. Fig. 2.6 shows the arrangement of the ALICE detectors around the central beam pipe.
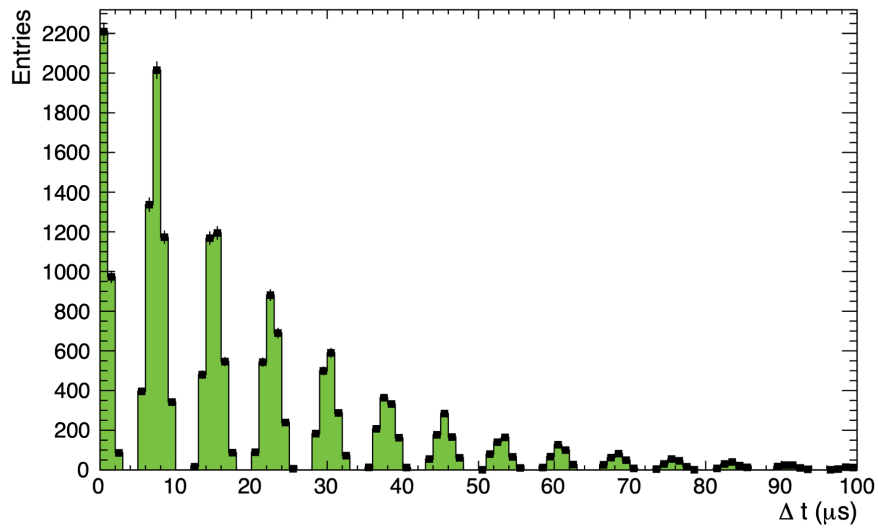
Figure 2.5: Distribution of time differences between two consecutive collisions for an interaction rate of 50 kHz — taken from [Lippmann (2014)].
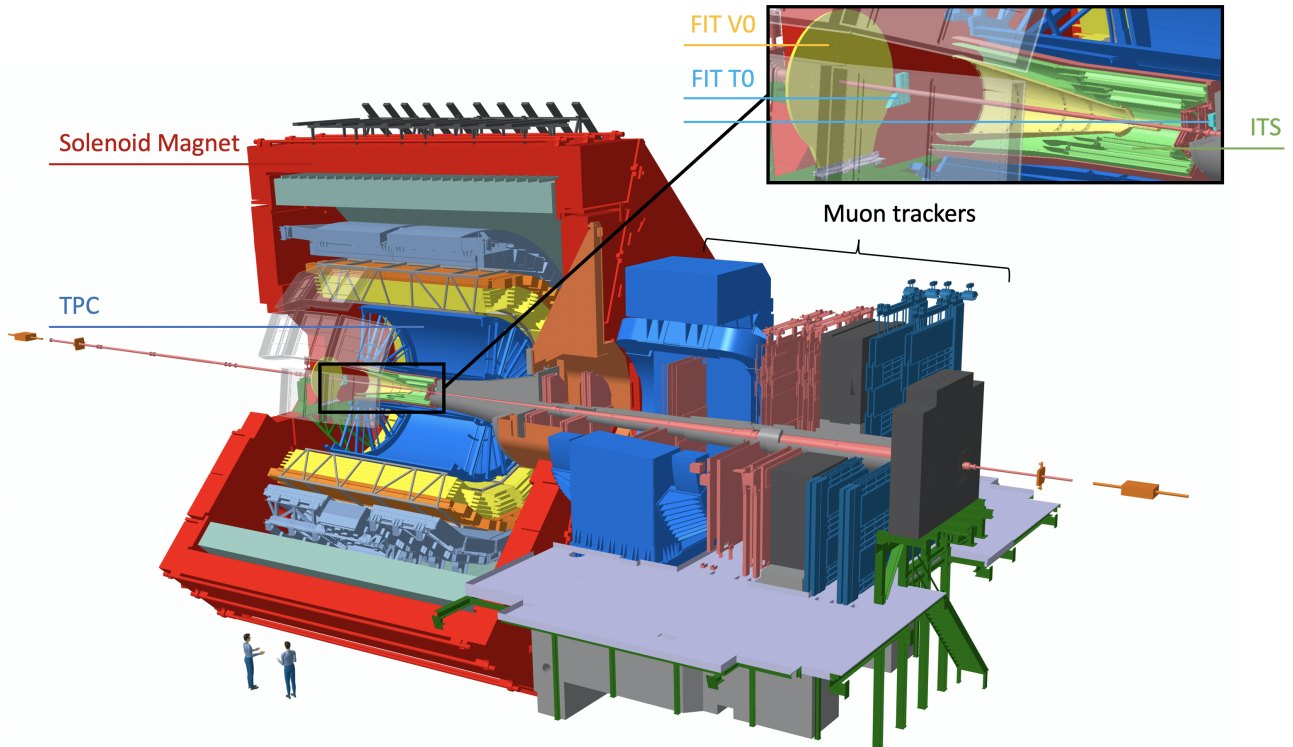
Figure 2.6: ALICE Schematics in Run 3, with zoom on the ITS and FIT detectors.

2.2.4   Coordinate system in ALICE and pseudorapidity

A global coordinate system is used in ALICE to encode the trajectories of particles or the positions of the detectors. That system is described in [Betev and Chochula (2003)]: it is a right-handed orthogonal Cartesian system, with a point of origin at the beam interaction point. The z axis is parallel to the beam direction, pointing opposite to the muon spectrometer. The x axis is perpendicular to the beam direction and aligned with the local horizontal, and pointing towards the accelerator centre. Finally, the y axis is perpendicular to the x and z axes, and points upwards. A polar coordinate system is also used, for which the polar angle θ is defined as the angle between the z axis previously defined, and the azimuth angle φ is the angle between the x axis and the projection of the position vector of length r onto the xy plane. Figure 2.7 shows a sketch of those coordinate systems superimposed onto the central barrel detectors.

Instead of the polar angle θ, the pseudorapity variable η is used to identify the angle of a particle with the beam line. It is defined as in Eq. 2.7:

$$\eta = -\ln\left(\tan\frac{\theta}{2}\right) \tag{2.7}$$

The pseudorapidity has the property that when the transverse momentum of a particle is large compared to its mass, it converges towards the rapidity of this particle as introduced in section 1.6.3, but does not depend on anything but the polar angle and can thus be used as a spatial coordinate.

2.2.5   ITS

The ITS is made out of seven concentric cylinders of silicon pixel detectors surrounding the beam pipe [Abelev et al. (2014b)], placed at radii of 2.3 cm, 3.1 cm and 3.9 cm for the inner layers, 19.6 cm and 24.5 cm for the middle layers, 34.4 cm and 39.3 cm for the outer layers [Kushpil (2020)]. The inner layers have a length of 27.1 cm, the middle layers a length of 84.3 cm, and the outer layers a length of 147.5 cm. They allow the tracking of particles close to the beam line in the pseudorapidity interval $|\eta| < 1.3$ [Liu (2022)] with a high precision going as small as 4 μm for the intrinsic resolution of the central layers, while at the same time reducing the scattering of the products of the collision by the detectors as much as possible. This is possible thanks to a thickness as low as 0.35% of the radiation length of the material used per layer, a measure of the energy loss of high energy particles when passing through a material, standardised for electrons as the mean length to reduce its energy by a factor $1/e$ [Gupta (2010)]. Its readout time is 10 μs for Pb-Pb and 1 μs for pp [Liu (2022)]. Low enough to capture less than one Pb-Pb collision every cycle on average with the expected ion interactions rate of 50 kHz, and about two collisions for pp with the expected event rate of 200 kHz [Abelev et al. (2014b)]. Fig. 2.8 gives a schematic view of the ITS detector in Run 3.
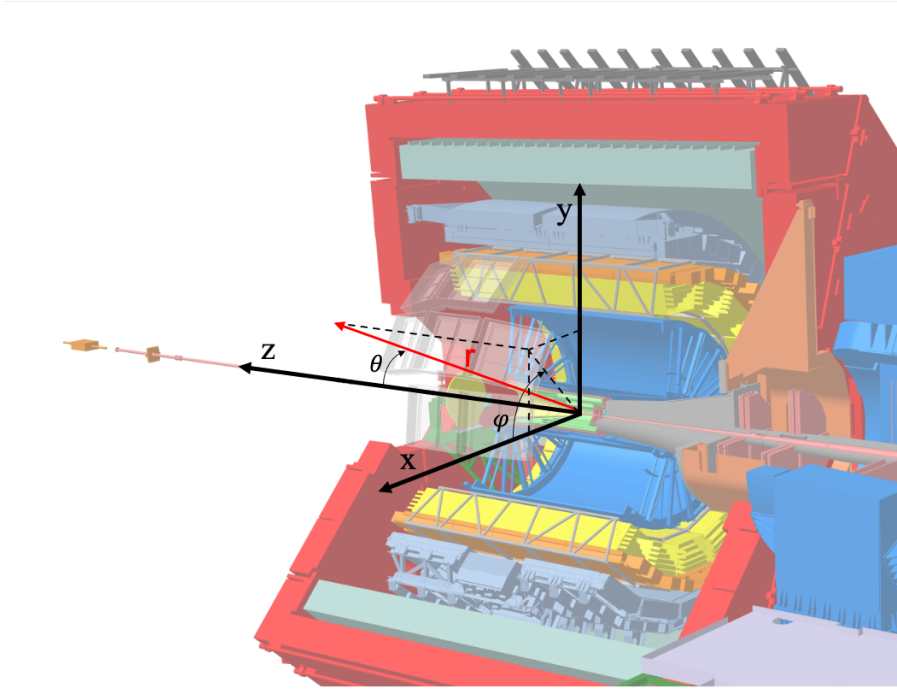
Figure 2.7: ALICE coordinate system.

The ITS as presented above is the result of an important upgrade that brought the innermost layer closer to the beam line (the innermost layer was located at a radius of 3.9 cm in Run 1), increased the total number of layers (from six in Run 1 to the seven presented in the previous paragraph), reduced the material budget (the current 0.35% per layer was previously 1.14% per layer). Those changes brought important performance gains in the tracking efficiency and momentum resolution at low p_{T}, as well as the pointing resolution as illustrated in Fig. 2.9.

Some of the main tasks of the ITS include the precise localisation of the primary vertex inside the beam line, improving the momentum and angle resolution of tracks reconstructed in the TPC, the reconstruction of secondary vertices of decays of particles too short-lived to reach the farther TPC.

2.2.6 TPC

The TPC is a large cylindrical field cage, 500 cm long with an inner radius of 85 cm and outer radius of 250 cm, filled with a mixture of gas that is ionised by the passage of product particles from the collisions inside the beam line. It covers the pseudorapidity range $|\eta| < 0.9$ for full radial track lengths, up to $|\eta| < 1.5$ for reduced track length [Aamodt et al. (2008)]. An electrode sitting in the centre of the revolution axis and dividing the chamber into two halves creates two electric potential gradients of about 400 V/cm (one on each half) that send the electrons from the ionisation of the gas drifting to the readout chambers adorning the closest end plate of the cylinder [Abelev et al. (2014b)] at a speed v_{drift} of 2.56 cm/µs. Those readout

Outer layers

Middle layers

Inner layers

Beam pipe

Inner Barrel

Outer Barrel

Layer 1,2,3

Layer 4,5

Layer 6,7
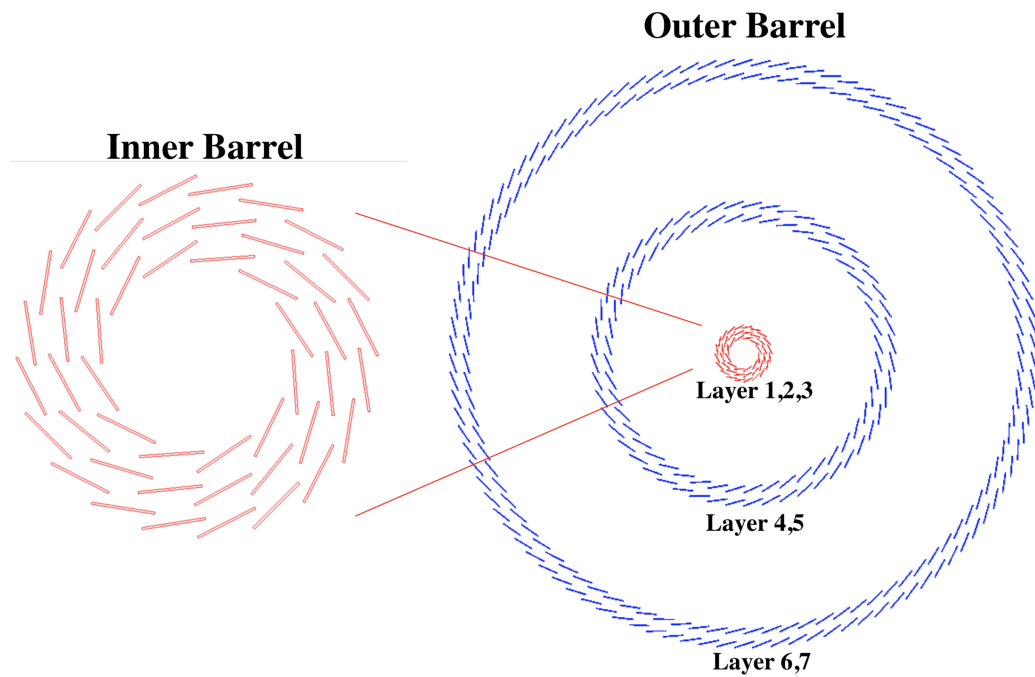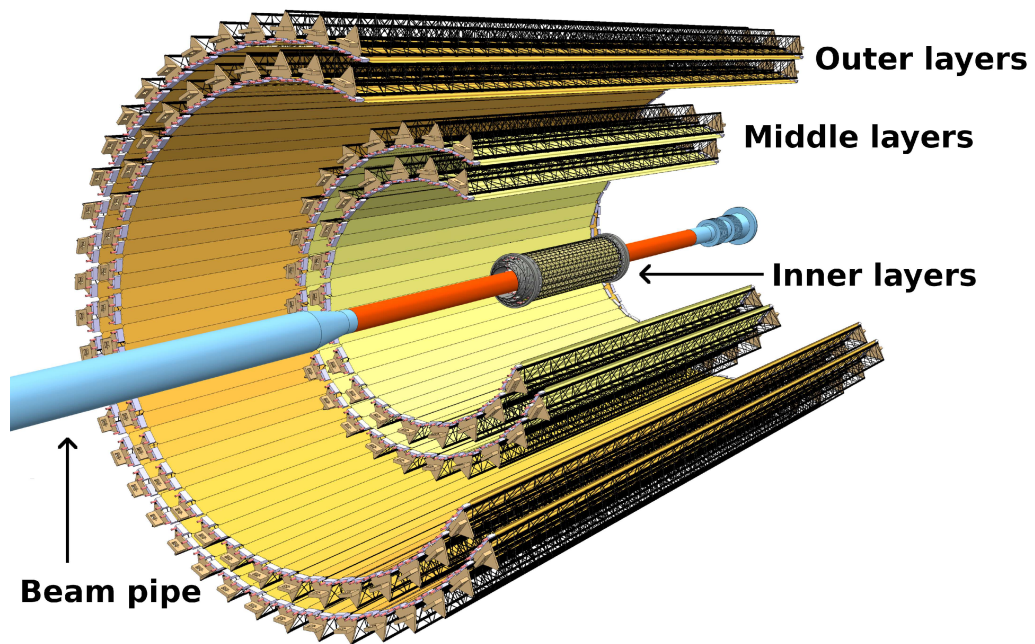
Figure 2.8: Schematics of the upgraded ITS (top) with radial view (bottom) — taken from [Colella (2020) and Abelev et al. (2014b)].
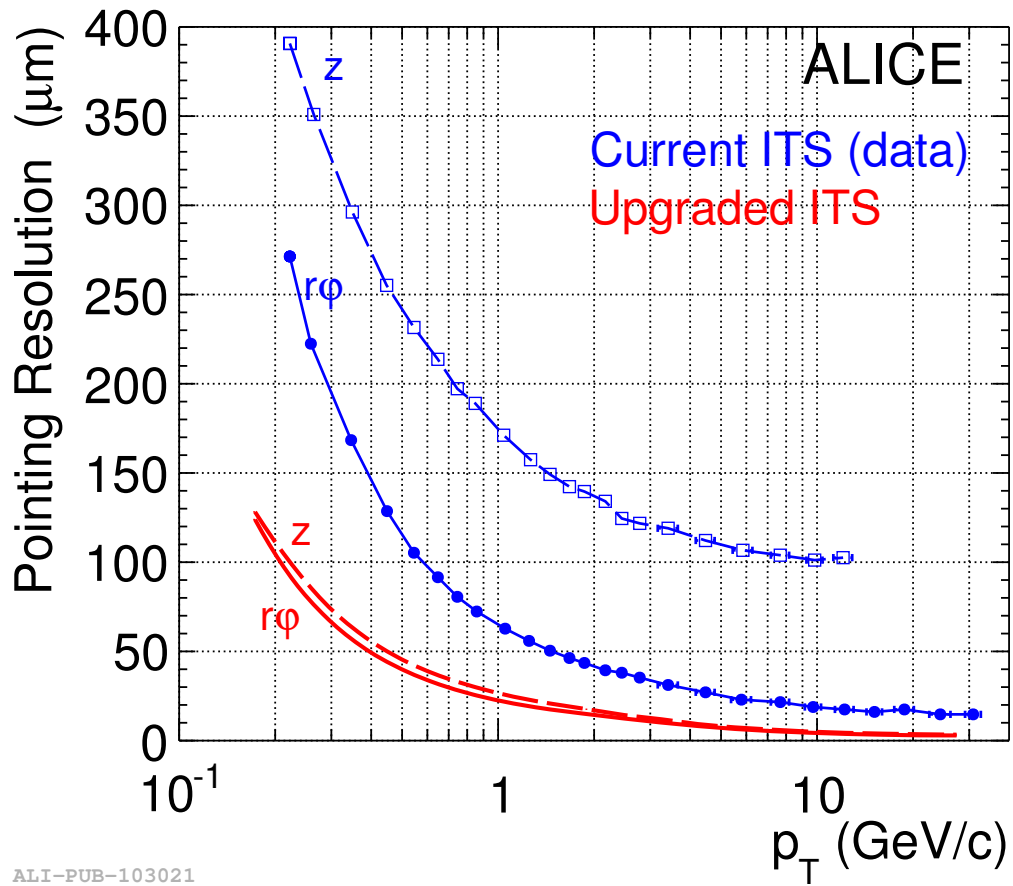
Figure 2.9: Impact parameter resolution ($r\phi$ and z) for current ITS (PbPb data) in blue and upgraded ITS in red, as a function of p_{T}.

chambers are made out of Gas Electron Multipliers (GEM) foils: 3-layer sheets (metal-insulator-metal) etched with a matrix of ~70 μm-wide holes. Their role is to amplify the signal received on the end plates so that the readout planes can resolve the signal, by multiplying the electrons through an avalanche process, where electrons accelerated by intense and localised electric fields in the GEM holes ionise the ambient gas and free new electrons that will themselves ionise the gas, and create a chain reaction [Sauli (1997)]. The size of the readout pads on the end plates dictates the intrinsic radial resolution of the TPC: from $4 \times 7.5 \, \text{mm}^2$ close to the centre to $6 \times 15 \, \text{mm}^2$ on the outer edge [Lippmann (2014)]. This resolution is further limited by the spread of the electron clusters reaching the readout plane. Figure 2.10 gives a schematic view of the TPC detector.

The main tasks of the TPC are to track the trajectories of the particles inside the volume covered by the chamber, to give an accurate measurement of their momenta, as well as measuring the ionisation energy loss throughout their trajectories. The latter is an important tool for particle identification (PID) as the evolution of this ionisation energy loss $\frac{dE}{dx}$ as a function of the particle momentum follows a different distribution for each particle species (the mean of this distribution is described by the Bethe-Bloch formula, see [Tanabashi et al. (2018)]). This power of discrimination between different particle species can be visualised in Fig. 2.11, where the 2D distribution follows the lines described by the Bethe-Bloch formulae for each species.

2.2.7 FIT detector

The Fast Interaction Trigger detector consists of three subsystems [Rojas Torres (2022)]. Two of those, the detectors FV0 and FT0, are important for the precise measurement of collision time, and in Pb-Pb collisions for the determination of the centrality, a measure of how head on a collision is. The third one, FDD, will help monitor the beam as well as contribute to measurements of categories of events that are not studied in this thesis [Rojas Torres (2021)]. All three are shown in figure 2.12.

On one side of the central barrel is the FV0 detector, $3.16 \, \text{m}$ away from the interaction point, a plastic scintillator ring with an inner and outer radius of $8 \, \text{cm}$ and $148 \, \text{cm}$ that takes advantage of fluorescence: when an incoming particle ionises the medium, some of the ionisation energy is absorbed by special compounds in suspension in the solid polymer matrix, called fluors, that re-emit this energy in the form of light. A grid of optical fibres bring this light to photomultiplier tubes. The scintillator ring covers the pseudorapidity range $2.2 < \eta < 5.0$. This large angular acceptance makes the FV0 an important detector for centrality and collision plane determination.

The FT0 detectors is made out of two $2 \, \text{cm}$ thick arrays of Cherenkov quartz radiators surrounding the beam pipe, $3.3 \, \text{m}$ and $0.819 \, \text{m}$ away from the interaction point, that capture particles on each side of the central barrel in the pseudorapidity ranges $-4.9 < \eta < -3.3$ and
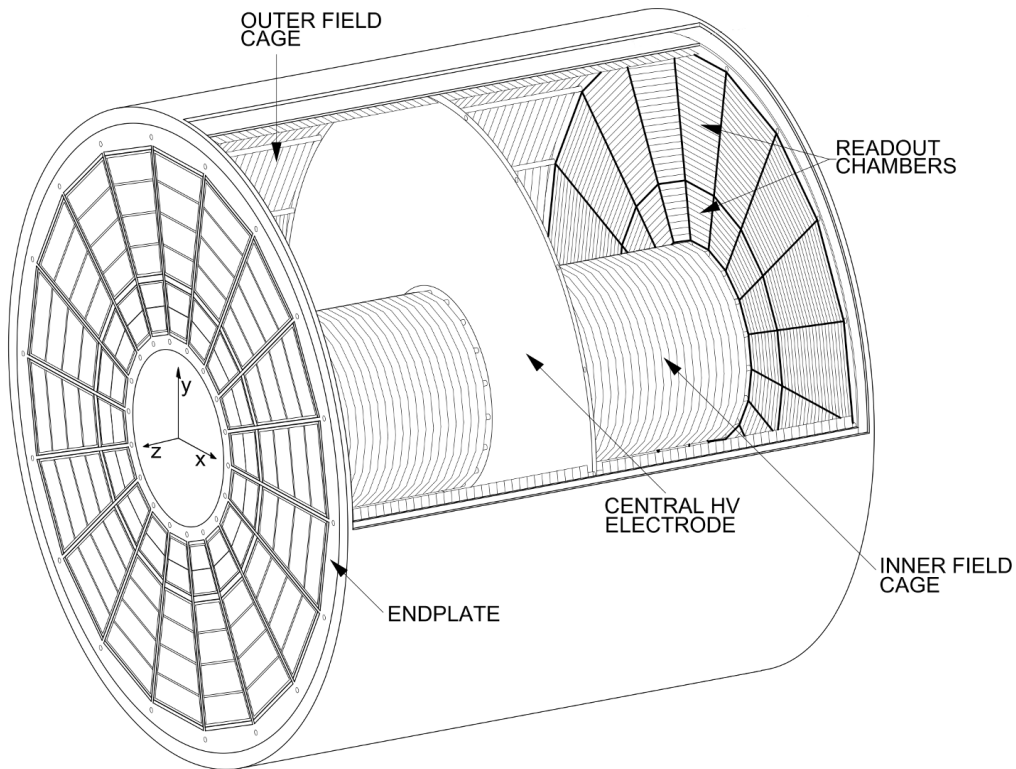
Figure 2.10: Schematic view of the TPC — taken from [Alme et al. (2010)].

$3.5 < \eta < 4.9$. The quartz radiators are coupled to light sensors that collect the Cherenkov light emitted in a cone along its path by the charged particles produced in the collision, as they propagate through the quartz medium. The Cherenkov phenomenon appears when a charged particle propagates in a medium above the phase velocity of light in this medium. It manifests as a cone of light being emitted along the path of the particle. The light sensors are microchannel plates photomultiplier tubes: plates with pores about 25 µm large (the microchannels) that act as miniature photomultiplier tubes [Melikyan et al. (2020)]. FT0 has a time resolution better than 50 ps for a single particle, which makes it a crucial part in the precise determination of the collision timestamp. The timing information is also used to distinguish actual beam-beam events from beam-gas events, results of the interaction of the beam with the residual gas from the vacuum in which said beam propagates [Alemany-Fernández et al. (2009)].

2.3 The new O2 computing framework and data model

The data gathered by the detectors electronics, expected to amount to about 1.1 TB/s, is first fed to the First Level Processors (FLP) of the O2 facility that split the readout into small time divisions called Sub-Time Frames (each FLP produces one Sub-Time Frame). Local calibrations are carried out at this stage for the detectors. The raw data from the TPC, main contributor to the data flow as shown in Table 2.1 is also compressed into clusters, synthetic representations of collections of adjacent hits (in time and position) on the readout chambers.
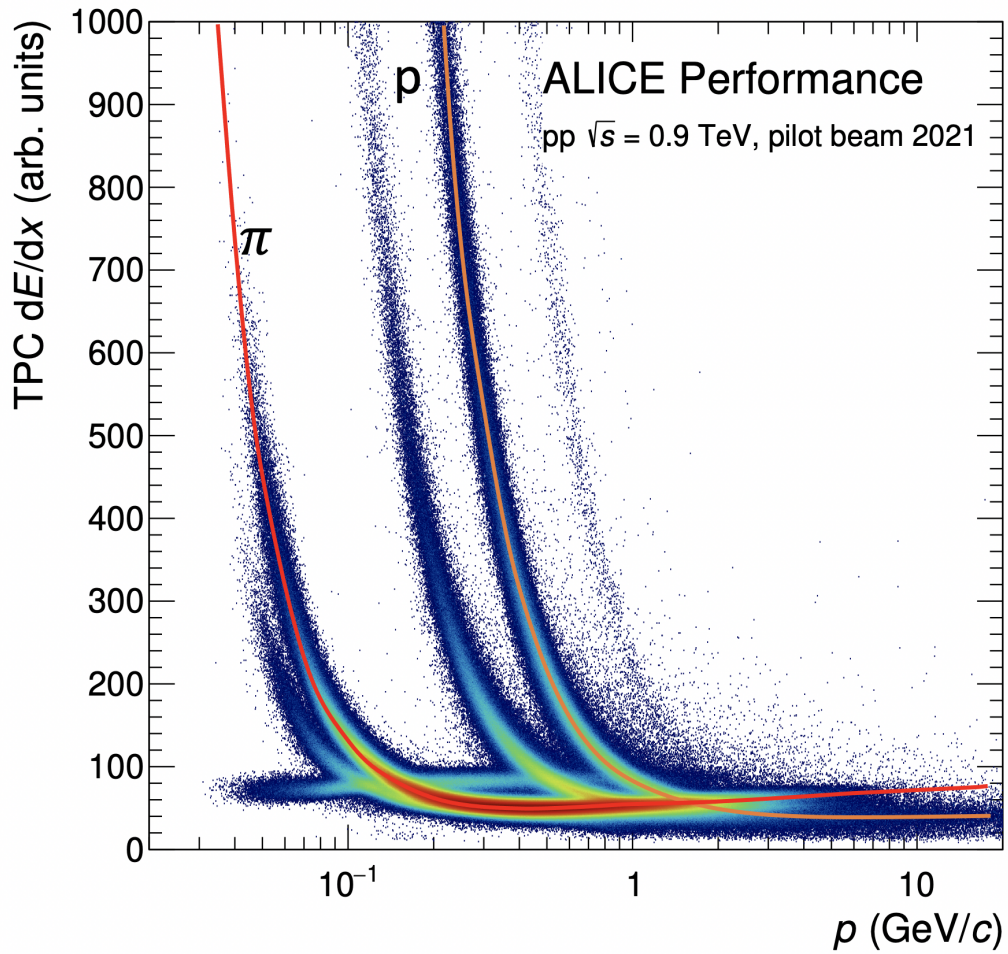
Figure 2.11: Ionisation energy loss of a particle in the ALICE TPC as a function of its momentum, for pp collisions at $\sqrt{s_{NN}} = 0.9\,\mathrm{TeV}$ — the Bethe-Bloch parametrisations are sketched for pions and protons.
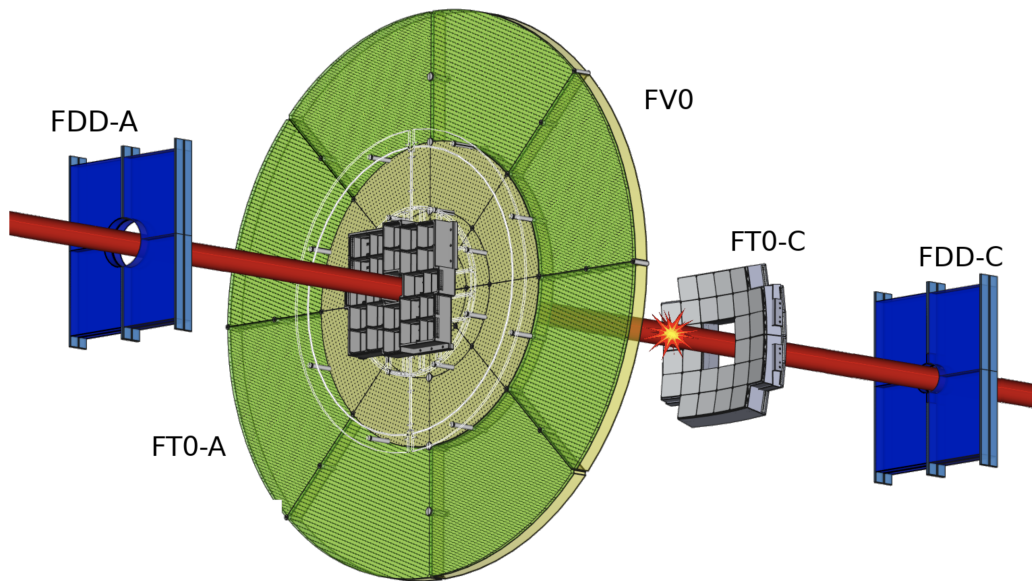
Figure 2.12: Schematic view of the FIT detectors around the beam line (in red) — taken from [Rojas Torres (2021)].

This compressed data now amounting to about 500 GB/s is then sent to the Event Processing Nodes (EPN), in charge of performing track reconstruction for the TPC using the clusters found by the FLPs, in order to greatly reduce the data size originating from the TPC, but also of discarding a lot of the clusters that show no interest to physics analyses (noise, background from beam-gas collisions, etc). The EPNs also aggregate the Sub-Time Frames into larger time divisions called Data Frames (Section 2.3.2 will give more details about those). This is the end of the synchronous analysis. The data output from this synchronous analysis on the EPNs, which amounts to 90 GB/s, is then saved on a storage system used as a buffer between this synchronous step and the asynchronous one. The rest of the reconstruction (reconstruction of tracks in all detectors, matching of tracks between the different detectors, etc) is done asynchronously, using a small subset of EPNs dedicated to it during data taking, or all of them when data taking is not ongoing. A visual summary of those steps can be seen in 2.13, and more details on the whole data processing in O2 can be found in [Buncic et al. (2015)].

The data is saved at the end of the asynchronous process in AO2D files, short for Analysis Object Data files with a wink to O2, in the form of a collection of tables, in which a row corresponds to an entry and the columns are the variables saved for those entries, proper to a table. Those tables are related to each other using indices. For example the Tracks table has a CollisionId column that saves the index for track entries to the row in the Collision table of their associated collision (or an error value, -1, in case of ambiguity).

The compression carried out during the synchronous then asynchronous analyses has been done so that only a minimal set of data are saved in a AO2D file. Any quantity that can be inferred during the offline analysis from this minimal set of data will be recalculated during the analysis, and the tables will be extended with corresponding additional temporary columns, or new temporary tables will be created.

Some examples of those tables are as follows. The Collisions table saves in its columns the coordinates of the vertex, the covariance matrix elements of its position, the index to the bunch crossing that saw the collision, saved in the BCs table, the time of the collision relative to this bunch crossing, etc. The V0s table saves in its columns the indices of the two daughter

Detector	Data rate for Pb-Pb collisions at 50 kHz (GB/s)
TPC	1012 GB/s
ITS	40 GB/s
FIT	0.115 GB/s
other detectors	43 GB/s

Table 2.1: Data rates produced by the ALICE detectors assuming Pb-Pb collisions at 50 kHz — numbers taken from [Buncic et al. (2015)].

Detectors electronics

Continuous and triggered streams of raw data   1.1 TB/s

Readout, split into Sub-Time Frames,
and aggregation
Local pattern recognition and calibration
Local data compression
Quality control

FLPs

Compressed Sub-Time Frames   500 GB/s

Data aggregation
Synchronous global reconstruction,
calibration and data volume reduction
Quality control

EPNs

Compressed Time Frames   90 GB/s

Data storage
and archival

Compressed Time Frames   *Reconstructed events*

Asynchronous refined calibration,
reconstruction
Event extraction
Quality control

EPNs

Figure 2.13: Functional flow of the O2 computing system — taken and adapted from [Buncic et al. (2015)].

tracks, one positive and one negative, and the index to the collision it belongs to.

One table, the Tracks table, saves the quantities that have been chosen to define tracks. The following section describes the track model used in O2.

2.3.1   Track model

Tracks are trajectories of particles. They represent a continuum of positions, energy and momenta for their particle. Due to data volume constraints, the particle properties cannot be saved for all of the points along the tracks. Given the propagation of a charged particle inside an electric and magnetic field is well understood, saving the position and momentum of the particle at a single point along the track is enough to reconstruct the whole track during the analysis. The convention chosen is to save those quantities at the point of closest approach to the collision vertex the track belongs to. Given only a single point is saved, the analyser does not know the bounds of the tracks as seen by the detector, and the track can thus be propagated outside those even though it has never been detected there.

2.3.2   Data frames

The data collected in Run 3 and saved in the AO2Ds is organised in data frames that span 20 ms each. Each data frame sees about 1000 Pb-Pb events (due to the average event rate of 50 kHz), which makes for a very large number of tracks to be assigned to their corresponding collision vertex. Figure 2.14 shows 2 ms of what the central barrel detectors would see during a Pb-Pb collision run at 50 kHz. In it, can be seen several simulated collision events, each represented in a different colour for better visualisation, with the curved tracks originating from it. The vertices are shifted along the horizontal axis by a factor proportional to their collision time.

2.4   Particle track and vertex reconstruction in continuous readout

The track reconstruction of particle trajectories in ALICE and the determining of collision vertices involves all tracking detectors in the central barrel. The reconstruction of the two main tracking detectors, namely the ITS and TPC, will be presented in this section, along with how the detectors information is combined and the primary vertices reconstructed.
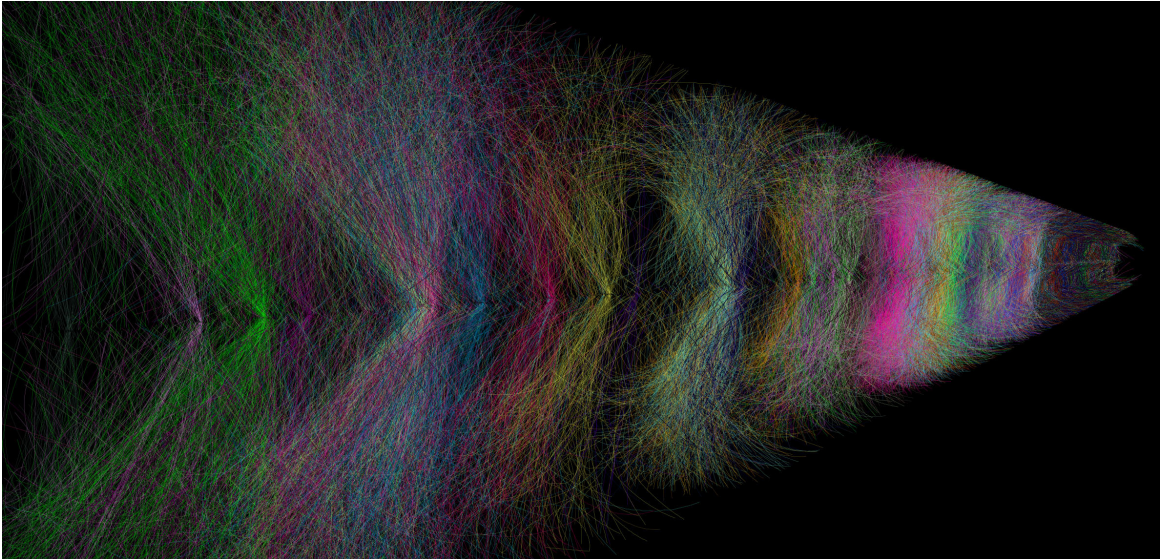
Figure 2.14: View of a simulation of one data frame in the O2 framework — a different colour is assigned to each collision event for better visibility — taken from [Rohr et al. (2018)].

2.4.1   Tracking in the ITS

The tracking of particles inside the ITS is described in [Abelev et al. (2014a)]. An algorithm first searches for collections of adjacent pixel hits, and tags them as clusters. Then an algorithm based on a Cellular Automaton builds track candidates from those clusters. First, all pair combinations of clusters from adjacent ITS layers are first collected as tracklets. Then, each tracklet is extrapolated to the next layer towards the centre of the ITS, by applying to it a track model, and all clusters from that layer that are compatible with the extrapolation are added to the tracklet. This process is repeated for each initial tracklet until the innermost ITS layer has been reached. At this point, the collection of tracklets has become a collection of track candidates, and a track model is fitted to each of the candidates. Various selection criteria are checked to decide whether to keep them, and tracks are required not to share more than a handful of clusters with longer candidates that passed the selection. When candidates of similar length share a large number of clusters, only the one with the best fit is kept.

2.4.2   Tracking in the TPC

Inside the TPC, the ionisation of the gas mixture by a particle tends to form clusters of electrons that appear in the readout plane as roughly Gaussian distributions in time and space. Those clusters are the bricks used to reconstruct particle tracks: starting from the outer edges of the TPC, track candidates are found from aligned clusters, then a Kalman filter [Billoir (1984)] propagates those tracks to smaller radii and sequentially adds to those track the candidates clusters that are compatible with the predicted propagation, refining said propagation as the algorithm reaches smaller radii and as a more accurate version of the track parameters like p_{T}

or energy loss are calculated.

The z-position of the ionisations $z_{ionisation}$ that form the aforementioned clusters can be related to the z-position and the time of the hit on the end plate by the electrons, $z_{endplate}$ and t_{hit} respectively, using the drift speed v_{drift} and the time of the ionisation $t_{ionisation}$ from which the electrons that created the cluster in the end plate originate from, as illustrated in Fig. 2.15 and shown in Eq. 2.8. This is useful if the time t_{vertex} of the collision vertex the track originates from is known, as the track model can be used to calculate $t_{ionisation}$ by extrapolating the track at the vertex. In Run 2, before the upgrade, t_{vertex} was known thanks to triggers that made sure to capture only single collision events. In Run 3, after the upgrade, the continuous readout introduces an ambiguity in the attribution of a vertex to tracks built from those electron hits, with about 5 collisions happening within one TPC maximum drift time window (100 μs) on average. This means the z-position of those ionisations, and thus of tracks, is no longer uniquely defined with the sole TPC information.

$$z_{ionisation} - z_{endplate} = (t_{ionisation} - t_{hit}) \cdot v_{drift} \tag{2.8}$$

Information from other detectors can refine the determination of t_{vertex} during the asynchronous reconstruction phase.

2.4.3 Combination of detector information and primary vertex reconstruction

Once all standalone reconstructions have been run, a global fit is done during which ITS tracks are prolonged in the TPC and matched to TPC tracks, then further matched to other outer detectors. During the ITS-TPC matching procedure, the TPC track is allowed to shift in the z direction within a time interval defined so that the clusters associated with the TPC track are not pushed outside the TPC volume (see Eq. 2.8 for the correspondence between time and z-position). That time interval can be as long as the maximum drift time (100 μs inside the TPC for tracks fully perpendicular to the beam line). An afterburner algorithm then also matches the remaining TPC tracks with ITS clusters that have not been assigned to tracks. The tracks that have been fitted with all the central barrel detectors are called global tracks. Thanks to the high spatial precision of the ITS, and even though the pile-up rate in the ITS readout time is close to 50%, TPC tracks successfully matched with ITS tracks now have good z-position estimate, and thus a good time estimate. The time resolution goes down to ~0.1 μs according to [Buncic et al. (2015)], which reduces the pile-up rate for such tracks to ~2%.

The good position resolutions of global and ITS-standalone tracks allows for a good precision in the determination of the primary vertex position: from 25 μm for pp collisions with low number of tracks to ~3 μm for Pb-Pb collisions with high number of tracks [Abelev et al.
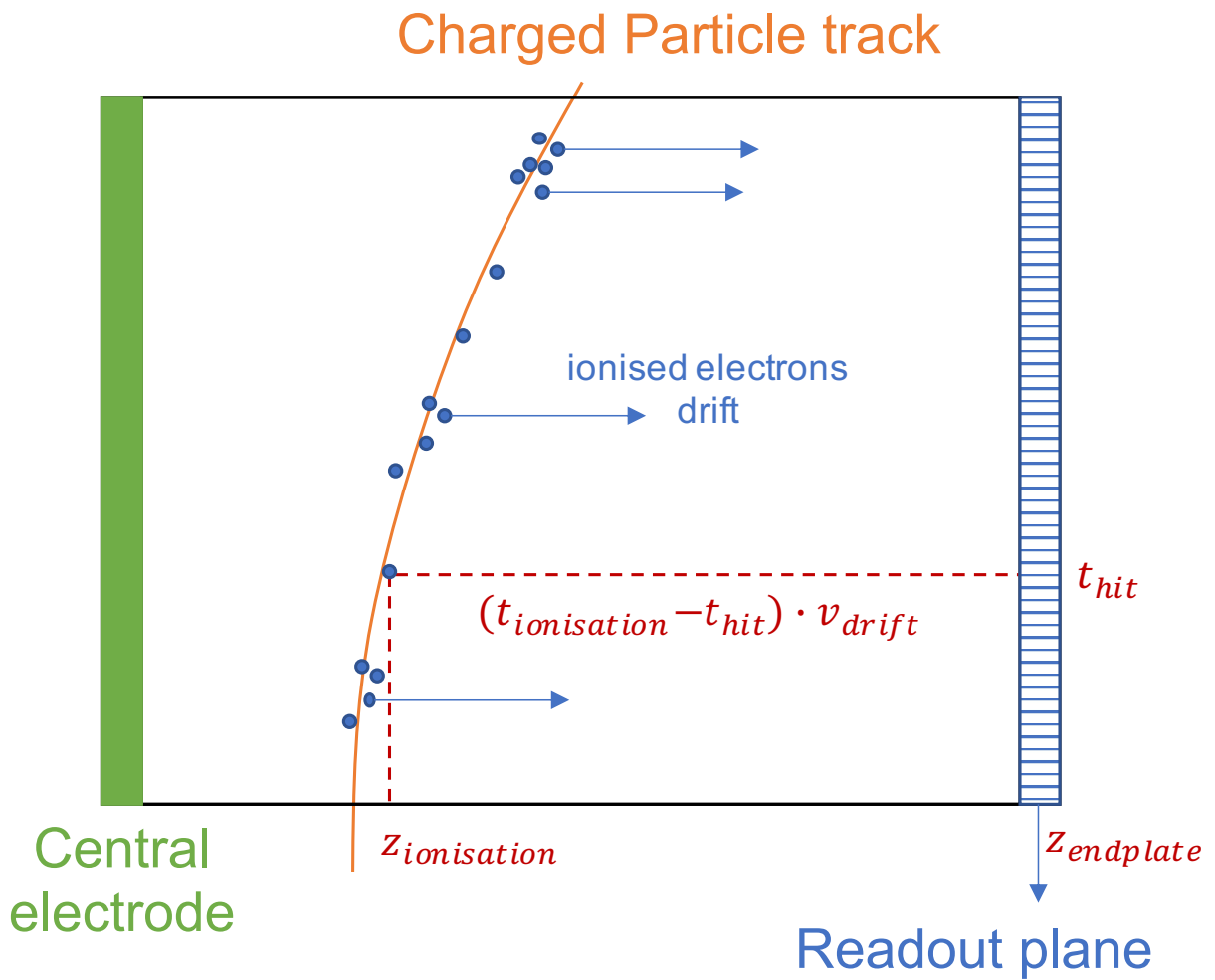
Figure 2.15: Track reconstruction inside a half of the TPC.

(2014a)]. The collision vertices are determined by finding clusters of global tracks and good quality ITS standalone tracks that share an identical timestamp. Then an iterative χ^2 fit of the collision vertex position is done with respect to each track in a cluster. The fit takes into account the track errors through the weights by using the inverse covariance matrices of the tracks [Eulisse et al. (2018)]. The time of the collisions t_{vertex} can be determined using the time estimates of the global tracks used in the fit, crossed with the timestamps measured by the FIT detector with a resolution as low as 7 ps for Pb-Pb or 25 ps for pp as shown by Fig. 2.16 from [Maevskaya (2019)].

For tracks that have not been used in a vertex fit and for which a collision cannot be attributed unambiguously to it based on the timings, the data model simply saves a list of the compatible collisions, and this ambiguity can be taken into account during the offline analysis stage.
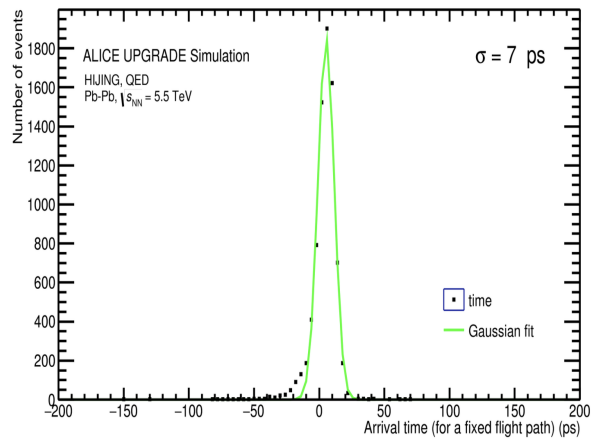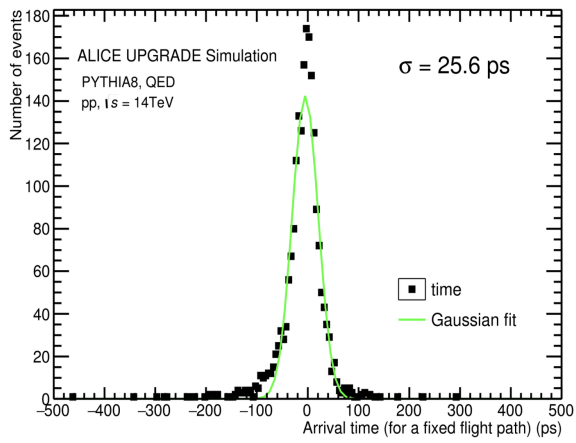
Figure 2.16: Collision time resolution of FIT in Run 3 for pp collisions $\sqrt{s} = 14\,\text{TeV}$ (left) and Pb–Pb collisions, $\sqrt{s_{NN}} = 5.5\,\text{TeV}$ (right).

III − Strange decays - Analysis

The theoretical context has been set and ALICE experiment has been presented. Now the analysis study done for this thesis will be detailed and discussed.

3.1 V0 decays and their reconstruction

The study of strange particles makes use of the characteristic topology of the most common decay channel of the hadrons K_S^0 and Λ, as in addition to being single strange particles themselves, they also are the decay products of the double and triple strange particles $\Xi^\pm$ and $\Omega^\pm$ in their main decay channel. This topology is that of a charge-less particle decaying into two particles of opposite charges. Figure 3.1 shows the topology of the decay $\Lambda \to p + \pi^-$. The charge-less particle, the trajectory of which is represented in dotted line, is invisible to the ITS and the TPC, while the two daughters, charged, leave in the detectors this V-shaped signature, with two tracks not connected to any other track or vertex, and of opposite curvatures in the magnetic field permeating the detectors due to their opposite charge. The decay $K_S^0 \to \pi^+ + \pi^-$, has a similar signature. Those decays are called V0 decays.

A dedicated reconstruction step has for objective their identification among all the pairs of tracks with opposite charges collected during tracking. It takes advantage of a few geometric variables that emerge when the two tracks are propagated to their point of closest approach (PCA) that is used as an estimate of the decay point.

The propagation to the PCA is done by minimising the squared distance χ^2, defined in Eq. 3.1 as the average of the squares of the distances Δ_{neg} and Δ_{pos}, between the negative daughter
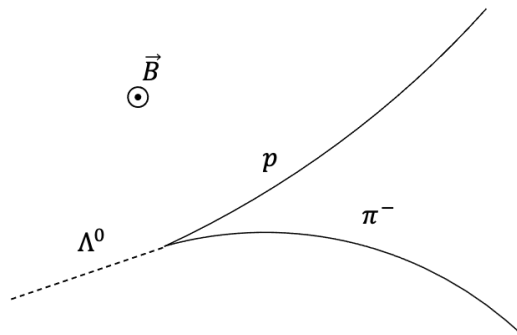
Figure 3.1: Topology of the V0 decay $\Lambda \to p + \pi^-$ inside a magnetic field $\vec{B}$ — neutral particle track in dotted line, charged particle tracks in full lines with curvatures because of the magnetic field.

track candidate position and the PCA candidate and between the positive daughter track candidate position and the PCA candidate, where the PCA candidate $(x_{PCA}, y_{PCA}, z_{PCA})$ is the midpoint of the line segment defined by the track points $(x_{neg}, y_{neg}, z_{neg})$ and $(x_{pos}, y_{pos}, z_{pos})$ [Shahoyan (2022a)].

$$\chi^2 = \frac{1}{2} \cdot (\Delta_{neg}^2 + \Delta_{pos}^2) \tag{3.1}$$

where

$$\Delta_{neg}^2 = (x_{neg} - x_{PCA})^2 + (y_{neg} - y_{PCA})^2 + (z_{neg} - z_{PCA})^2 \tag{3.2}$$

and likewise for Δ_{pos}^2.

In short, the PCA is found by minimising χ^2 in regard to x_{neg} and x_{pos}. χ^2 can be seen as a function of only those two parameters as y and z are functions of x if we consider a track of known trajectory. The algorithm used for the minimisation is Newton's method. Geometric considerations in the transverse plane of the detector give a first estimate of the PCA position. Three cases summarise all possible configurations, pictured in Fig. 3.2: the circles drawn by the two V0 daughter track candidates and their extension can either cross in two points or never, in which case either the smaller circle is contained inside the bigger circle or is located outside it. If the circles intersect, the PCA should be located in close proximity of one of the two crossings points. If the circles don't intersect, it should be located in close proximity of the centre point between the two circles' surfaces. Those points are used as seeds for the minimisation of χ^2. In the crossing circles case, if two PCA are found, the one with the smallest χ^2 value is kept. If the minimisation fails, the V0 candidate is discarded.

Once the secondary vertex position has been estimated by propagating the two daughter track candidates to the PCA, four main variables can be defined on which cuts have a powerful discrimination power. They are depicted in Fig. 3.3 (not to scale, exaggerated for readability) and detailed below:

- The distance of closest approach (DCA) between two tracks should be very small if the two tracks indeed originate from a same particle decay, although due to finite detector res-
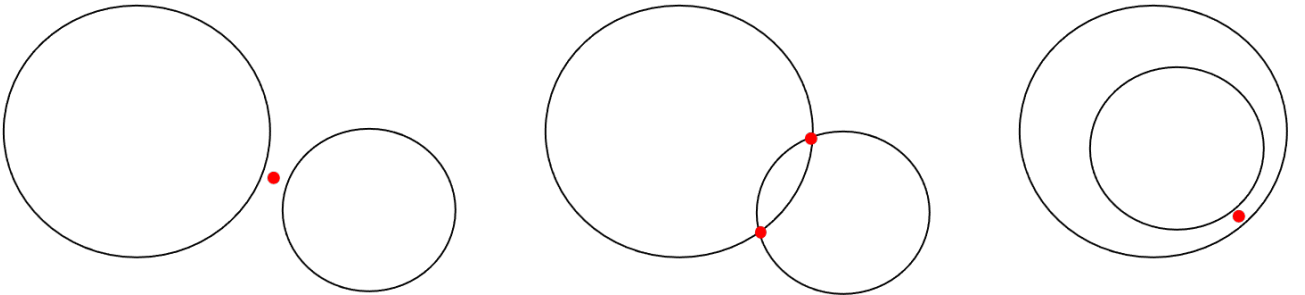
Figure 3.2: All three possible configurations of the track trajectories in the transverse plane. The red points are the PCA seeds used for the minimisation in each configuration.
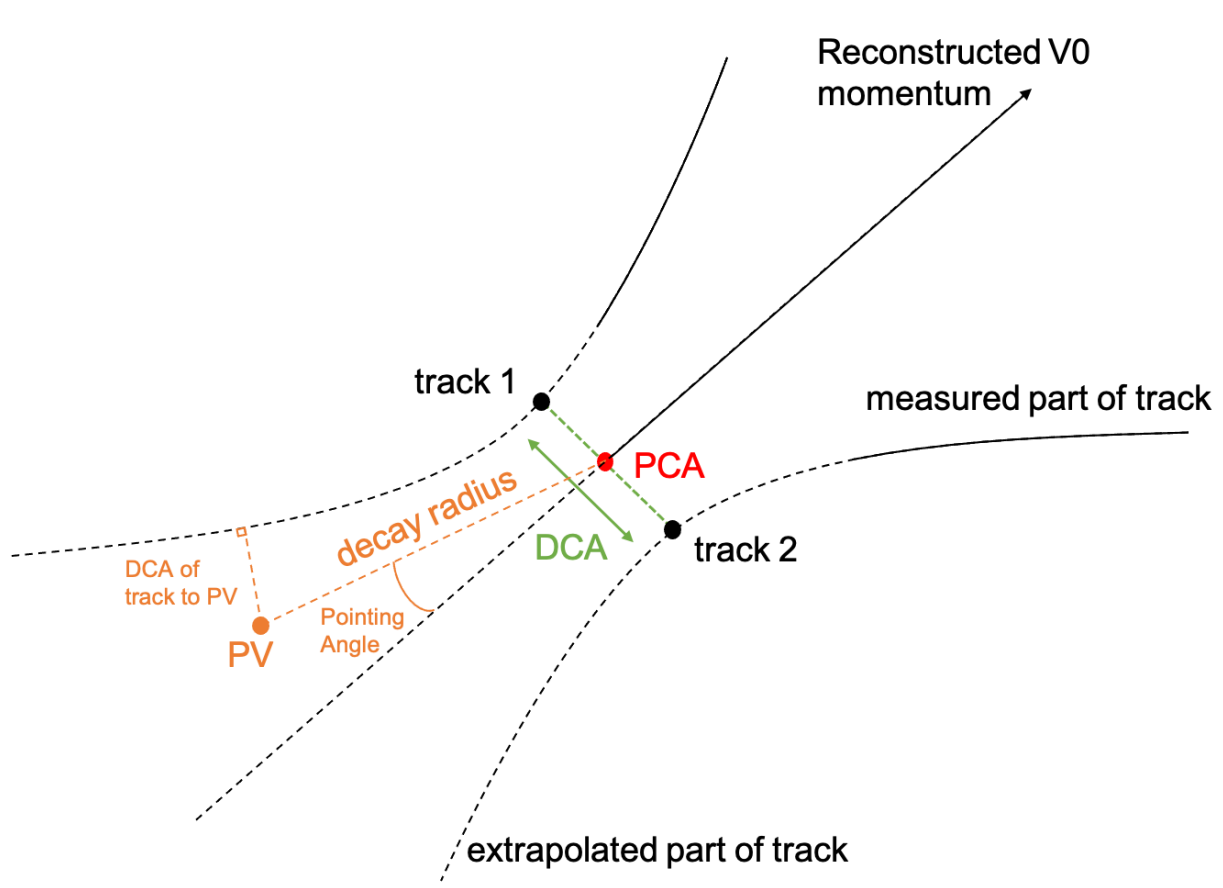
Figure 3.3: Sketch of the topology of a V0 decay inside a magnetic field.

olution it cannot be infinitely small and thus a tolerance has to be accepted. A quadratic mean of Euclidean distances has been calculated in the propagation of the two tracks to their PCA: χ^2 defined in Eq. 3.1. This quantity is what this analysis uses as definition for the DCA between the V0 daughter candidates.

- The distance of closest approach of a track to the primary vertex (PV) tends to be much larger for secondary particles originating from a light-flavour particle decay far away from the collision compared to that of primary particles produced in the collision. The distance used for the DCA of a V0 daughter candidate the PV is a standard Euclidean distance.

- The decay radius, defined as the distance the V0 particle travels before decaying, can theoretically be very small: it follows an exponential law as seen in Section 1.6.2. However the distribution of decay radii calculated for a background of primary particle pairs should decrease a lot more rapidly at larger radii compared to true V0 daughter pairs. Thus applying a cut on this variable helps reduce the false positive count.

- The pointing angle between the momentum of the V0 and the relative position of the PCA to the PV should in principle be very small in the case of a primary V0, as that V0 is not affected by the magnetic field and should thus have travelled in a straight line from the collision that gave birth to it. In practice, a cut is imposed on the cosine of this pointing angle, as the cosine is calculated directly from the inner product of those two vectors.

These variables are used among other considerations for the finding of V0 decays during the reconstruction. The reconstruction of those secondary decays uses brute force. For each data frame, the algorithm loops over all the tracks with positive charge, and for each of those tracks, it then loops over all the tracks with negative charge that share an associated collision in common with that positive track. The pair is then subjected to the PCA finding summarised above in this same section. If a PCA is found, the distance between that point and the collision vertex, i.e. the decay radius of the hypothetical primary V0 particle, is required to be greater than a chosen cut value. Then a causality check is made: if one of the two tracks is associated with a detector hit at a transverse radius smaller than that of the PCA candidate, within a set tolerance range, the pair of tracks is discarded. Additional cuts are set as follows: a minimum p_{T}, a minimum DCA to the PV of each track, a maximum DCA to the PV for the V0, a minimum cosine of pointing angle for the V0, a maximum on the tangent $\tan(\lambda_{V0})$ of the angle λ_{V0} between the momentum of the V0 and its transverse part that translates the imposition of an upper limit on the rapidity of the V0. The effect of those cuts on the invariant mass plots for the three hypotheses (K0S, Lambda and AntiLambda) are shown in Fig. 3.4: the background count is greatly reduced compared to the signal count when the secondary vertex cuts are applied. Because the data written on the AO2D has those cuts applied, a small simulation of 7500 events has been produced with the cuts from Table 3.1 completely relaxed

for the comparison, using apart from those cuts the same parameters as the MC production analysed in this thesis and presented in Section 3.2.1. A last check is done on the reconstructed invariant masses of the V0 candidate and its daughters, that should fall close to the masses published in the Particle Data Group review [Tanabashi et al. (2018)] within a p_{T} dependent margin [Shahoyan (2022b)].

The values of those cuts at the time of the reconstruction of the data used in this analysis are detailed in Table 3.1.

The V0 candidates that pass those cuts during the reconstruction are saved into the AO2D data file, in the form of a set of 3 identifiers. One to the collision the V0 was found in, and two to the positive track and to the negative track that form the V0 candidate. If the two tracks shared more than one collision then the primary vertex that gives the smallest pointing angle is kept [Shahoyan (2022b)]. This pool of V0 candidates will be refined with an offline analysis presented in the next section.

3.2 Strangeness spectra extraction with a Monte Carlo simulation of the pilot beam run

At the end of October 2021, the first stable beams of Run 3 were run at the LHC. Those runs, of short durations, were designed to test the readiness of the detectors for the full launch of the Run 3 data-taking campaign at the end of 2022. A little more than 8 million proton-proton collisions at low interaction rate were recorded by the ALICE detector during this pilot beam run, within a magnetic field of $0.2\,\mathrm{T}$, a little lower than the nominal value of $0.5\,\mathrm{T}$ that has been used in Run 2 and that will be used in Run 3, and at a low total collision energy $\sqrt{s} = 0.9\,\mathrm{GeV}$.

The data collected by ALICE during those runs has already been used to test the data analysis software that has been designed for Run 3 with O2. So called asynchronous passes

V0 selection variable	Cut value
DCA of daughter track to PV	$> 0.1\,\mathrm{cm}$
V0 transverse decay radius	$> 0.5\,\mathrm{cm}$
DCA of V0 to PV	$< 0.2\,\mathrm{cm}$
V0 cosine of pointing angle	> 0.9
p_{T} of V0	$> 0.01\,\mathrm{GeV/c}$
$\tan(\lambda_{V0})$	< 2

Table 3.1: Selections applied during the secondary vertex reconstruction.
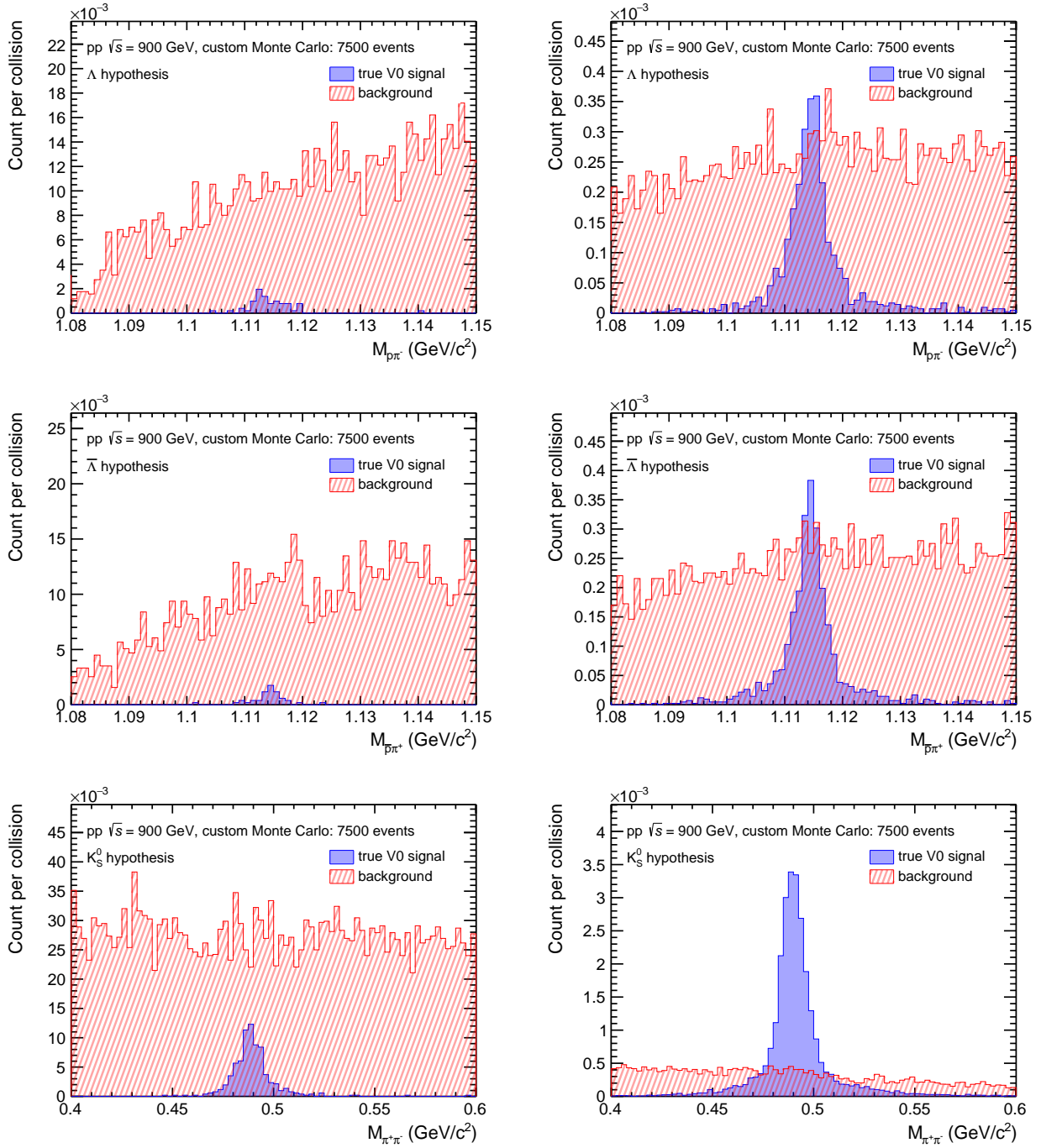
Figure 3.4: Invariant mass distributions for the Λ (top), $\overline{\Lambda}$ (center) and K_S^0 (bottom) hypotheses, with the secondary vertex cuts completely relaxed (left) and with the secondary vertex cuts as defined in Table 3.1 (right), for the V0 candidates associated with a true V0 Monte Carlo particle in blue and for the V0 candidates not associated with such a V0 Monte Carlo particle in hashed red

were released, numbering four, corresponding to iterations of the whole reconstruction process, and for each of which a collection of AO2D files was released. The V0 analysis software, the basis of the strangeness reconstruction chain, has thus been put to the test in the first two asynchronous passes and some issues were found and solved. Unfortunately, the third pass witnessed a problem in the reconstruction software when writing to the AO2D files, that made the analysis of V0 decays impossible. A fix was found, but the new asynchronous pass 4 arrived too late to be thoroughly analysed for this thesis.

Instead, the data from a first medium-scale Monte Carlo simulation of the pilot beam is analysed. The MC simulated data is processed the same way real data from the detector would be. That way the new V0 analysis process ported to the O2 environment can be tested and its performance evaluated. The analysis tools used are detailed in Appendix B.

In this analysis the p_{T} and rapidity production spectra of K_S^0, Λ and $\overline{\Lambda}$ are estimated for a Monte Carlo production that simulates the pilot beam conditions, and compared to the true spectra obtained from reading the MC truth as well as to the spectra from the Run 1 analysis on pp collisions at the same total beam energy $\sqrt{s} = 0.9\,\mathrm{TeV}$ as the 2021 pilot beam [Aamodt et al. (2011)].

3.2.1 Dataset and Monte Carlo

This V0 analysis has been done on the MC production named LHC22c5. This production gathers pp collisions simulated at $\sqrt{s} = 0.9\,\mathrm{TeV}$ with a low interaction rate of 2kHz, a rate low enough for pile-up effects to be neglected. Three runs of this production (with reference IDs 505548, 505582, 505600) show unexplained poor invariant mass distribution shapes, very different from what has been observed so far in previous smaller test MC simulations and in the other 7 runs of the same production. The difference in shape of those invariant mass plots (after the analysis cuts that will be presented in Section 3.2.3) can be seen in Fig. 3.5, where they have been drawn with a normalisation to their respective maximum to make the comparison of the shape easier. The runs 505548, 505582 and 505600 show a noticeably larger peak, with an unexpected structure on the sides of the peak. Those runs are thus not used in this analysis. About 400 000 collisions remain at the start of this analysis.

The generation of particles in the collisions and their decays is simulated by PYTHIA8 [Bierlich et al. (2022)], while the transport of those particles and their interaction with matter is simulated by GEANT4 [Agostinelli et al. (2003)]. A custom O2 digitiser converts the energy deposits on the detectors from GEANT4 into an electronic signal that is given to the detector readout and fed to the reconstruction process that eventually generates the AO2D files.
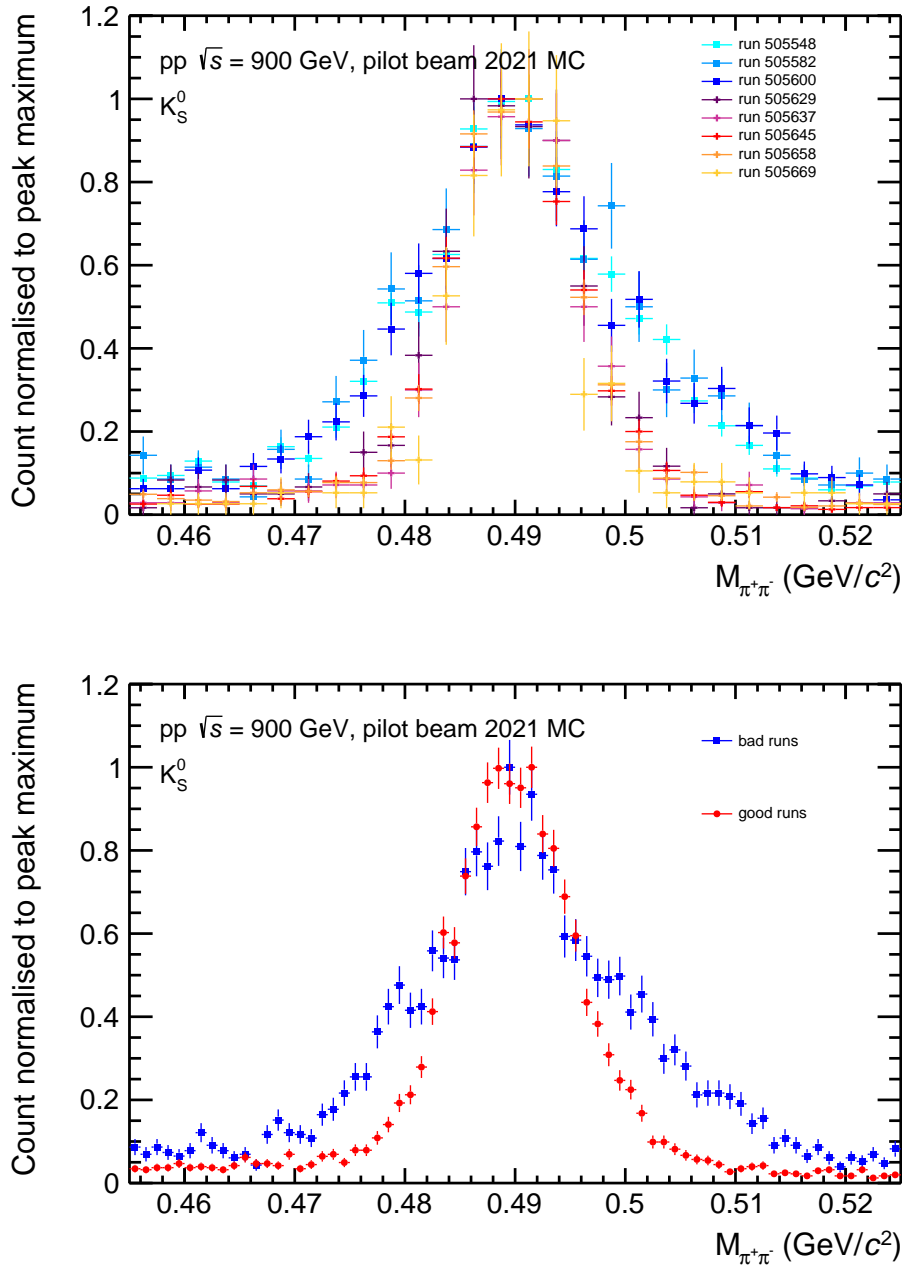
Figure 3.5: Invariant mass distributions of $\pi^- + \pi^+$ (K_S^0 hypothesis) for V0 candidates that passed the analysis selection in the three excluded runs with reference IDs 505548, 505582, 505600 (full squares), and in the other seven runs that are analysed in this thesis (full circles). The upper plot shows all the runs individually, the bottom plot combines the three bad runs (full squares, blue) and the seven good runs (full circles, red)

3.2.2   Event selection

As mentioned in 2.2.7, real data can be polluted by beam-gas events. And the default event selection for the 2021 pilot beam data, called sel8, uses the FT0 detector timing information to filter those out. However the data analysed in this thesis comes from a MC simulation. All events simulated in it are true beam-beam collisions. Thus the sel8 event selection has not been applied to it.

The reconstruction of tracks with high pseudo-rapidity and belonging to collisions that are too displaced from the centre of the detector along the z axis can suffer due to them missing the TPC or layers of the ITS. In Run 1, only collisions with their z-position respecting the condition $|z_{vertex}| < 10$ cm were kept, because due to this condition the track reconstruction efficiency was almost independent of the z-position of the collision [Aamodt et al. (2010)]. For simplicity, and to allow for an easier comparison to the Run 1 analysis, the same cut is applied in this analysis. 365 000 collisions remain after this selection that will be processed in this analysis.

For each of the collisions that pass this selection, the V0 candidates associated with the collision are retrieved and subject to a last selection.

3.2.3   V0 selection

The information available for V0 candidates at the beginning of this offline analysis is a link to the two daughter track candidates. The propagation of the two tracks to their PCA is done once more, using the same algorithm as the one presented in section 3.1. This allows for a refinement of the rough cuts applied as V0 selection in the reconstruction, but also the calculation of other variables upon which a cut will be made. The choice is made for this analysis to follow similar analysis cuts as those chosen in the Run 1 analysis of V0 decays [Aamodt et al. (2011)], that analysed similar pp collisions at $\sqrt{s} = 900$ GeV, as it allows a better comparison and gives a good idea of what can be expected.

A first selection is made on the track quality, requiring a minimum size on the transverse propagation length of the V0 daughter track candidates inside the TPC. This is done by cutting on the number of crossed TPC rows in the readout chambers' pads arrangement. This cut ensures a good p_T resolution as well as good PID capabilities with the TPC.

Some of the main selections in the Run 1 analysis have received a first cut in the V0 reconstruction step presented in the section 3.1: the cosine of the pointing angle, the transverse decay radius and the DCA between the daughters and the PV. The last two are not cut upon further than during the reconstruction, as those cuts have already been set tighter than in Run 1, in order to limit the computing resource usage needed. Only the cosine of the pointing angle actually receives a tighter cut here, from a lower bound of 0.9 to one of 0.97. This cut is kept a

little looser than in [Aamodt et al. (2011)], to improve the performance of the signal extraction detailed in the next two sections by introducing a more regular background for a more accurate modelling of it, along with simply reducing the signal loss. A new cut is done, on the DCA between the V0 daughter candidates. The cut is chosen looser than in Run 1, for the same reason as the cut on the pointing angle, and all V0 candidate with a DCA between daughters smaller than $1\,\mathrm{cm}^2$ are kept. Figure 3.6 shows the distributions of the 5 variables mentioned so far in this subsection, after the V0 reconstruction and before the cuts mentioned in this subsection. Shown separated are the V0 candidates associated with true primary V0 particles with the Monte Carlo truth and the background made out of all the other V0 candidates.

The PID capabilities of the TPC on the V0 daughter candidates are also used to filter out some additional background. This selection step checks three configurations, and does not distinguish particles from their antiparticles. Either both V0 daughter track candidates are π particles (K_S^0 candidate), or the positive daughter candidate is a p and the negative one a π (Λ candidate), or the positive daughter candidate is a π and the negative one a p ($\overline{\Lambda}$ candidate). This cut is also kept very loose in order to not discard any signal. The details of the particle identification method is as follows: the average value of the ionisation energy loss of particles measured in the TPC and recorded in Figure 2.11 follows a line that can be modelled by a Bethe-Bloch parametrisation [Tanabashi et al. (2018)] and is characteristic to the species of particle ionising the TPC gas. This parametrisation is determined for each species during calibration. Particles of the correct species will be scattered around their corresponding line, and the distribution of the residuals to that line can be fitted with a Gaussian function. A cut can thus be imposed on the distance to that average line, set to $\pm 5\sigma_{TPC}(p)$ in this analysis, where $\sigma_{TPC}(p)$ is the standard deviation of the fitted Gaussian.

Finally, particle spectra are usually presented in the literature as rapidity- and p_{T}- spectra $\frac{\mathrm{d}^2 N}{\mathrm{d}p_{\mathrm{T}}\mathrm{d}y}$. Due to the low number of data entries in this study, the differential measure of the yields in rapidity is not possible at the same time as their differential measure in transverse momentum. Thus the measure is done as an average inside a rapidity interval where the production rate stays relatively constant: the rapidity range $|y| < 0.75$ fits this condition, as can be seen in Fig. 3.7 for all the V0 particles generated in the Monte Carlo simulation.

A summary of all the cuts imposed on the V0 candidates that have been detailed above is gathered in Table 3.2. At this stage, a quality check can be made on the pool of V0 candidates that pass those selections.

Armenteros-Podolanski Plot

Plotting the Armenteros-Podolanski plot [Podolanski and Armenteros (1954)] for the V0 candidates is a visual way to check that those candidates are indeed good V0 candidates. In it, the momentum q_T of the daughters' transverse to that of the V0 is plotted against the dimension-
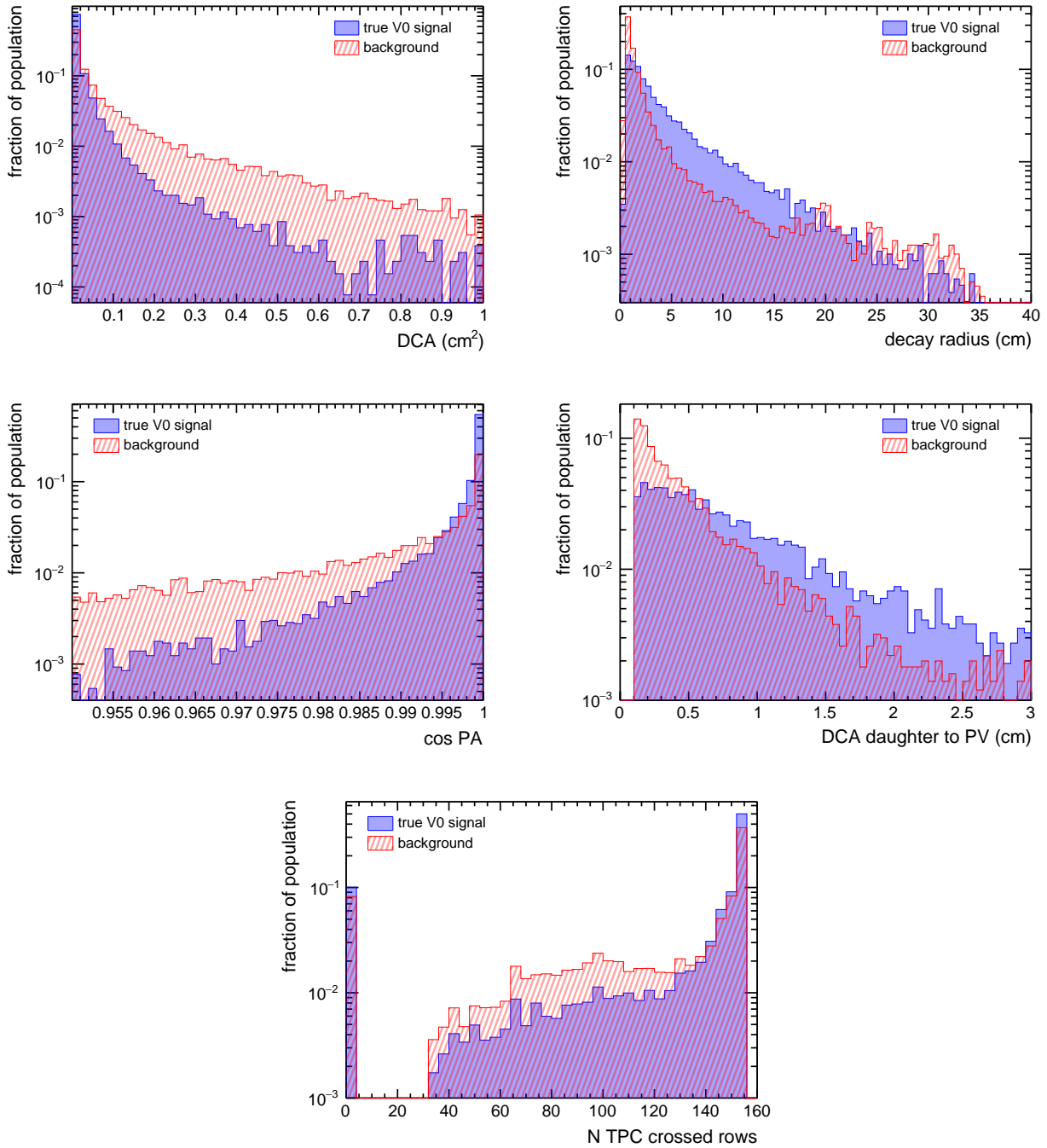
Figure 3.6: Distributions of the DCA between the V0 daughters, of the transverse decay radius of the V0, of the cosine of the pointing angle of the V0, of the DCA between the V0 daughters and the PV, and of the number of crossed rows inside the TPC of the V0 daughters, for the V0 candidates associated with a true V0 Monte Carlo particle in blue and for the V0 candidates not associated with such a V0 Monte Carlo particle in hashed red — the histograms have been normalised to their number of entries to allow for a better shape comparison.
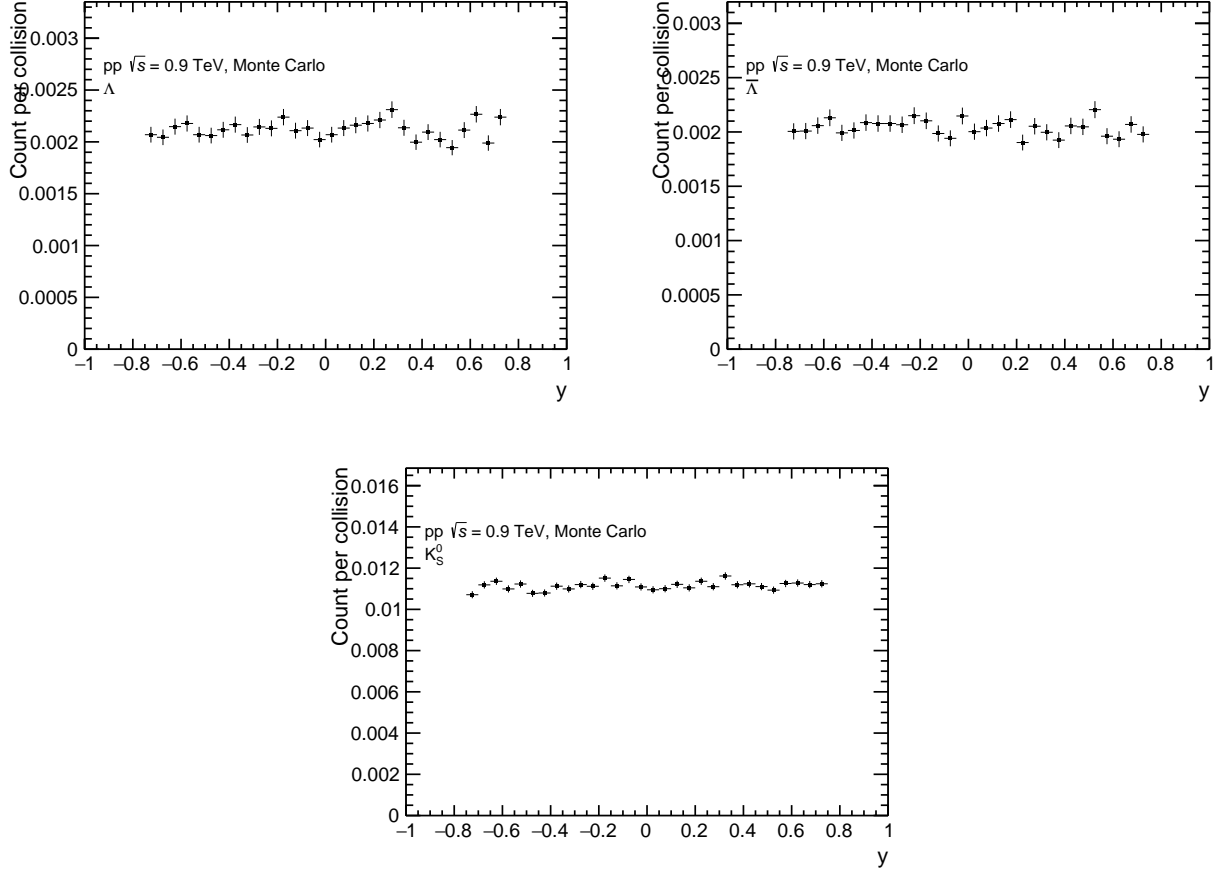
Figure 3.7: Rapidity distributions of all primary Λ (upper left), $\overline{\Lambda}$ (upper right) and K_S^0 (bottom) generated by the simulation with rapidities $|y| < 0.75$ — normalised to the number of collisions in the simulation with $|z_{vertex}| < 10$ cm.

Topological V0 Selection	K_S^0 (Λ and $\overline{\Lambda}$) Cut
V0 transverse decay radius	$> 0.5\,\text{cm}$
DCA daughter track to PV	$> 0.1\,\text{cm}$
V0 cosine of pointing angle	> 0.97
(DCA V0 daughters)^2	$< 1\,\text{cm}^2$
General Selection	K_S^0 (Λ and $\overline{\Lambda}$) Cut
Rapidity interval of V0	$|y| < 0.75$
TPC dE/dx Selection of daughters (for Λ and $\overline{\Lambda}$)	$< 5\sigma$
TPC Number of Clusters Found of daughters	> 70

Table 3.2: Selections applied to K_S^0, Λ and $\overline{\Lambda}$ candidates.

less variable α, that measures the normalized difference of the daughters longitudinal momenta $p_{||}$ (see Fig. 3.8 and Eq. 3.3), with q_T and each $p_{||}$ in the lab frame (variables chosen as in [Rodríguez et al. (2021)]. This plot translates in a visual way the 4-momentum conservation in the decay through the distribution of detected V0s around ellipses for each V0 type. It also outlines the asymmetry in the momenta of the daughter particles of a V0 particle due to daughters having different masses, as the ellipses corresponding to such V0 particles would not be symmetric with respect to $\alpha = 0$. And indeed can clearly be seen in Fig. 3.9 three ellipses, one symmetric with respect to $\alpha = 0$ that corresponds to K0s, and two smaller ellipses, shifted away from $\alpha = 0$ and symmetric with respect to each other, corresponding to Λ (right ellipse) and $\overline{\Lambda}$ (left ellipse).

$$\alpha = \frac{p_{||}^+ - p_{||}^-}{p_{||}^+ + p_{||}^-} \tag{3.3}$$

The V0 candidates that pass all the selections detailed in the previous subsection are tested further by looking at their invariant masses under the assumption that the V0 candidate daughters belong to the right species.

3.2.4 Invariant mass distributions

As explained in section 1.6, the invariant mass M_0 of the mother particle in a particle decay can be calculated from the measured invariant masses of the daughters, their momenta and energies using Eq. 1.8. The analysis conducted so far gathers pairs of V0 daughter candidates. Despite all the selections and cuts so far, some background remains. The calculation of the invariant mass of each of the V0 candidates corresponding to those pairs of tracks can help distinguish real V0s from the background: the former should form a peak around the invariant mass of the V0 particles K_S^0, Λ and $\overline{\Lambda}$.

To proceed with this calculation, an assumption has to be made about the nature of the two daughters, in order to input their invariant masses in the equation. For K_S^0 candidates, the daughter with negative charge is assumed to be a π^- while the daughter with positive charge is assumed to be a π^+. For Λ ($\overline{\Lambda}$) candidates, the negative daughter is assumed to be a π^- ($\overline{p}$) while the positive daughter is assumed to be a p (π^+).
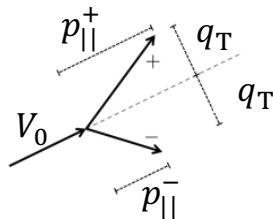
Figure 3.8: Sketch of the momentum projections used in the Armenteros-Podolanski plot.
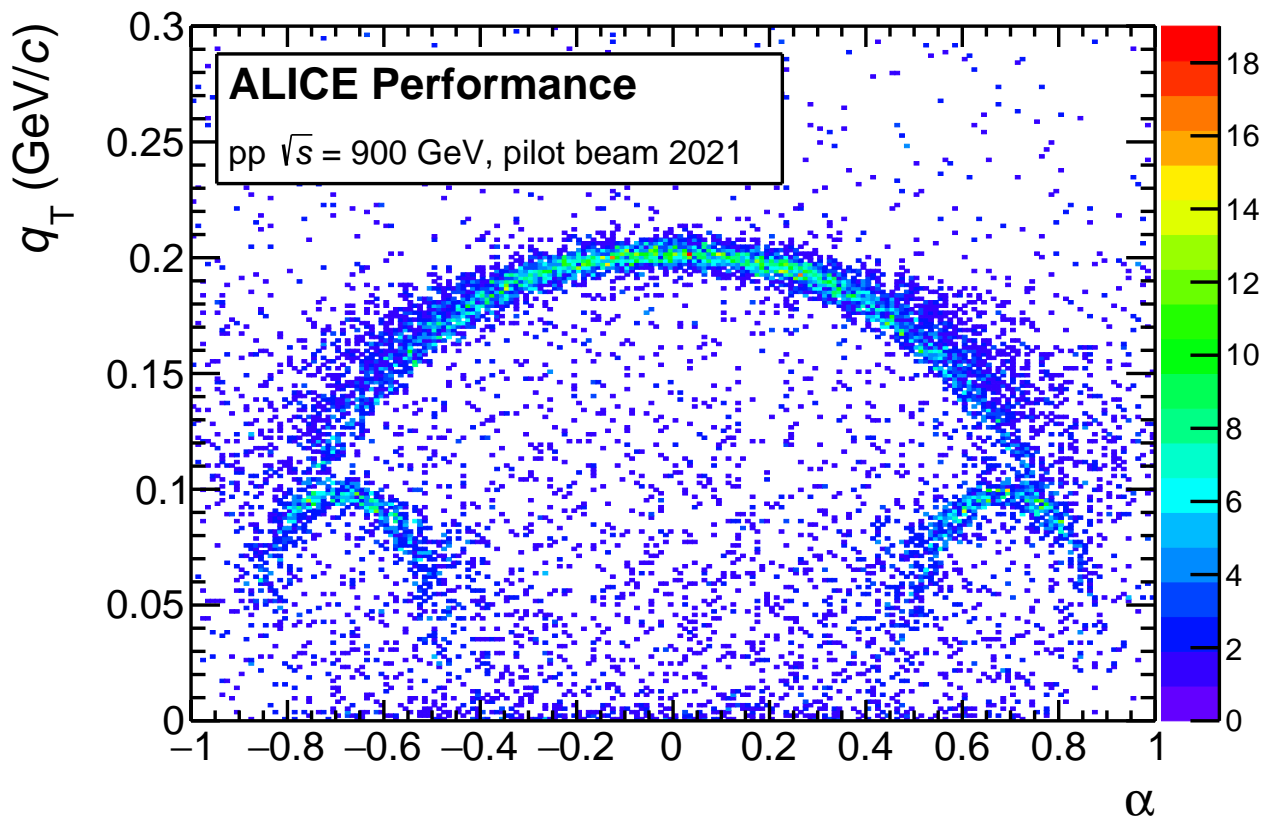
Figure 3.9: Armenteros-Podolanski plot for the V0 candidates that passed the selection detailed in section 3.2.3.

The invariant mass calculated for each configuration is saved during the analysis workflow in the form of three two-dimensional histograms along with the reconstructed p_T of the V0 candidates, one for each of the three V0 particle types studied in this thesis. The binning of said histograms are chosen fine enough so that no feature is lost while keeping a moderate disk size.

Figure 3.10 shows the invariant mass histograms obtained for the K_S^0 daughter pair candidates and for the Λ daughter pairs candidates. A peak is clearly visible in each distribution. Its width comes mainly from the detector and reconstruction resolutions for the transverse momentum p_T and the energy involved in the calculation of the invariant mass. One thing to note: K_S^0 shows a peak shifted away from the mass published in the Particle Data Group [Tanabashi et al. (2018)]. This stems from an issue with the application of the material budget energy loss when propagating the tracks to their PCA for this MC production, but has been fixed in more recent simulations, and does not impact the analysis as the peak is still very well defined.

Using those invariant mass plots, the number of actual V0 among the candidates can be inferred.

3.2.5   Signal extraction

The estimation of the signal yield for each V0 species necessary for the derivation of this species' spectrum relies on the relatively regular background shapes for the invariant mass distributions around the peak.

The background is modelled in this thesis by a linear function. The peak is modelled with a Gaussian function in order to obtain an average position (mean μ of the Gaussian) and width (standard deviation σ of the Gaussian). The invariant mass histograms of each V0 species are fitted with the sum of a linear function and a Gaussian function. Figures 3.11 show the fit function drawn in red on top of the invariant mass distribution represented by black markers for the whole of each V0 collection (with transverse momenta p_T contained within the interval $[0.0, 3.0]$ GeV/c), along with the mean μ and width σ of each peak obtained with the fit.

The details of the procedure are as follows. The invariant mass histogram divides the interval $[0.4, 0.6]$ GeV/c^2 in 40 mass bins, each with a width of $5\,\mathrm{MeV/c^2}$ for K_S^0, and divides the interval $[1.015, 1.215]$ GeV/c^2 in 100 mass bins, each with a width of $2\,\mathrm{MeV/c^2}$ for Λ and $\overline{\Lambda}$. Those bin sizes have been found sufficiently large to give a good fit quality while small enough to keep the resolution good enough in regard to the signal peaks. A first fit is done with a simple Gaussian function, to get a rough estimate of the mean and width σ of the peak. The mean and width of the peak are used to define a signal region and two background side bands: the former as $]\mu - L\sigma; \mu + L\sigma[$, the latter as $]\mu - 2L\sigma; \mu - L\sigma[\cup]\mu + L\sigma; \mu + 2L\sigma[$ with $L = 4$. They are delimited in Fig. 3.11 by vertical grey lines. Then, the distribution in the background
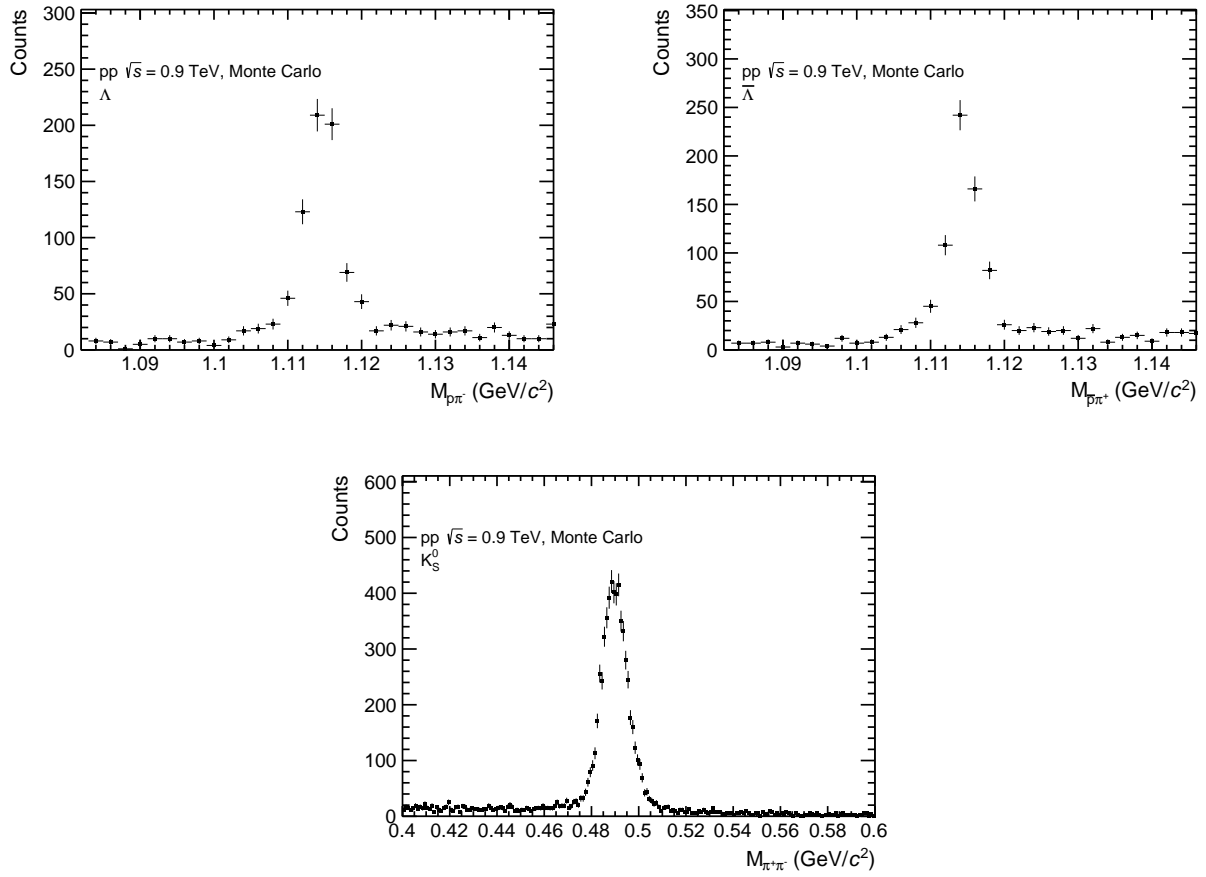
Figure 3.10: Invariant mass histograms of $\pi^- + p$ (upper left), $\overline{\pi^+}$ (upper right) and $\pi^- + \pi^+$ (bottom), respectively for the Λ, $\overline{\Lambda}$ and K_S^0 candidates that have passed the selections detailed so far.

side band regions is fitted to a linear function. Finally, the sum f_{Fit} of a Gaussian function and a linear function (Eq. 3.4) is fitted to the distribution in the union of the signal region and the side band regions, using the parameters from the initial two fits as seeds.

$$f_{Fit}(m) = A \cdot \exp\left\{ \left(\frac{m - \mu}{\sigma} \right)^2 \right\} + c \cdot m + d \qquad (3.4)$$

where the amplitude A, the mean μ and the standard deviation σ of the Gaussian, along with the slope c and the intercept d of the linear function b are fit parameters, and m is the invariant mass variable.

The counting of the number of V0s, or signal, in the invariant mass plot is done by counting the number of candidates N_{total} in the signal region $]\mu - L\sigma; \mu + L\sigma[$ then subtracting from it the integral of the fitted background line[1] $b(m) = cm + d$ inside that same signal region to obtain N_{signal} as summarised in Eq. 3.5. That way no assumption is made as to the shape of the signal distribution, often not actually Gaussian in shape. This signal extraction is illustrated in Fig. 3.11 by the integral of the background line fit being filled with green. The interval is chosen as a trade-off between the ratio of true signal that falls inside it (wanted as close to 1 as possible, in this case ~0.99 with no p_T dependence for the chosen interval) and the symmetric background side bands staying in a region where the linear model holds. Λ and $\overline{\Lambda}$ also have a hard lower limit for the leftmost boundary given how close the peak is to the lowest possible invariant mass value of ~1.08 GeV/c^2 corresponding to the sum of the masses of π^- and p.

$$N_{signal} = N_{total} - \frac{1}{\Delta m} \int_{\mu - 4\sigma}^{\mu + 4\sigma} b(m)\, dm \qquad (3.5)$$

where Δm is the width of the invariant mass bins and where the factor $\frac{1}{\Delta m}$ converts the integral back to a count.

This analysis looks to estimate the p_T spectra of K_S^0, Λ and $\overline{\Lambda}$. For that, the data is divided into several p_T bins and the signal extraction procedure detailed above is applied to each data subsample. Those bins ideally should be made as small as possible to get as fine a distribution for the p_T spectra as possible, but the limited size of the data sample commands widths large enough to keep uncertainties small. In addition to those two balancing imperatives, the ease of comparison with the Run 1 published analysis [Aamodt et al. (2011)] looking at the same decays has been taken into consideration. The chosen divisions of the p_T axis for each particle species are as follows:

- K_S^0 p_T binning : `[0.0, 0.2, 0.3, 0.4, 0.5, 0.6, 0.7, 0.8, 0.9, 1.0, 1.1, 1.2, 1.3, 1.4, 1.6, 2.0, 2.4, 3.0]` GeV/c.

---

[1] due to low number of data entries, sometimes the fitted background line goes below 0 inside the signal region. In such an event, only the positive part of the fit function is integrated.
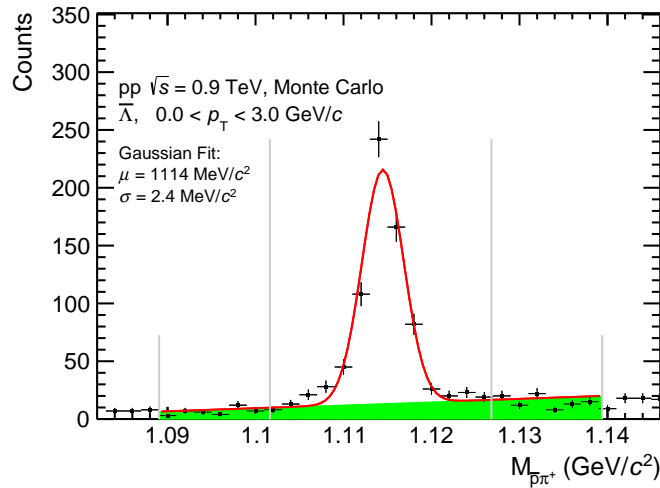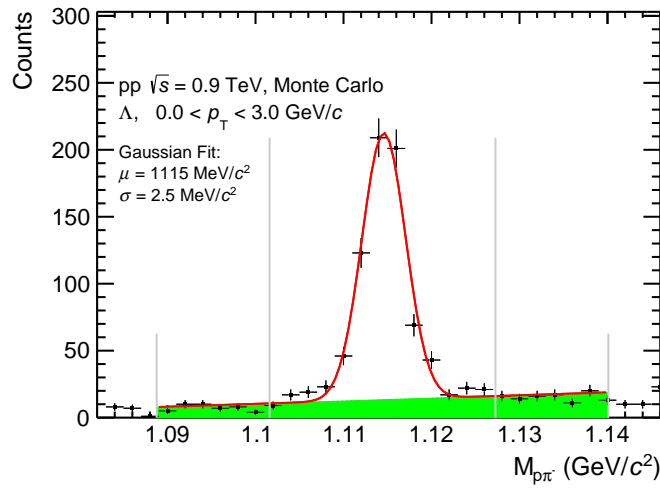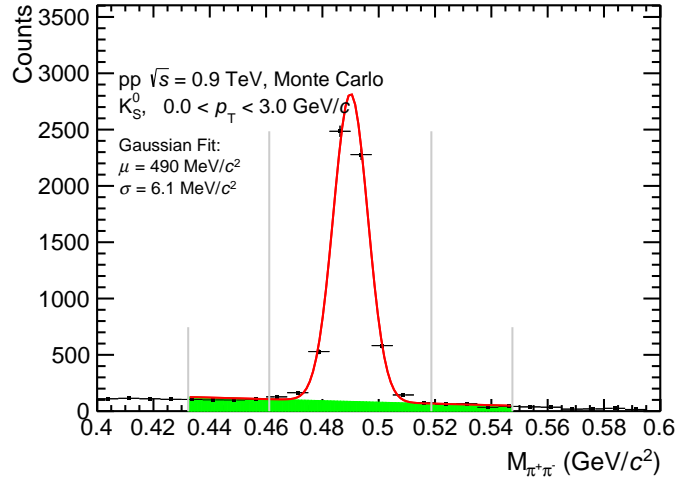
Figure 3.11: Illustration of signal extraction for K_S^0 (top), Λ (centre) and $\overline{\Lambda}$ (bottom) - Invariant mass distribution plotted with black markers, global fit function drawn in red, linear portion of the global fit function drawn in green - four grey vertical lines mark from left to right the -8, -4, +4 and +8 σ ranges around the mass peak.

- Λ and $\overline{\Lambda}$ p_T binning : [0.6, 0.8, 1.0, 1.2, 1.4, 1.6, 2.0, 2.4, 3.0] GeV/c. The range studied starts at $0.6\,\mathrm{GeV/c}$ instead of $0.0\,\mathrm{GeV/c}$ because the number of data entries between those two values are too few.

The resulting fits for each of those bins can be found in Appendix A.

The raw rapidity- and p_T spectrum is thus calculated as per Eq. 3.6:

$$\frac{\mathrm{d}^2 N_{raw}}{\mathrm{d}p_\mathrm{T}\mathrm{d}y} = \frac{1}{\Delta p_\mathrm{T}} \cdot \frac{1}{\Delta y} \cdot N_{signal} \tag{3.6}$$

where N_{signal} is calculated as shown in Eq. 3.5, Δp_T is the width of the p_T bin for which N_{signal} is being calculated and that gives the p_T-differential quality to the spectrum, and where Δy is the rapidity range considered for the analysis ($\Delta y = 1.5$ here) that averages the spectrum over the rapidity interval $|y| < 0.75$.

The measurement of the transverse momentum p_T of the particles detected is not perfect, and in some measurements can be very far from the real transverse momentum of the particle. This effect creates a migration between the p_T bins. It can be visualised using Monte Carlo data by looking at the distribution of the deviation of the measured $p_\mathrm{T}^{measured}$ of reconstructed MC particles as a function of their true p_T^{MC}. When turned into a 2-dimensional histogram, this distribution is the detector response matrix for the p_T variable. It is shown for our analysis for each V0 species, selected using the Monte Carlo truth, in Fig. 3.12. The matrices are here almost diagonal, thus the migration between bins is small. Furthermore, the unfolding of this bin migration was not performed on the Run 1 analysis [Aamodt et al. (2011)] that this thesis will be compared to, as the bin migration had then been measured as small as well, due to the p_T bin widths used in the analysis being quite larger than the p_T resolution of ALICE.

The spectrum $\frac{\mathrm{d}^2 N_{raw}}{\mathrm{d}p_\mathrm{T}\mathrm{d}y}$ obtained is only a reflection of the particles actually detected in the detector.

3.2.6 Efficiency correction

A good number of the strange particles generated in collisions are missed, be it because their daughters have not left any trace in the detectors, because the traces they left were not reconstructed correctly, because the reconstructed daughters have not been matched successfully or because the V0 has been discarded due to cuts. On top of that, the V0 decay is only one of the many decay channels of those strange particles, and account for only about 69.2% of K_S^0 decays and 63.9% of Λ and $\overline{\Lambda}$ decays [Tanabashi et al. (2018)]. To calculate how many strange particles have actually been produced in the selected collisions based on the number of strange particles detected, a correction factor, the efficiency, has to be applied. Because the quantity of interest is the p_T spectrum of those particles, this correction has to be applied as a function of p_T.
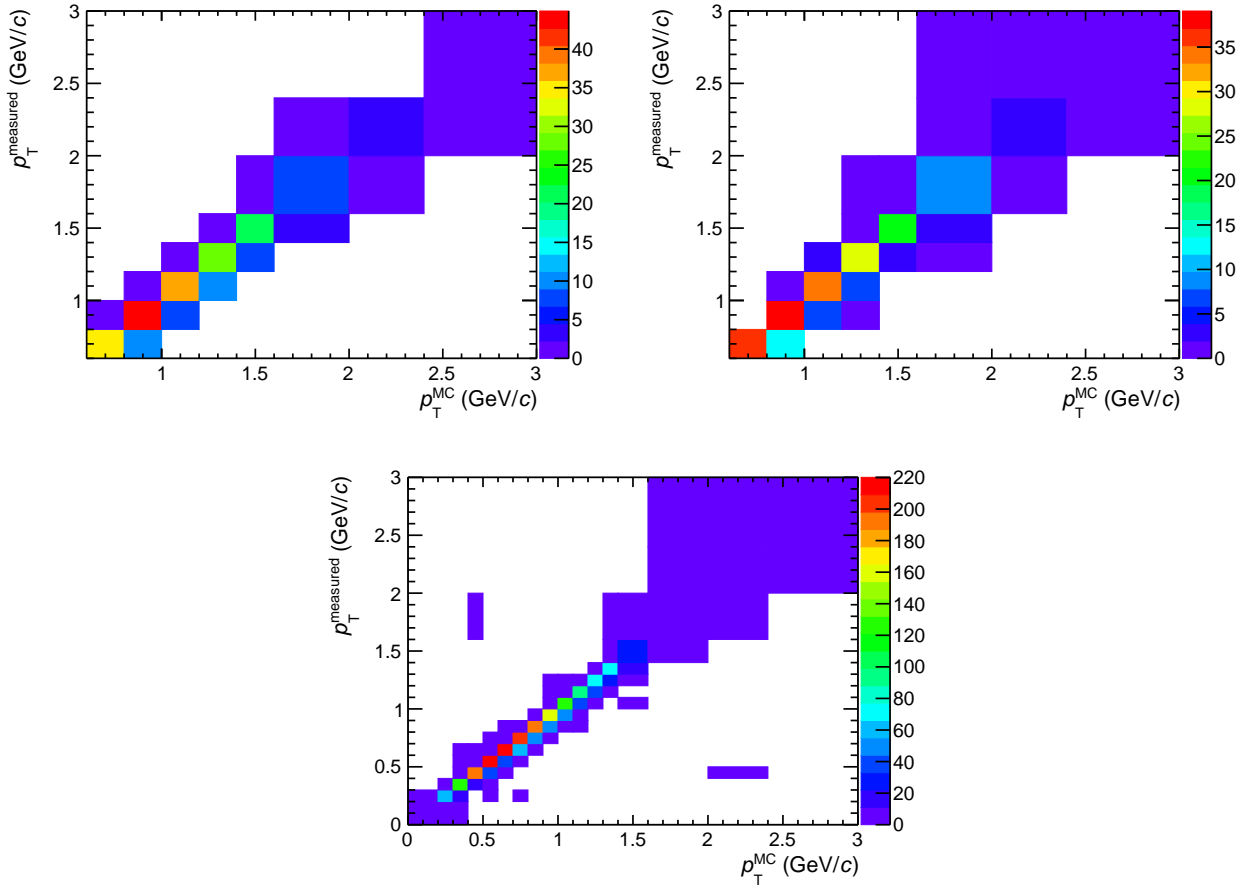
Figure 3.12: p_{T} response matrices for Λ (upper left), $\overline{\Lambda}$ (upper right) and K_S^0 (bottom).

To calculate this correction factor when analysing real data, a Monte Carlo simulation that reproduces the real data as close as possible is used. The detector and the interactions of particles with it (be it with the active parts of the detectors or with the electronics or material support) should be fined tuned to what is observed during calibration (using for example well known sources of particles like cosmic rays). Discrepancies between the real detector, the real collisions and the simulation of those should be taken into account in the uncertainties calculated for the final quantities of interests. In this thesis, the Monte Carlo truth is a perfect simulation of the data that is analysed as they are one and the same.

The same data analysis and signal extraction as presented before in this chapter is applied to the Monte Carlo dataset, with three exceptions: the species of the Monte Carlo particles associated to the reconstructed V0 daughters and to their mother must correspond to the V0 decay being studied ($K_S^0 \rightarrow \pi^+ + \pi^-$, $\Lambda \rightarrow p + \pi^-$ and $\overline{\Lambda} \rightarrow \overline{p} + \pi^+$), the MC mother is required to be a primary particle, and its rapidity y is required to fall within the interval [-0.75, 0.75]. For each of those three decays, the particles that pass the reconstruction and those three conditions are counted as N_{reco}. The efficiency ϵ is defined in Eq. 3.7 as a ratio. The numerator is N_{reco}. The denominator N_{gen} is the initial number of primary particles generated by the simulation of the particle species studied (K_S^0, Λ or $\overline{\Lambda}$). This efficiency is calculated for intervals of transverse momentum p_T^{MC} of the MC mothers.

$$\epsilon(p_T^{MC}) = \frac{N_{reco}(p_T^{MC})}{N_{gen}(p_T^{MC})} \tag{3.7}$$

Figures 3.13, 3.14 and 3.15 show the efficiencies obtained with this analysis. The three efficiencies show a lot of fluctuations. A fit of the curves with a generalised logistic function was studied to smoothen the efficiencies but the idea was discarded as it worsened the shape of the corrected spectrum when compared to the generated one, making the former less compatible with the latter.

In an analysis of real data like the one carried out in Run 1, the distributions of the variables that are cut on to select V0 candidates (see Tables 3.1 and 3.2) in data are compared to their MC counterparts. It is important that the two match as closely as possible lest an important efficiency bias is introduced. Because this thesis looks at MC data, this is not done.

The condition on the MC mother being a primary particle is important as the final objective is to measure the abundance of particles produced in the collision itself. This information however is not accessible when analysing real data.

3.2.7 Feeddown correction

To account for the reconstructed particles coming from a secondary vertex, another correction has to be applied. This correction is necessary for Λ and $\overline{\Lambda}$, as about 12% of their abundance
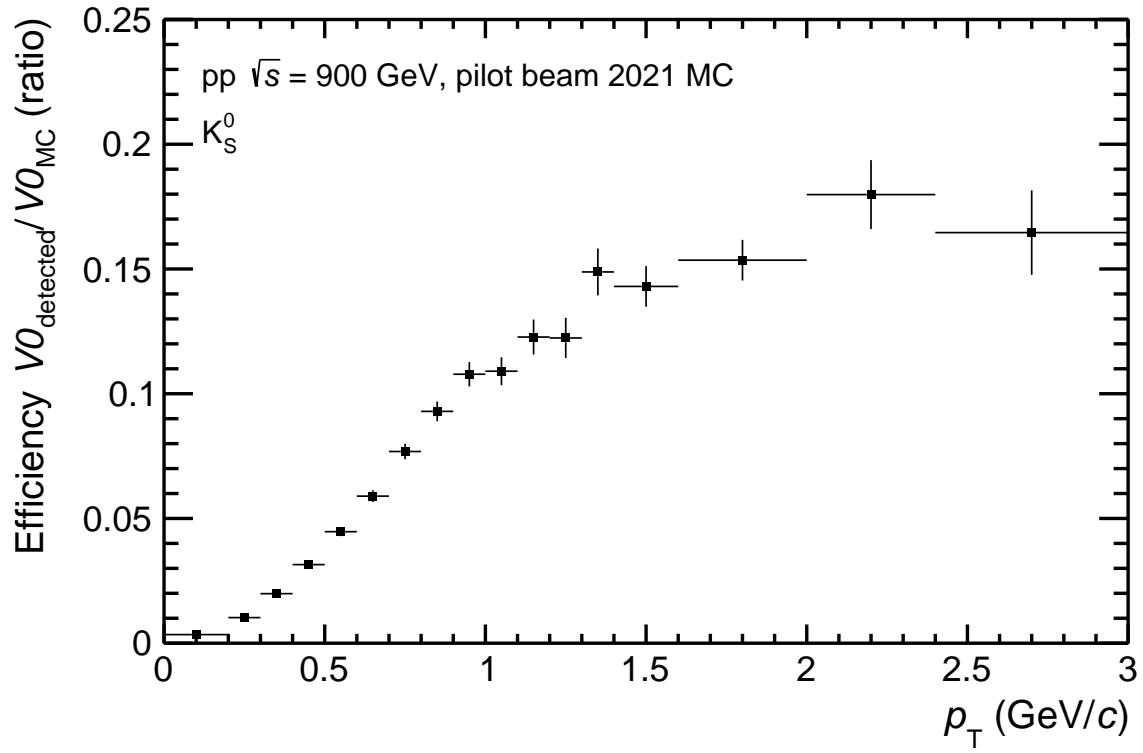
Figure 3.13: Reconstruction efficiency — K_S^0.
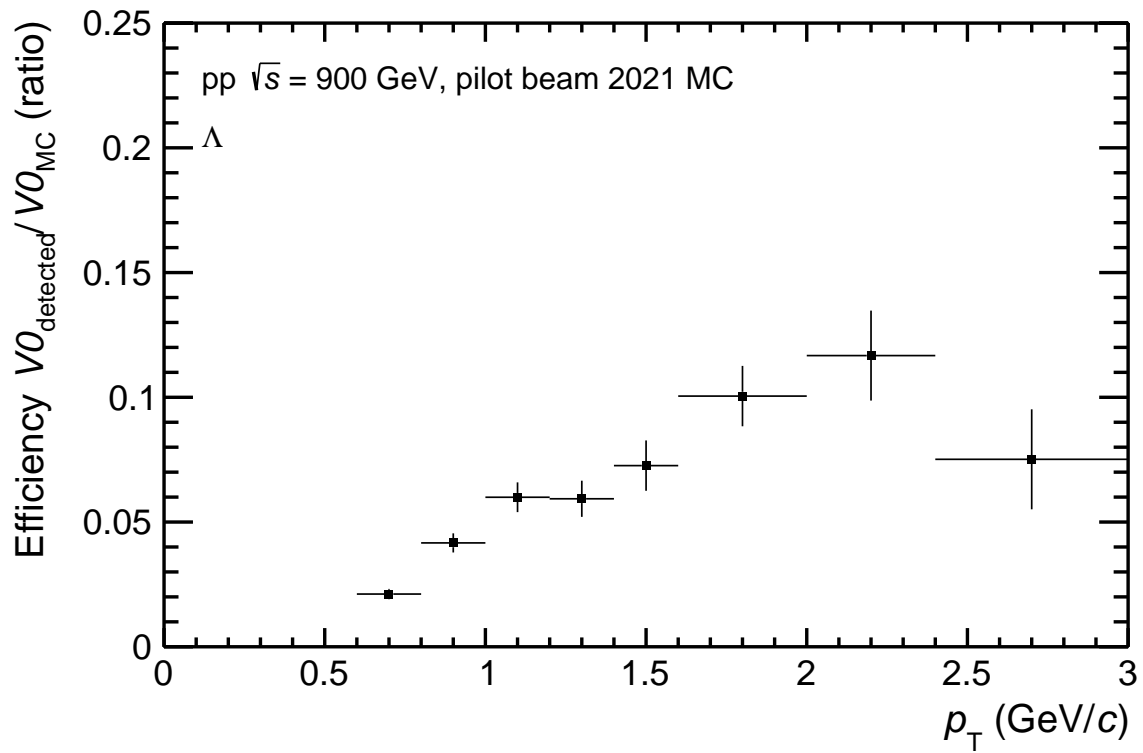
Figure 3.14: Reconstruction efficiency — Λ.
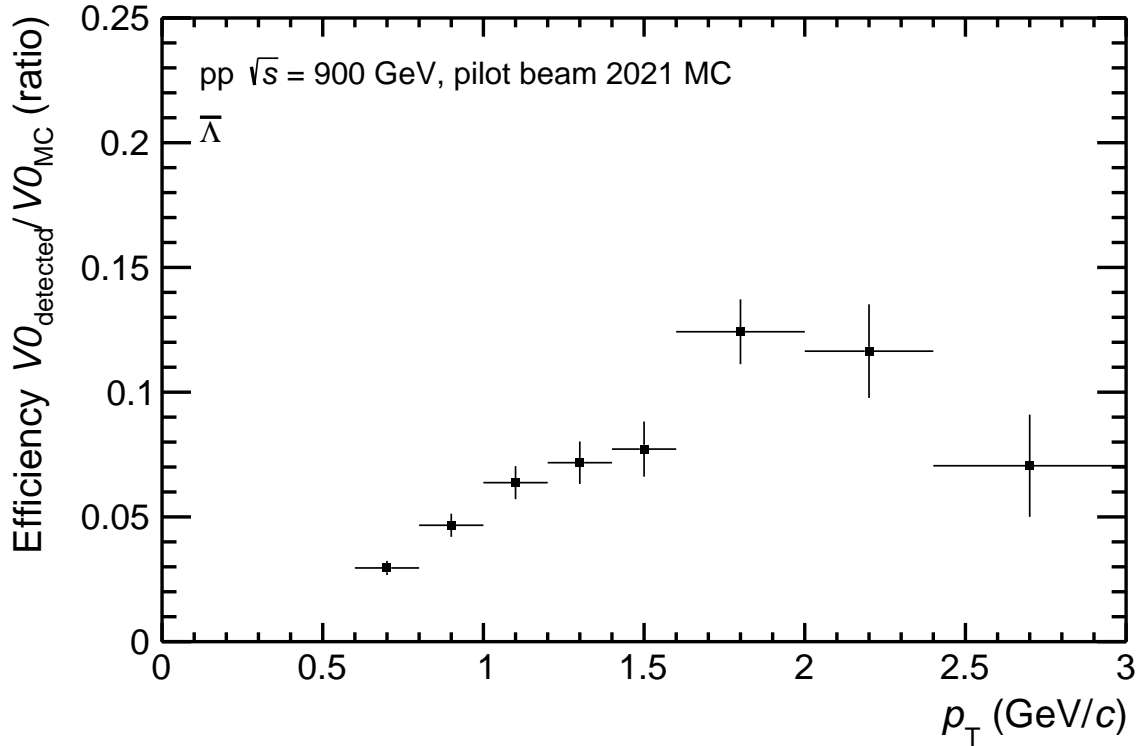
Figure 3.15: Reconstruction efficiency — $\overline{\Lambda}$.

comes from the decays $\Xi^- \to \Lambda + \pi^-$ and $\Xi^0 \to \Lambda + \pi^0$ for the former, and $\Xi^+ \to \overline{\Lambda} + \pi^+$ and $\overline{\Xi^0} \to \overline{\Lambda} + \overline{\pi^0}$ for the latter, according to [Aamodt et al. (2011)]. The decays of Ω also contribute to this abundance but the analysis of the Monte Carlo simulation shows a total of 3 and 0 Λ and $\overline{\Lambda}$ originating from the decay of an Ω, compared to 66 and 43 for Λ and $\overline{\Lambda}$ originating from Ξ. This contribution is negligible in regard to the uncertainties of the feeddown correction.

To correct for the reconstructed particles coming from a secondary vertex, an efficiency can be created using Monte Carlo information as in Eq. 3.8. The numerator $N_{reco}(\Lambda)^{\text{in bin i}}$ counts the number of Λ ($\overline{\Lambda}$) particles in a given p_{T} bin i that are reconstructed using the analysis detailed in this chapter (analysis cuts detailed in Table 3.2 and event selection detailed in Section 3.2.2), and whose Monte Carlo information confirms they correspond to the V0 decay studied $\Lambda \to p + \pi^-$ ($\overline{\Lambda} \to \overline{p} + \pi^+$) and have as mother a Ξ^- (Ξ^+). The denominator $N_{gen}(\Xi)$ counts all the Ξ^- (Ξ^+) that have been generated in the simulation with the condition that their rapidity y satisfies $|y| < 0.75$. This ratio can indeed be seen as a reconstruction efficiency for the secondary Λ because the branching ratios in question are of about 99.9% and 99.5% for charged and neutral Ξ to Λ, and because other sources of secondary Λ have been found negligible after analysis cuts.

$$F_i = \frac{N_{reco}(\Lambda)^{\text{in bin i}}}{N_{gen}(\Xi)} \tag{3.8}$$

67

Monte Carlo simulations do not reproduce well the Ξ spectrum seen in real data. Because the p_T of a secondary Λ is correlated with that of its mother Ξ, that discrepancy between the real data and MC spectrum of Ξ has an effect on the somewhat naive correction expressed in Eq. 3.8. To minimise this effect, the Ξ p_T spectrum is divided into several bins, and the correction factor are redefined in the form of a matrix as per Eq. 3.9. The matrix element F_{ij} is thus the number of Λ with p_T in the bin i coming from the disintegration of a Ξ with p_T in the bin j per generated Ξ with p_T in the bin j. The feeddown matrices for Λ and $\overline{\Lambda}$ are shown in Fig. 3.16. The p_T binning used for Ξ is the same as that of Λ.

$$F_{ij} = \frac{N_{reco}(\Lambda)_{\text{from } \Xi \text{ bin j}}^{\text{in bin i}}}{N_{gen}(\Xi)_{\Xi \text{ bin j}}} \tag{3.9}$$

Those ratios encoded in the feeddown matrix of Λ $(\overline{\Lambda})$ are then multiplied by the number $N(\Xi)_{\Xi \text{ bin j}}$ of measured Ξ^- (Ξ^+) in the j-th p_T bin of Ξ for the same dataset. This product is then summed over all the p_T bins of Ξ to get the expected number of Λ $(\overline{\Lambda})$ in the p_T bin i coming from the decay of any Ξ^- (Ξ^+). This quantity, the number $N(\Lambda_{\text{secondary}}^{\text{raw}})^{\text{in bin i}}$ of secondary Λ with p_T in the bin i that have passed the Λ signal extraction, is shown in Eq. 3.10. Subtracting $N(\Lambda_{\text{secondary}}^{\text{raw}})^{\text{in bin i}}$ from the total number $N(\Lambda_{\text{measured}}^{\text{raw}})^{\text{in bin i}}$ of Λ measured gives the corrected count $N(\Lambda_{\text{measured}}^{\text{raw}})^{\text{in bin i}}$ of primary Λ measured in the detector (Eq. 3.11).

$$N(\Lambda_{\text{secondary}}^{\text{raw}})^{\text{in bin i}} = \sum_j F_{ij} \cdot N(\Xi)_{\Xi \text{ bin j}} \tag{3.10}$$

$$N(\Lambda_{\text{primary}}^{\text{raw}})^{\text{in bin i}} = N(\Lambda_{\text{measured}}^{\text{raw}})^{\text{in bin i}} - N(\Lambda_{\text{secondary}}^{\text{raw}})^{\text{in bin i}} \tag{3.11}$$

The number $N(\Xi)$ of measured Ξ is calculated in Eq. 3.12 by integrating the p_T spectrum $\frac{dN}{dp_\mathrm{T}}(\Xi)$ over the p_T bin of interest.

$$N(\Xi)_{\Xi \text{ bin j}} = \int_{p_\mathrm{T}(\text{bin})} \frac{dN}{dp_\mathrm{T}}(\Xi) \tag{3.12}$$

The measurement of the Ξ p_T spectrum needed for this step has not necessarily been carried out using the same p_T bins as those used for the feeddown matrices. To circumvent this issue, the Ξ spectrum is fitted with a Lévy distribution [Wilk and Włodarczyk (2000)] as detailed in Eq. 3.13:

$$\frac{dN}{dp_\mathrm{T}}(\Xi) = N \cdot p_\mathrm{T} \cdot \frac{(n-1)(n-2)}{nT(nT + m_0(n-2))} \cdot \left(1 + \frac{\sqrt{p_\mathrm{T}^2 + m_0^2} - m_0}{nT}\right)^{-n} \tag{3.13}$$

where m_0 is the mass of the particle and N, n and T are fit parameters (N representing the total yield of the particle). This fit function has been used extensively in the analysis of multi-strange particles like the Ξ in pp collisions [Abelev et al. (2007), Abelev et al. (2012)] as it has been found to reproduce very well various transverse momentum distributions in high energy
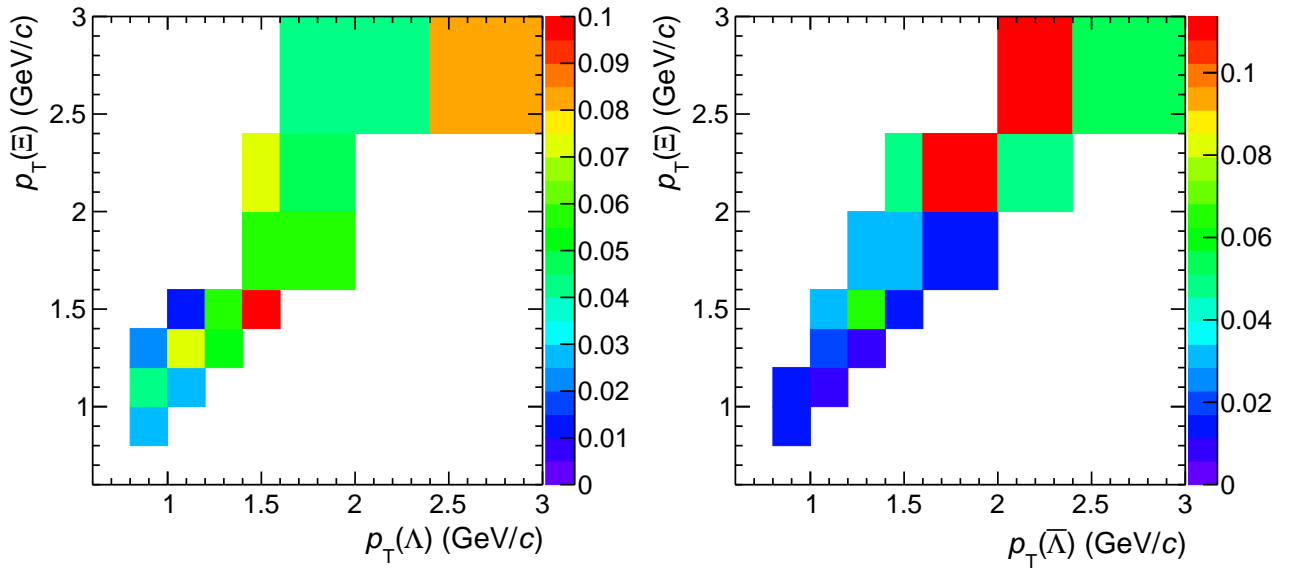
Figure 3.16: Feeddown matrix for Λ (left) and $\overline{\Lambda}$ (right) - p_{T} of Λ and $\overline{\Lambda}$ on the x-axis, p_{T} of Ξ on the y-axis.
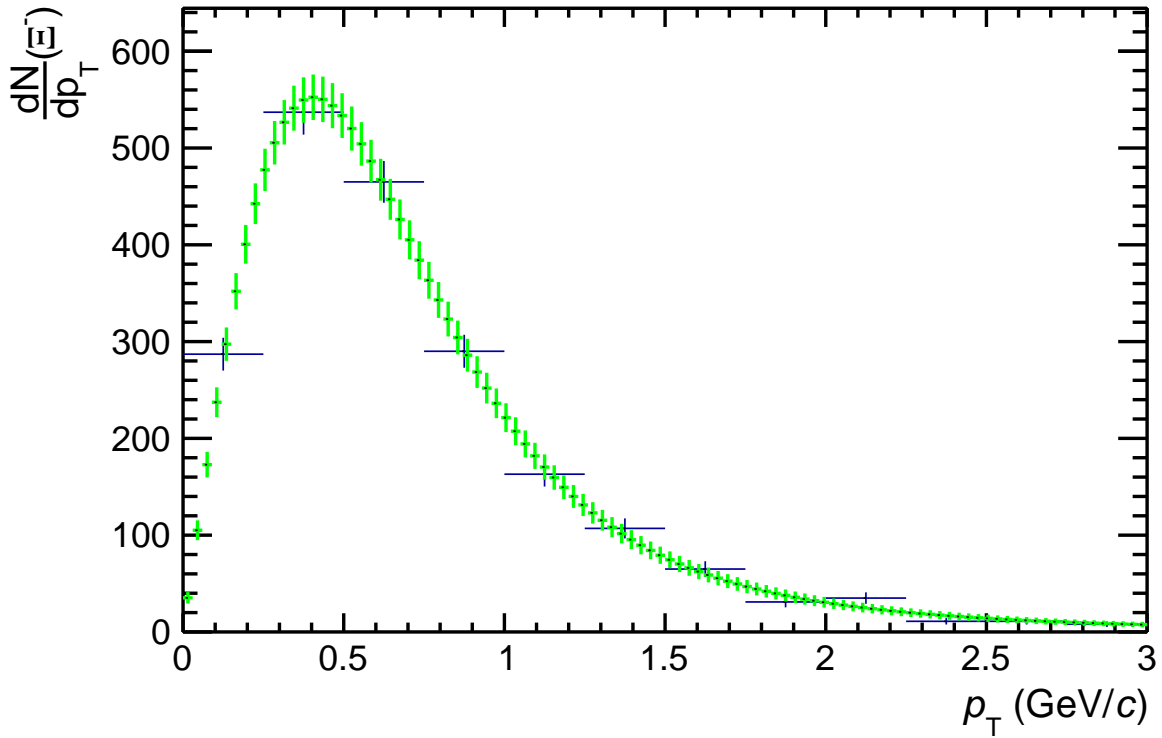
Figure 3.17: p_{T}-spectrum of Ξ^{-} (black) and the fitted Lévy function (green).

physics [Wilk and Włodarczyk (2000)]. Figure 3.17 shows the fit of this distribution in green, superimposed to the Ξ^- spectrum generated by the Monte Carlo simulation in black.

While only charged Ξ decays can be reconstructed due to Ξ^0 decaying in the vast majority of cases to a neutral π^0 that does not leave any trace in the detector [Tanabashi et al. (2018)], the contamination can come from both charged and neutral Ξ decays. To account for this, the numerator of the feeddown matrix is filled with Λ secondaries coming from both $\Xi^\mp$ and Ξ^0. This relies on the assumption that the Ξ^0 spectrum is similar to that of $\Xi^\mp$. The Monte Carlo simulation shows similar Lévy-fitted spectra for both species, with a maximum difference of ~2%.

Because the analysis of the Ξ p_{T}-spectrum has not been done for this Monte Carlo dataset, we substitute it for this thesis with the generated MC p_{T}-spectrum of Ξ.

To summarise, the correction term that has to be subtracted from the raw spectrum $\frac{\mathrm{d}^2 N_{raw}}{\mathrm{d}p_{\mathrm{T}}\mathrm{d}y}$ is $\frac{\mathrm{d}^2 N_{feeddown}}{\mathrm{d}p_{\mathrm{T}}\mathrm{d}y}$ as written in Eq. 3.14:

$$\frac{\mathrm{d}^2 N_{feeddown}}{\mathrm{d}p_{\mathrm{T}}\mathrm{d}y} = \frac{1}{\Delta p_{\mathrm{T}}} \cdot \frac{1}{\Delta y} \cdot N(\Lambda^{\mathrm{raw}}_{\mathrm{secondary}}) \tag{3.14}$$

where Δp_{T} is the width of the p_{T} bin for which $N(\Lambda^{\mathrm{raw}}_{\mathrm{secondary}})$ is being calculated, and where Δy is the rapidity range considered for the analysis ($\Delta y = 1.5$ here) that averages the spectrum over the rapidity interval $|y| < 0.75$.

Figure 3.18 shows the fraction of raw yield removed by the feeddown correction for both Λ and $\overline{\Lambda}$ in this analysis. The fractions are expected to show similar values between Λ and $\overline{\Lambda}$, however the apparent differences seen in this plot are not significant in this analysis given the very large statistical uncertainties (due to a lack of entries in the numerator of the feeddown matrix, only 43 and 66 for Λ and $\overline{\Lambda}$ respectively split between the non-empty bins shown in Fig. 3.16.

In theory, the feeddown could also be calculated without having to involve MC data (and its associated systematic uncertainty), by using the fact that the pointing angle or the DCA of the V0 to the primary vertex of a secondary V0 would tend to be larger than those of a primary V0. A fit on the distribution of those variables could give a measurement of the feeddown. This technique has so far not been used in ALICE, despite the advantage of only involving real data, because it relied heavily on a variable that the experiment was not very good at reproducing: the pointing to the primary vertex.

3.2.8 Corrected spectrum

With the raw spectrum $\frac{\mathrm{d}^2 N_{raw}}{\mathrm{d}p_{\mathrm{T}}\mathrm{d}y}$ extracted from the data (Eq. 3.6), and the efficiency correction factor $\epsilon(p_{\mathrm{T}})$ and feeddown correction term $\frac{\mathrm{d}^2 N_{feeddown}}{\mathrm{d}p_{\mathrm{T}}\mathrm{d}y}$ having been calculated (Eq. 3.7 and 3.14), the corrected spectrum $\frac{\mathrm{d}^2 N}{\mathrm{d}p_{\mathrm{T}}\mathrm{d}y}$ can be computed with Eq. 3.15. A normalisation to
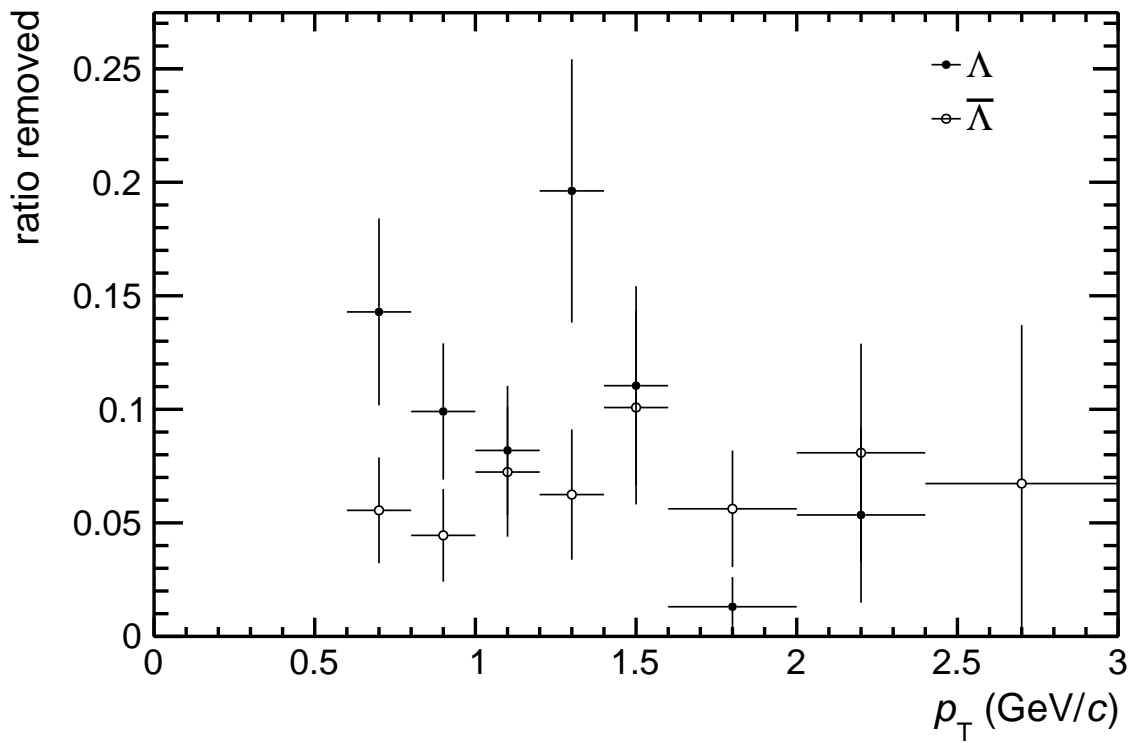
Figure 3.18: Fraction of Λ (full circles) and $\overline{\Lambda}$ (empty circles) raw spectra removed due to feeddown subtraction of charged and neutral Ξ.

the number of events N_{event} that pass the event selection (see subsection 3.2.2) is applied to the spectra to allow for a comparison to other measurements done in ALICE or other experiments with a different set of collisions.

$$\frac{\mathrm{d}^2 N}{\mathrm{d}p_{\mathrm{T}}\mathrm{d}y} = \frac{1}{N_{event}} \cdot \frac{1}{\epsilon(p_{\mathrm{T}})} \cdot \left(\frac{\mathrm{d}^2 N_{raw}}{\mathrm{d}p_{\mathrm{T}}\mathrm{d}y} - \frac{\mathrm{d}^2 N_{feeddown}}{\mathrm{d}p_{\mathrm{T}}\mathrm{d}y} \right) \tag{3.15}$$

3.2.9 Uncertainties

A measure means nothing without its associated uncertainty. Two sources of uncertainties can be distinguished. Statistical uncertainties arising from the amount of data available for the analysis, and systematic uncertainties arising from the analysis procedure.

Statistical Uncertainties

The calculation of statistical uncertainties for this analysis mostly relies on the fact that the analysis presented in this thesis is at its core a counting experiment. The number of entries in an invariant mass histograms such as the ones described in subsection 3.2.4 are random Poisson processes [Barlow (2000)]. The uncertainty for such a bin with $N_{entries}$ entries is simply given by the Poisson standard deviation $\sqrt{N_{entries}}$.

The determination of the uncertainties for the efficiencies involves a different type of random process. The application of the various selections used in this analysis can be seen on first approximation [Ullrich and Xu (2007)] as Binomial processes with probability of success the efficiency ϵ and number of experiments the number N_{gen} of generated particles of the species considered. The standard deviation of such a Binomial process is $\sqrt{\frac{\epsilon(1-\epsilon)}{N_{gen}}}$.

Systematic Uncertainties

The analysis of the analysis itself can unveil several aspects of it that can be the origin of new uncertainties, that do not arise from statistical fluctuations but from the analysis recipe.

The following sources of systematic uncertainties have been considered, mainly having to do with the signal extraction procedure:

- **Invariant mass binning change**: the impact of the choice of invariant mass binning for the signal extraction procedure has been studied by varying it and looking at the deviations in corrected yield with the binning detailed in 3.2.5. The alternative binning that have been considered are: 200 bins, 80 bins and 20 bins instead of 40 for K_S^0, 200 bins, 50 bins and 40 bins instead of 100 for Λ and $\overline{\Lambda}$.

- **Background extrapolation**: an alternative method to the extrapolation of the background inside the signal window has been tried, that does not rely on a fit to the background. Instead of integrating the line function fitted to the background, the background is averaged by counting the number of entries in the side band region $]\mu - 2L\sigma; \mu - L\sigma[\cup]\mu + L\sigma; \mu + 2L\sigma[$. Keeping the assumption of a linear background, and given the size of the side band region is the same as that of the signal region $]\mu - L\sigma; \mu + L\sigma[$, one gets $N_{bkg}(]\mu - 2L\sigma; \mu - L\sigma[\cup]\mu + L\sigma; \mu + 2L\sigma[) = N_{bkg}(]\mu - L\sigma; \mu + L\sigma[)$.

- **Signal window size**: the signal extraction and efficiency calculation have been carried out with $L = 4$ (subsection 3.2.5). The influence of a variation of the signal region size is checked with alternative values for L: $L = 3.5$ and $L = 3$.

Each of those systematic studies yields a corrected spectrum as calculated per Eq. 3.15, and most probably a difference between this new value and the one obtain with the standard analysis detailed in the previous subsections. Is this difference significant? Or does it most probably arise from statistical fluctuations? Roger Barlow presents in a lecture of his on statistics [Barlow (2000)] a test that allows for an informed decision. Given two estimators $\hat{a}_1$ and $\hat{a}_2$ of a quantity a with statistical uncertainties σ_1 and σ_2, their difference $\Delta = \hat{a}_1 - \hat{a}_2$ has a statistical uncertainty σ_Δ, often called σ_{Barlow} that can be calculated in practice [Barlow (2000)] as per Eq. 3.16:

$$\sigma_{Barlow} = \sqrt{|\sigma_1^2 - \sigma_2^2|} \tag{3.16}$$

This σ_{Barlow} can then be compared to the difference $\Delta_{spectra}$ between the reference spectrum and the one obtained in the systematic study, for each p_T bin. This thesis chooses to only consider differences larger than $2\sigma_{Barlow}$. This is the threshold chosen in various other strangeness analyses. If a systematic test yields a difference larger than this threshold, the difference $\Delta_{spectra}$ is added to the systematic uncertainty for the particle spectrum.

Other sources of systematic uncertainties are usually considered for the analysis of strange particles and the calculation of their p_T spectrum. However due to the simulated nature of the dataset used in this analysis, most of them have not been considered. For example:

- material budget: the detector model used in the efficiency and feeddown corrections is perfect and one hundred percent accurate given that the data studied in this thesis and the MC simulation used for the efficiency and feeddown are one and the same.

- variation of analysis cuts: this systematic study controls the errors arising from discrepancies between data and MC simulation for the distributions on which those cuts are applied. Given the absence of such discrepancies in this study, any difference in the spectra obtained by varying the cuts should only arise from statistical effects. Tests have indeed been made and the differences stayed below the $2\sigma_{Barlow}$ threshold.

From the considered sources of systematic uncertainties, only the variation of the invariant mass binning has been found to have an effect that is likely to not arise from statistical fluctuations, and this only for the corrected spectrum of K_S^0. The systematic uncertainties attributed to the choice of the invariant mass binning have been plotted in Fig. 3.19 as a percentage of the corrected spectrum value, as a function of p_T. Only a few bins show differences above $2\sigma_{Barlow}$. For Λ and $\overline{\Lambda}$, the effect of the systematic uncertainty sources were all below the $2\sigma_{Barlow}$ threshold.

Combination of uncertainties

Uncertainties can be combined by propagating them using differentiation. For any new quantity $f(x, y)$ depending on two quantities x and y, the uncertainty σ_f can be calculated from the uncertainties σ_x and σ_y and from the covariance matrix σ_{xy} using the formula for error propagation shown in Eq. 3.17. Those rules hold for the combination of systematic errors.

$$\sigma_f^2 = \left(\frac{\partial f}{\partial x}\right)^2 \sigma_x^2 + \left(\frac{\partial f}{\partial y}\right)^2 \sigma_y^2 + 2\frac{\partial f}{\partial x}\frac{\partial f}{\partial y}\sigma_{xy} \tag{3.17}$$

The most common formulae derived from Eq. 3.17 that are used in this analysis are as follows:

$$\sigma_{A-B}^2 = \sigma_A^2 + \sigma_B^2 \tag{3.18}$$

for A and B uncorrelated quantities, used for example in Eq. 3.5,

$$\sigma_{aA}^2 = a^2\sigma_A^2 \tag{3.19}$$

for a a fixed parameter, used for example in Eq. 3.6.

$$\sigma_{AB}^2 = B^2 \cdot \sigma_A^2 + A^2 \cdot \sigma_B^2 \tag{3.20}$$

for A and B uncorrelated quantities, used in Eq. 3.10.

$$\sigma_{A/B}^2 = \frac{\sigma_A^2}{A^2} + \frac{\sigma_B^2}{B^2} \tag{3.21}$$

for A and B uncorrelated quantities, used in Eq. 3.15.

The final statistical and systematic uncertainties on the corrected spectra are combined in quadrature.
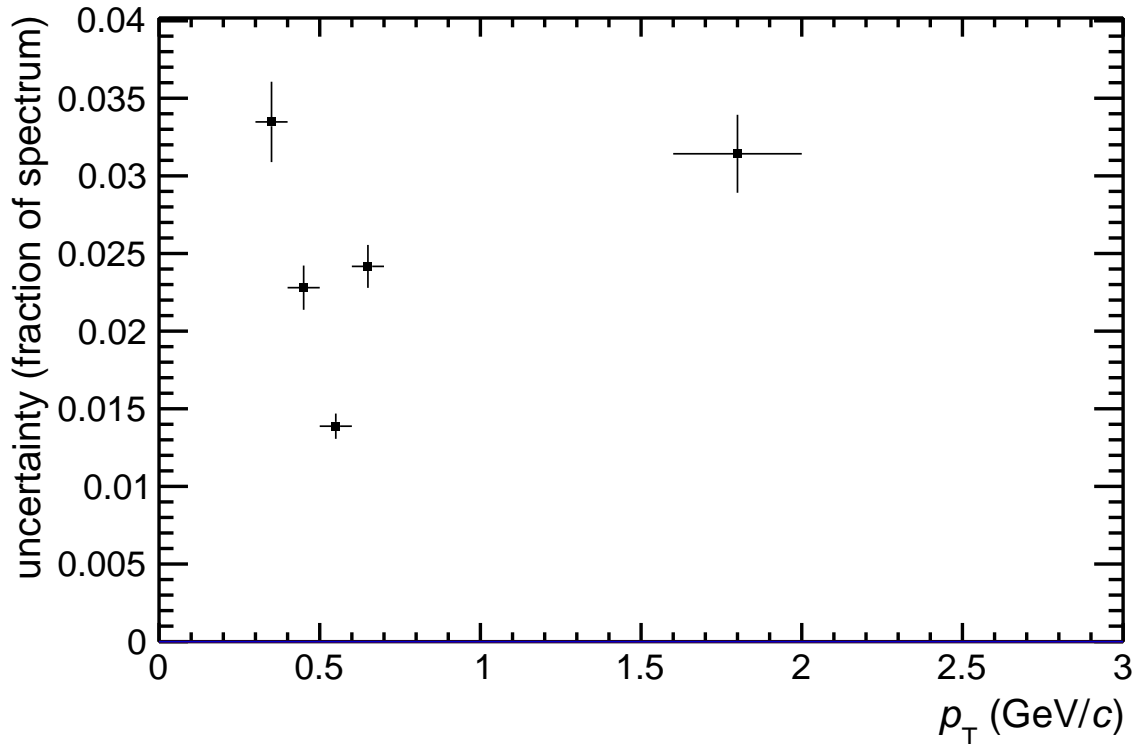
Figure 3.19: Systematics for K_S^0.

3.2.10 Results

The corrected spectra, results of the analysis detailed in this section, are displayed for K_S^0 in Fig. 3.20, for Λ in 3.21, and for $\overline{\Lambda}$ in Fig. 3.22. They are compared to the distributions of primary particles of the corresponding species generated in the Monte Carlo simulation. The uncertainties are mainly statistical, and are rather large for Λ and $\overline{\Lambda}$ low data. Figures 3.23, 3.24 and 3.25 give a better idea of the fidelity of the reconstructed spectra by looking at their ratio with the Monte Carlo generated spectra. Some of the points seem a little too far away from the ratio value 1 even when taking the error bars into account, like for K_S^0 at $p_\mathrm{T} \in$ [0.2, 0.3] GeV/c. The error bar is only a representation of one single standard deviation around the estimated value, i.e. a representation of a confidence level of about 68%. What this means is that if a measurement of the same quantity was carried out many times, it would fall 68% of the time within the error bars. It is not a sharp cutoff. Thus, given how small the deviations are compared to the limits set by the error bars, said deviations are not significant. The spectra built with this analysis are in good agreement with the initial generated distributions when taking the uncertainties into account. This analysis thus has succeeded in extracting the V0 particle spectra from the data that it was fed, as far as can be assessed with the studied dataset, and thus gives good confidence that the V0 reconstruction does good work.
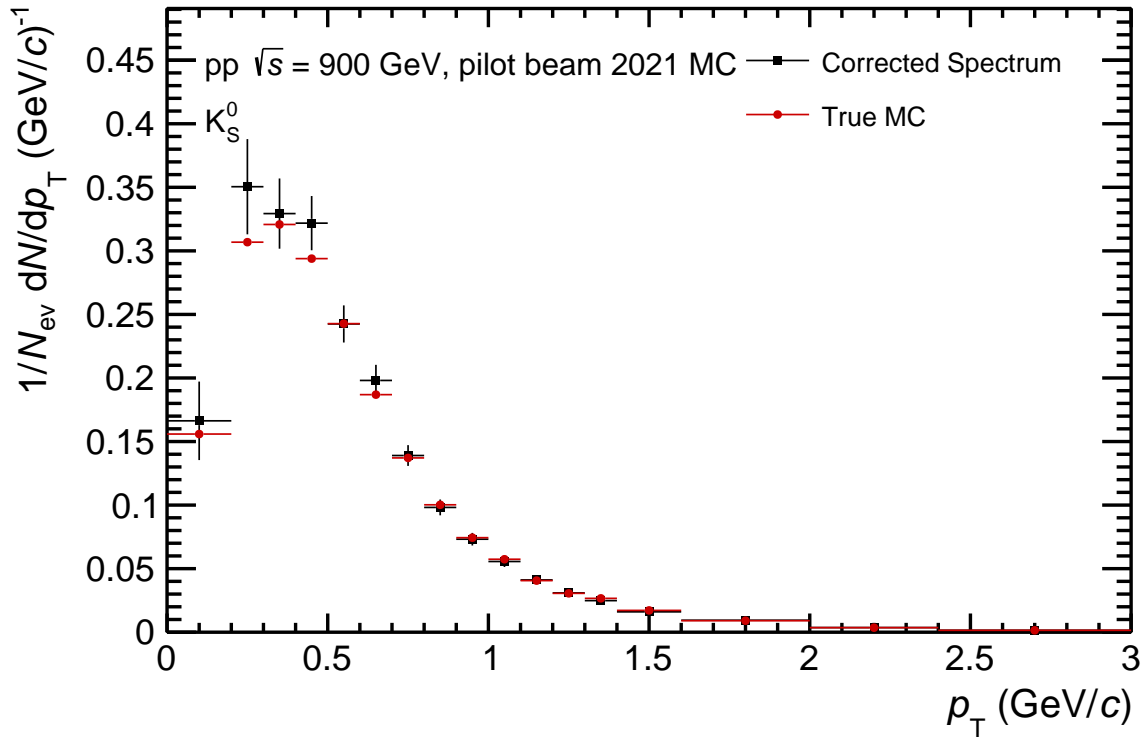
Figure 3.20: Corrected spectrum of K^0_S.
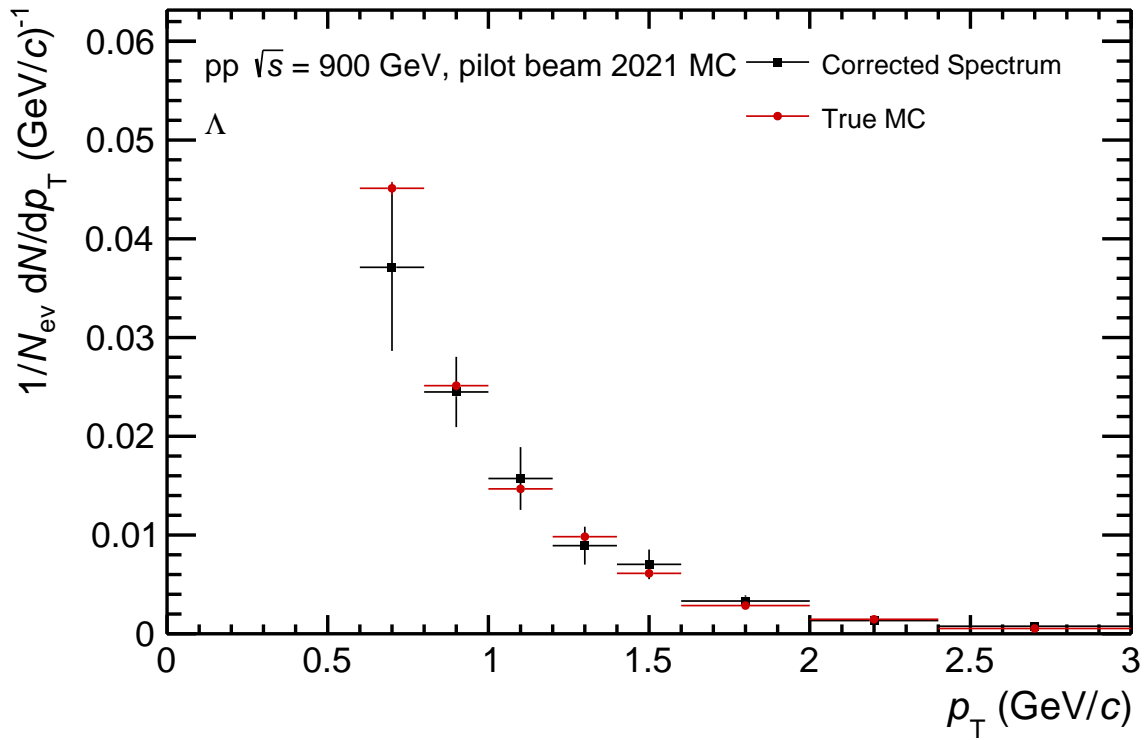
Figure 3.21: Corrected spectrum of Λ.
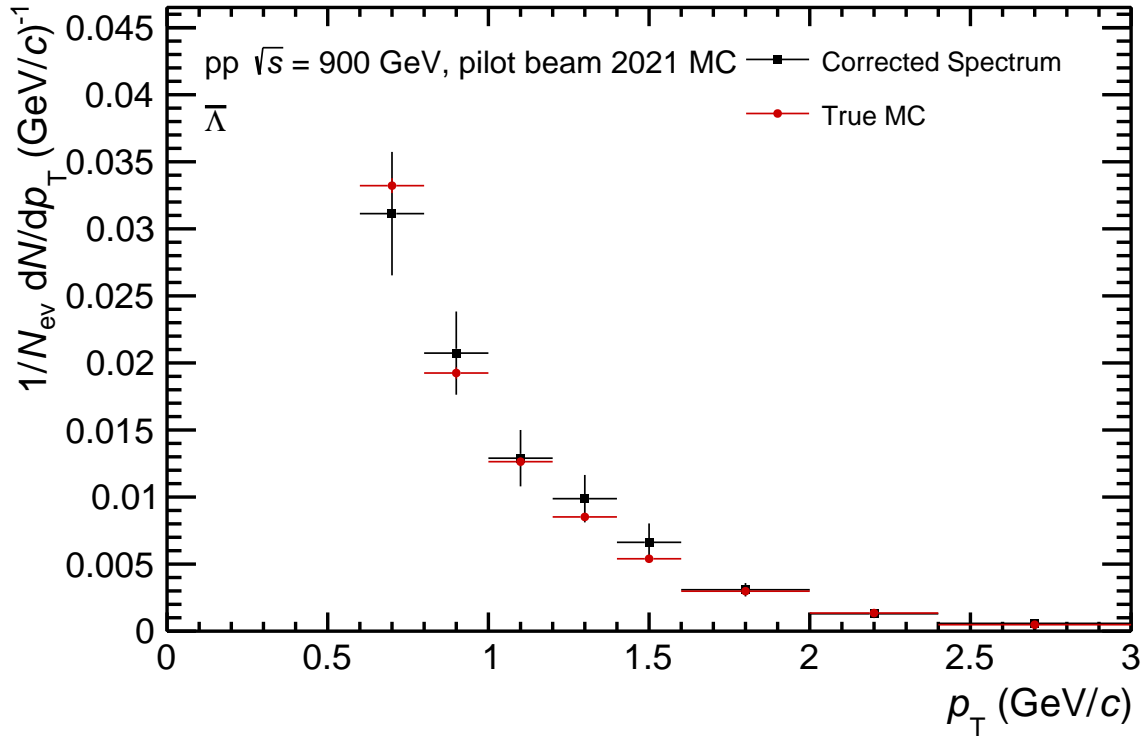
Figure 3.22: Corrected spectrum of $\overline{\Lambda}$.
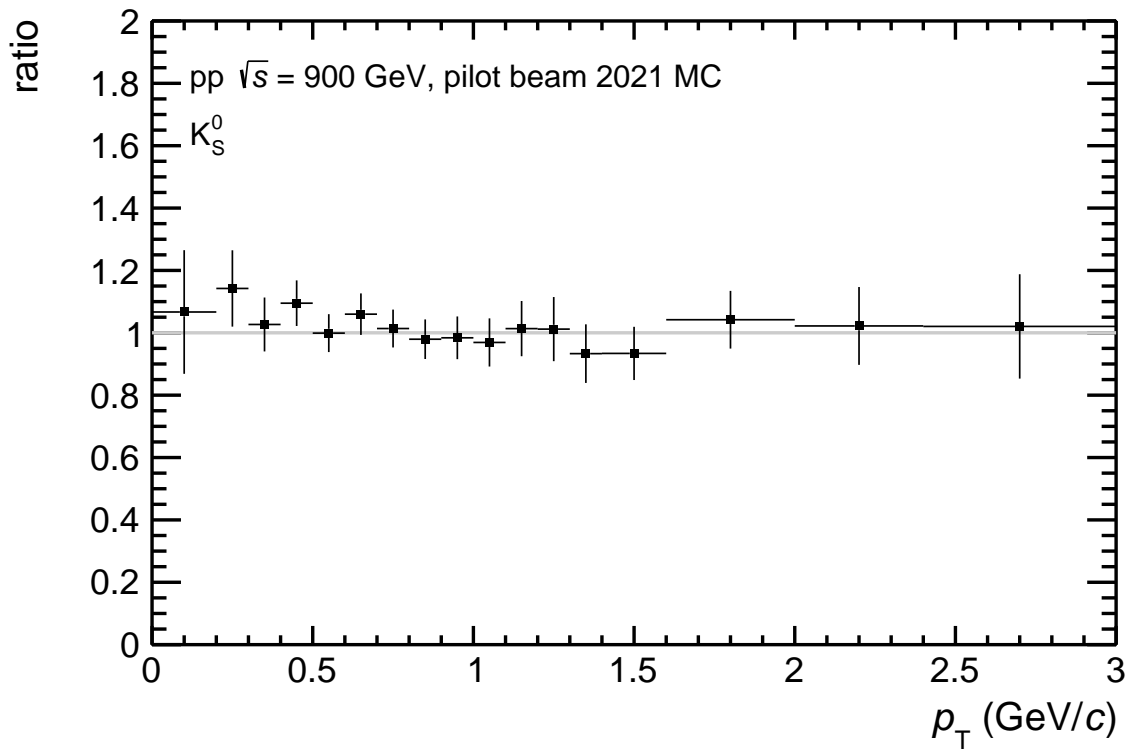
Figure 3.23: Ratio of corrected to generated spectrum for K_S^0 – a horizontal grey line is drawn at ratio = 1 to make the interpretation easier.
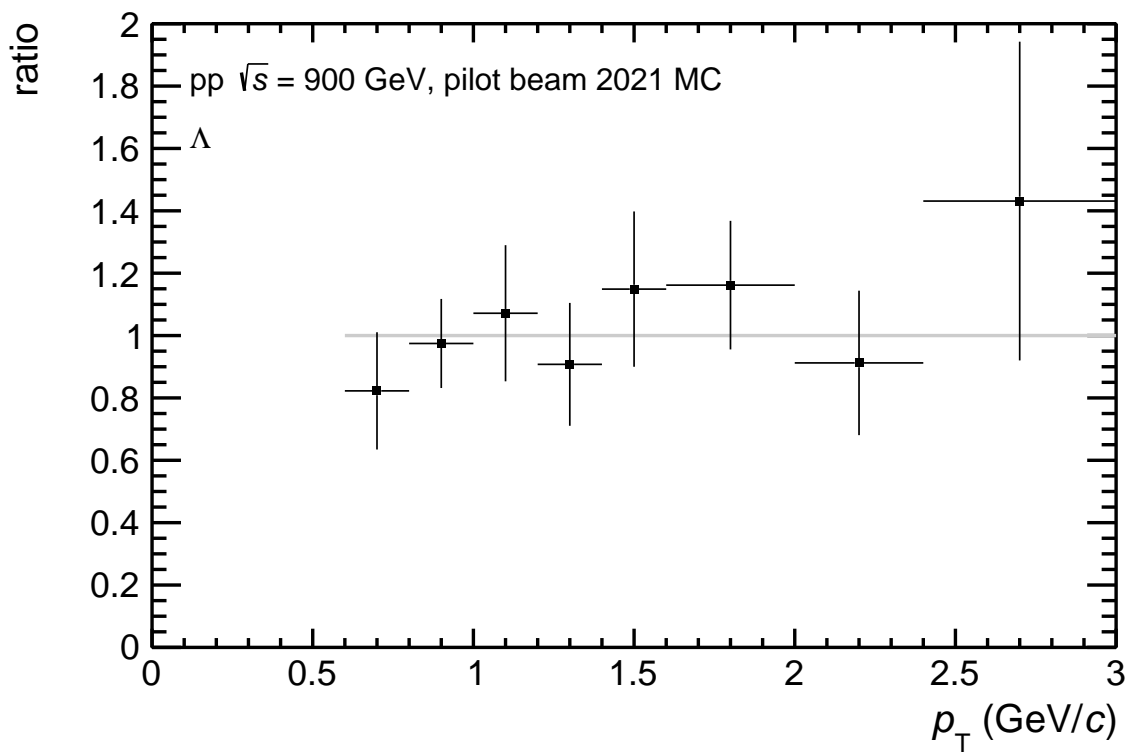
Figure 3.24: Ratio of corrected to generated spectrum for Λ – a horizontal grey line is drawn at ratio $= 1$ to make the interpretation easier.

Figure 3.25: Ratio of corrected to generated spectrum for $\overline{\Lambda}$ – a horizontal grey line is drawn at ratio = 1 to make the interpretation easier.

3.3   Discussion about the analysis

This section discusses a few points about the reconstruction performance shown in this analysis, then looks at preliminary results obtained with the real pilot beam data.

3.3.1   Comparison with the Run 1 strangeness analysis

The analysis cuts in this thesis have been chosen to be similar to those in the strange particle analysis from Run 1 [Aamodt et al. (2011)], in order for a comparison to be possible. What can be seen looking at the efficiencies presented in Fig. 3.13, 3.14 and 3.15 is that they are smaller than those obtained in the Run 1 analysis, that are displayed in Fig. 3.26 in a similar p_T range, about a factor 2.5 smaller. This observation holds when comparing to Run 2 efficiencies in pp collisions at higher energies, given they are for K_S^0 and Λ similar to those of Run 1 as can be seen in Fig. 3.27, the analysis cuts being very similar in Run 1 and 2 for the analysis of V0 decays.

In section 3.2.3, is discussed the fact that the secondary vertex reconstruction has been done with two cuts already tighter than in the Run 1 analysis, due to resource consumption considerations. On the V0 transverse decay radius, and on the DCA between the daughters and the primary vertex. Thus, a first hint as to the origin of this efficiency decrease. Unfortunately, all the intermediary simulation and reconstruction files, that would have been necessary to another run of the secondary vertex reconstruction (described in 3.1) with different cut values, are generally not kept and were thus not available. Thus, to check if releasing those two cuts would indeed explain the difference, a toy study has been done using the same AO2D data file used in this analysis. A new set of V0 candidates was created by looping over all the possible pairs of positive and negative tracks that are saved in the AO2D, propagating them to their PCA with the same DCA minimisation algorithm as the one used in the standard V0 reconstruction and described in 3.1 and keeping the pairs of tracks for which it succeeded. The exact same analysis as described in section 3.2 has then been applied to this new set of V0 candidates, with the only exception that the cuts on the V0 transverse decay radius and on the DCA between the daughters and the primary vertex have been relaxed to match their values in the Run 1 analysis: $0.2\,\mathrm{cm}$ and $0.05\,\mathrm{cm}$ respectively.

The new efficiency obtained in this toy analysis is plotted in Fig. 3.28 for K_S^0. Because this finding of the initial V0 candidates lacks many of the subtleties of the actual secondary vertex reconstruction, they are compared to the same analysis done this time with the two cuts kept at the values set in the actual reconstruction step (3.1). An increase in the efficiency of about 25% can be observed in the asymptotic with the loosened cuts. This larger efficiency obtained with this alternative V0 finding method is still lower than that observed in Run 1 and 2. However, the track reconstruction efficiency has also been found lower in general for this Run 3 Monte
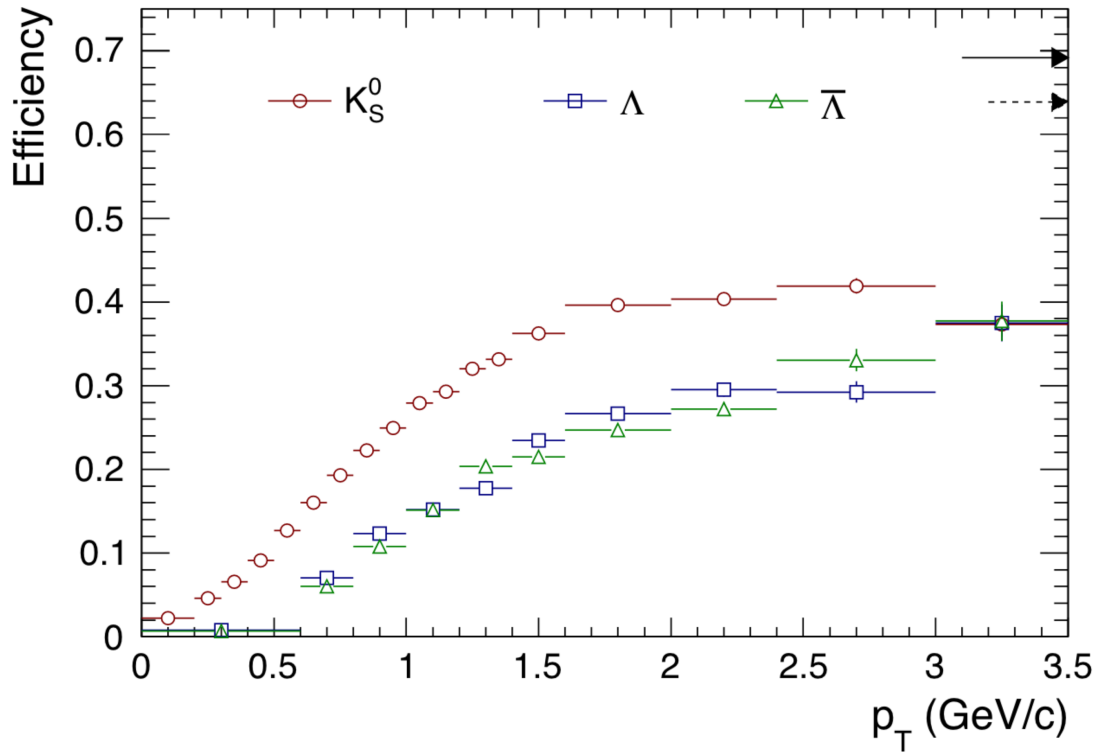
Figure 3.26: Efficiencies of K_S^0, Λ and $\overline{\Lambda}$ in the Run 1 analysis of pp collisions at $\sqrt{s}$ =900 GeV — taken from [Aamodt et al. (2011)].

ALI-PERF-145095
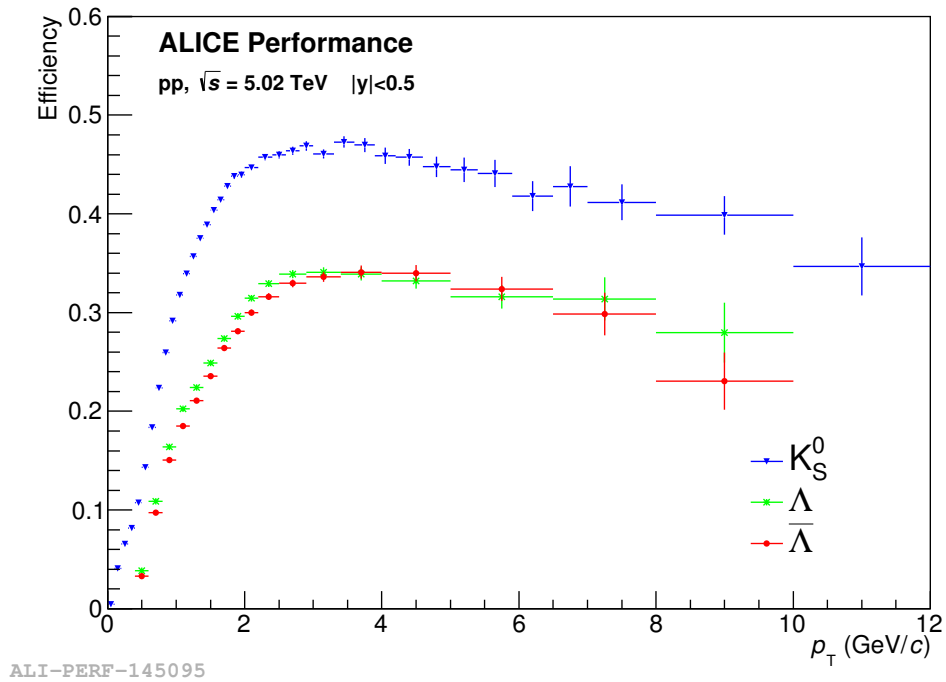
Figure 3.27: Efficiencies of K_S^0, Λ and $\overline{\Lambda}$ in Run 2 for pp collisions at $\sqrt{s}$ =5.02 TeV.

Carlo simulation compared to Run 2, as can be seen in Fig. 3.29, where the tracking efficiency (after the usual analysis track cuts in rapidity, TPC number of clusters, dE/dx distributions and the ITS-TPC matching requirement, which lower the tracking efficiency to 80 % in Run 2) is plotted for Run 2 pp data and for the Run 3 Monte Carlo dataset analysed in this thesis (LHC22c5). Thus, because it relies on the reconstruction of the two daughter tracks, a lower V0 reconstruction efficiency in this Run 3 dataset is not unexpected.

The observed 25% increase in efficiency was deemed large enough to warrant a loosening of the cuts despite the additional computing cost, and a release of the cuts has been approved after discussion with the reconstruction specialists, for the next large scale Monte Carlo simulation and for the data taking. It can also be seen that the lowest efficiency in this plot is still greater than that seen in section 3.2.6 in Fig. 3.13. Thus some other cuts might gain to be loosened in the secondary vertex reconstruction, although the impact on the reconstruction speed shall again have to be factored in. Λ and $\overline{\Lambda}$ show similar trends.

3.3.2   First look at the pilot beam data

While the full reconstruction of the asynchronous pass 4 was not released until late this year, a small preview was made accessible earlier in April. A portion of the analysis detailed in this thesis, with no efficiency or feed-down corrections applied, was run on this sample. Invariant mass plots have been plotted for Λ, $\overline{\Lambda}$ and K_S^0 in Fig. 3.30: clearly defined peaks can be seen in the data. The raw spectrum was extracted for K_S^0. This raw spectrum has been compared to the fully corrected spectrum published in the Run 1 analysis [Aamodt et al. (2011)]. Both analysis look at the same collision system (proton-proton at $\sqrt{s} = 900\,\text{GeV}$), and both spectra are normalised to the number of collision in their respective dataset. Thus, plotting the ratio of the pilot beam raw spectrum to the corrected spectrum of the Run 1 analysis gives a pseudo V0 reconstruction efficiency in the pilot beam data, the Run 1 corrected spectrum acting like the generated K_S^0 distribution in Eq. 3.7. This plot is shown in Fig. 3.31. This plot reveals an apparent discrepancy between the reconstruction efficiency performance in the pilot beam data and that in the Monte Carlo simulation of said pilot beam, the latter being about four times as high. If an analysis of this pilot beam data was to use the efficiency calculated using this Monte Carlo production, the corrected spectrum obtained with it would thus be three times as low as that measured in Run 1. The exact source of this probable calibration issue in those first preliminary results is under investigation.
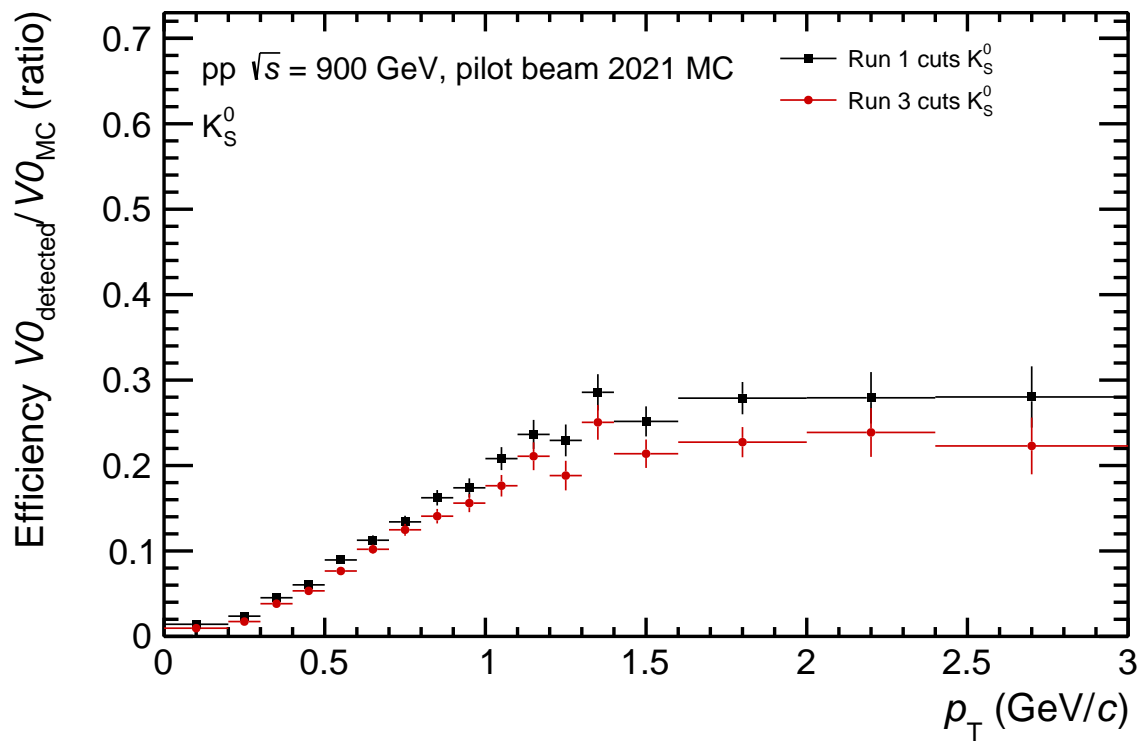
Figure 3.28: K_S^0 efficiencies with cut values similar to those in this thesis' Run 3 analysis (in red) and with cut values similar to those in the Run 1 analysis (in black).
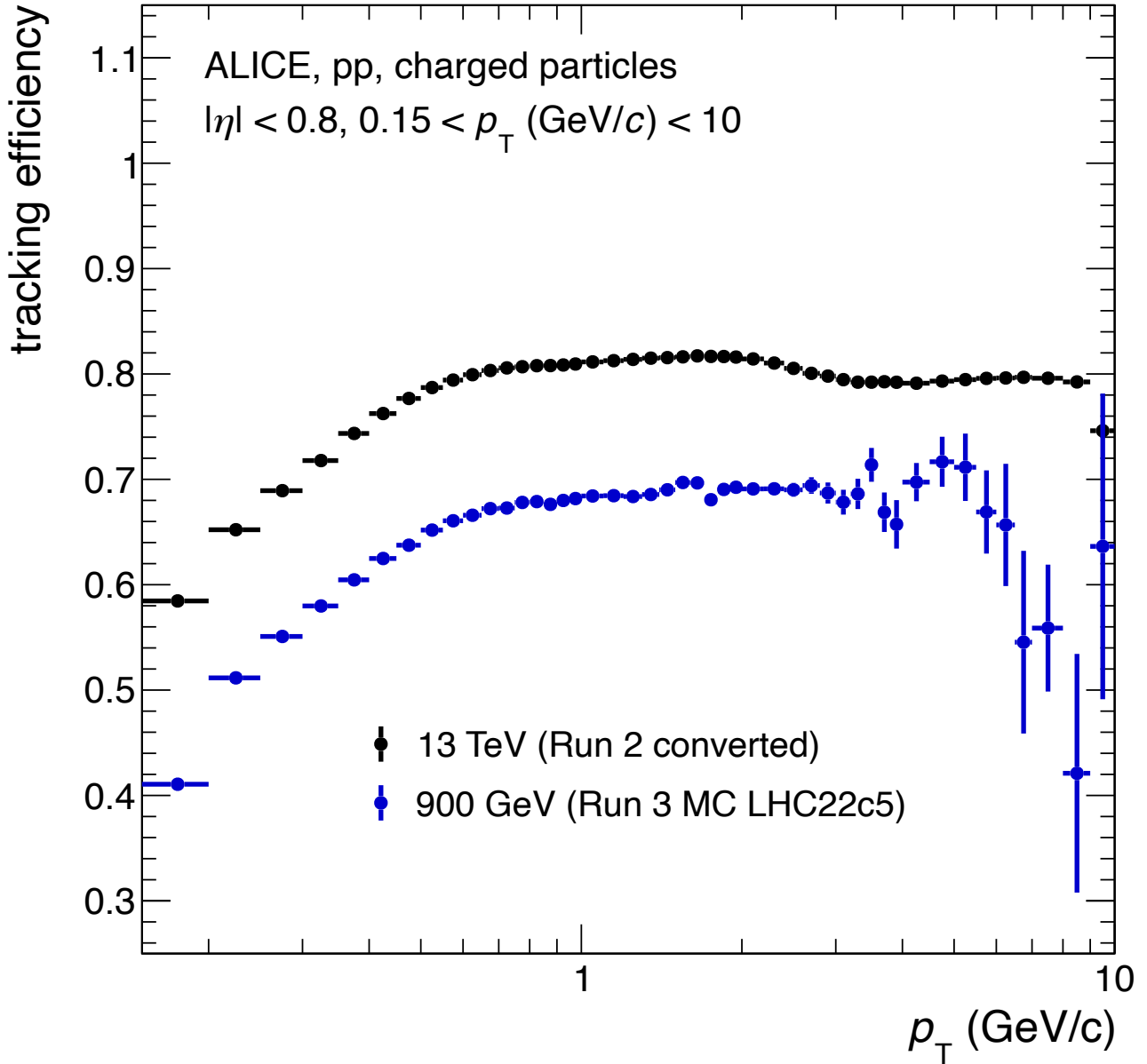
Figure 3.29: Tracking efficiencies in Run 2 for pp collisions at $\sqrt{s} = 13\,\text{TeV}$ (black) and Run 3 for the LHC22c5 MC production analysed in this thesis (blue) — many thanks to Mario Kruger for this plot.
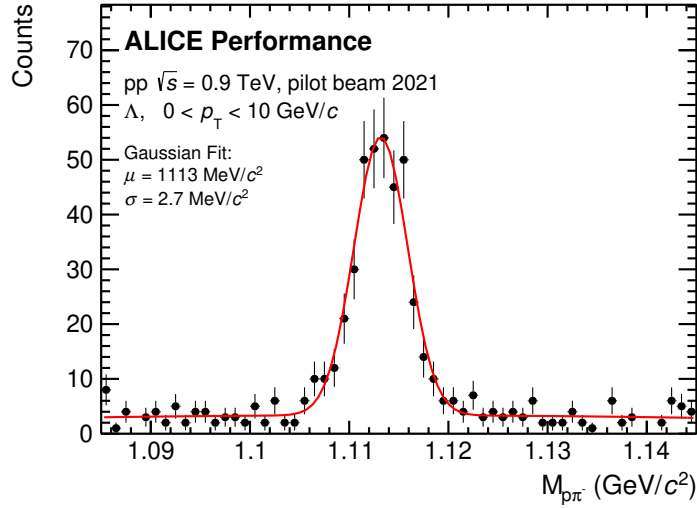
ALI-PERF-502948
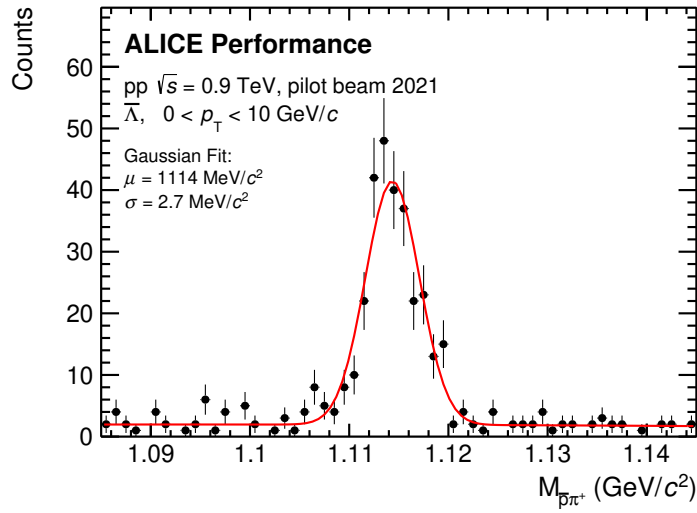
ALI-PERF-502943
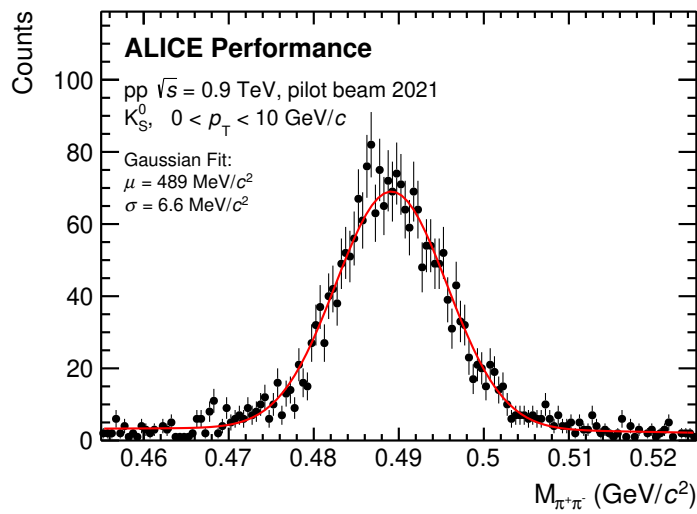
ALI-PERF-502953

Figure 3.30: Invariant mass distributions of Λ (top), $\overline{\Lambda}$ (centre) and K_S^0 (bottom) for the analysed subset of pilot beam data — in red the fit function described in 3.2.5.
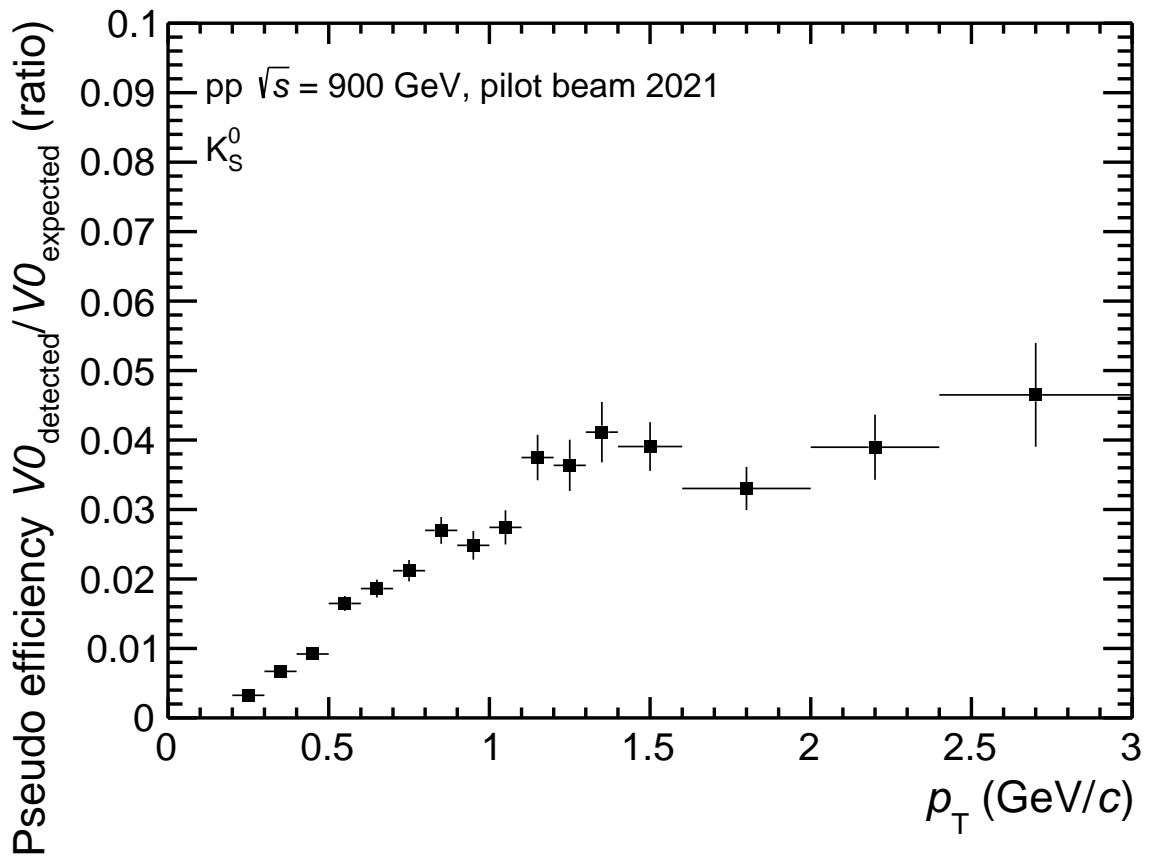
Figure 3.31: Pseudo efficiency of K_S^0 reconstruction in the pilot beam.

Conclusion

The ALICE experiment underwent between the end of 2018 and the middle of 2022 a major upgrade of its detector and of its reconstruction and analysis software, in order to allow for the continuous recording of collisions, without trigger, happening at a much increased interaction rate. A test of the new reconstruction software, and analysis framework of the newly upgraded ALICE experiment has been carried with a Monte Carlo simulation of the October 2021 pilot beam proton-proton collisions, at a total collision energy $\sqrt{s} = 900\,\text{GeV}$. This test focused on investigating the performances of the reconstruction of V0 decays, the building blocks for the analysis of strange decays, themselves valuable probes of the quark gluon-plasma, and of the analysis workflow developed during this thesis inside the new analysis framework for the analysis of those reconstructed V0 decays.

The transverse momentum spectra of the reconstructed K_S^0, Λ and $\overline{\Lambda}$ have been computed and compared to the initial spectra generated by the simulation. The details of this analysis, adapted during this thesis in the form of an analysis workflow combined with a post processing macro to produce the various histogram shown in this thesis, have been presented. The reconstruction software, the analysis workflow, and the post-processing code are all functioning and together they succeed in reproducing the generated spectra.

The reconstruction efficiencies obtained in this thesis have been compared to those presented in previous analyses from before the upgrade. The efficiencies are found to be lower in this Run 3 analysis and this observation has prompted a loosening of some of the reconstruction cuts, the additional computing load having been deemed acceptable for the potential improvement. The slight efficiency performance decrease is however counterbalanced by the increase of the size of the collision dataset that ALICE will analyse in Run 3. Indeed, with the increased interaction rate and the switch to a continuous readout, ALICE will see a lot more collisions than before the upgrade. The planned integrated luminosity for Pb-Pb in Run 3 is $10\,\text{nb}^{-1}$, ten times more than the $1\,\text{nb}^{-1}$ integrated luminosity gathered during Run 2, up to a hundred times more for minimum bias analyses as only about a tenth of Run 2 data was usable for those due to detector dead time while the $10\,\text{nb}^{-1}$ of Run 3 will all be minimum bias. With the new efficiency being about twice as low as the Run 2 efficiency, this means that the detector should still see about five times more strange particles in Run 3, up to fifty times more for minimum bias analyses.

A discrepancy between the reconstruction efficiency in Monte Carlo data and real data, linked to an imperfection in the calibration of the first preliminary results from real data, is

also observed.

With a globally successful V0 reconstruction in the new framework, a check of the reconstruction performance of more elaborate decay chains from multi strange particles has begun on the recently fully released asynchronous pass 4 of reconstruction of the 2021 pilot beam. But this is only a first step: already Run 3 has started in July 2022, with its first proton-proton collisions at $13.6\,\mathrm{TeV}$, and the first lead-lead collisions are coming in November 2022.

Bibliography

Aamodt, K. et al. (2008). ALICE Collaboration, "The ALICE experiment at the CERN LHC". In: JINST 3, S08002. DOI: 10.1088/1748-0221/3/08/S08002.

— (June 2010). ALICE Collaboration, "Charged-particle multiplicity measurement in proton–proton collisions at $\sqrt{s} = 0.9$ and 2.36 TeV with ALICE at LHC". In: The European Physical Journal C 68.1-2, pp. 89–108. DOI: 10.1140/epjc/s10052-010-1339-x. URL: https://doi.org/10.1140%2Fepjc%2Fs10052-010-1339-x.

— (Mar. 2011). ALICE Collaboration, "Strange particle production in proton–proton collisions at $\sqrt{s} = 0.9$ TeV with ALICE at the LHC". In: The European Physical Journal C 71.3. DOI: 10.1140/epjc/s10052-011-1594-5. URL: https://doi.org/10.1140%2Fepjc%2Fs10052-011-1594-5.

Abelev, B. et al. (June 2007). STAR Collaboration, "Strange particle production in $p + p$ collisions at $\sqrt{s} = 200$ GeV". In: Phys. Rev. C 75 (6), p. 064901. DOI: 10.1103/PhysRevC.75.064901. URL: https://link.aps.org/doi/10.1103/PhysRevC.75.064901.

— (2012). ALICE Collaboration, "Multi-strange baryon production in pp collisions at $\sqrt{s} = 7$ TeV with ALICE". In: Phys. Lett. B 712, pp. 309–318. DOI: 10.1016/j.physletb.2012.05.011. arXiv: 1204.0282 [nucl-ex].

— (2014a). ALICE Collaboration, "Technical Design Report for the Upgrade of the ALICE Inner Tracking System". In: J. Phys. G 41, p. 087002. DOI: 10.1088/0954-3899/41/8/087002.

— (2014b). ALICE Collaboration, "Upgrade of the ALICE Experiment: Letter Of Intent". In: J. Phys. G41, p. 087001. DOI: 10.1088/0954-3899/41/8/087001.

Abelev, B. (Sept. 2012). ALICE, "Strangeness with ALICE: from pp to Pb-Pb". In: PLHC2012: Physics at arXiv: 1209.3285 [nucl-ex].

Aberle, O. et al. (2020). "High-Luminosity Large Hadron Collider (HL-LHC): Technical design report". CERN Yellow Reports: Monographs. Geneva: CERN. DOI: 10.23731/CYRM-2020-0010. URL: https://cds.cern.ch/record/2749422.

Abreu, M. C. et al. (Feb. 2000). NA50 Collaboration, "Evidence for Deconfinement of Quarks and Gluons from the J/ψ Suppression Pattern Measured in $Pb - Pb$ Collisions at the CERN SPS". In: Phys. Lett. B 477, 28–36. 18 p. DOI: 10.1016/S0370-2693(00)00237-9. URL: https://cds.cern.ch/record/427590.

Acharya, S. et al. (Aug. 2018). ALICE Collaboration, "Centrality determination in heavy ion collisions." In: URL: https://cds.cern.ch/record/2636623.

Acharya, S. et al. (2019). ALICE, "Multiplicity dependence of light-flavor hadron production in pp collisions at $\sqrt{s} = 7$ TeV". In: <u>Phys. Rev. C</u> 99.2, p. 024906. DOI: `10.1103/PhysRevC.99.024906`. arXiv: `1807.11321 [nucl-ex]`.

Adam, J. et al. (2017). ALICE Collaboration, "Enhanced production of multi-strange hadrons in high-multiplicity proton-proton collisions". In: <u>Nature Phys.</u> 13, pp. 535–539. DOI: `10.1038/nphys4111`. arXiv: `1606.07424 [nucl-ex]`.

Adcox, K. et al. (Dec. 2001). "Suppression of Hadrons with Large Transverse Momentum in Central $Au + Au$ Collisions at $\sqrt{s_{\mathrm{NN}}} = 130$GeV". In: <u>Physical Review Letters</u> 88.2. DOI: `10.1103/physrevlett.88.022301`. URL: `https://doi.org/10.1103%2Fphysrevlett.88.022301`.

Agostinelli, S. et al. (2003). GEANT4, "GEANT4–a simulation toolkit". In: <u>Nucl. Instrum. Meth. A</u> 506, pp. 250–303. DOI: `10.1016/S0168-9002(03)01368-8`.

Alemany-Fernández, R. et al., eds. (2009). "LHC Workshop on Experimental Conditions and Beam-Induced Detectors Backgrounds: CERN, Geneva, Switzerland 3 - 4 Apr 2008. LHC Workshop on Experimental Conditions and Beam-Induced Detectors Backgrounds". CERN. Geneva: CERN. DOI: `10.5170/CERN-2009-003`. URL: `http://cds.cern.ch/record/1184436`.

Alme, J. et al. (2010). "The ALICE TPC, a large 3-dimensional tracking device with fast readout for ultra-high multiplicity events". In: <u>Nucl. Instrum. Meth.</u> A622, pp. 316–367. DOI: `10.1016/j.nima.2010.04.042`. arXiv: `1001.1950 [physics.ins-det]`.

Andronic, A. et al. (Sept. 2018a). "Decoding the phase structure of QCD via particle production at high energy". In: <u>Nature</u> 561.7723, pp. 321–330. DOI: `10.1038/s41586-018-0491-6`. URL: `https://doi.org/10.1038%2Fs41586-018-0491-6`.

— (2018b). "Decoding the phase structure of QCD via particle production at high energy". In: <u>Nature</u> 561.7723, pp. 321–330. DOI: `10.1038/s41586-018-0491-6`. arXiv: `1710.09425 [nucl-th]`.

Barlow, R. (2000). "SLUO Lectures on Statistics and Numerical Methods in HEP, Lecture 5: Systematic Errors". `https://www-group.slac.stanford.edu/sluo/Lectures/stat_lecture_files/sluolec5.pdf`. Available via BaBar Statistics Working Group web page.

Bazavov, A. et al. (2019). HotQCD, "Chiral crossover in QCD at zero and non-zero chemical potentials". In: <u>Phys. Lett. B</u> 795, pp. 15–21. DOI: `10.1016/j.physletb.2019.05.013`. arXiv: `1812.08235 [hep-lat]`.

Betev, L. and P. Chochula (2003). "Definition of the ALICE coordinate system and basic rules for sub-detector components numbering". In: URL: `https://edms.cern.ch/ui/file/406391/2/ALICE-INT-2003-038.pdf`.

Bhasin, A. and M. Sharma (Oct. 2022). ALICE, "Strangeness production in small-collision systems with ALICE". In: <u>51st International Symposium on Multiparticle Dynamics</u>. arXiv: `2210.08236 [hep-ex]`.

Bierlich, C. et al. (2022). "A comprehensive guide to the physics and usage of PYTHIA 8.3". DOI: 10.48550/ARXIV.2203.11601. URL: https://arxiv.org/abs/2203.11601.

Billoir, P. (1984). "Track Fitting With Multiple Scattering: A New Method". In: Nucl. Instrum. Meth. A 225, pp. 352–366. DOI: 10.1016/0167-5087(84)90274-6.

Brüning, O. S. et al. (2004). "LHC Design Report". CERN Yellow Reports: Monographs. Geneva: CERN. DOI: 10.5170/CERN-2004-003-V-1. URL: https://cds.cern.ch/record/782076.

Buncic, P. et al. (2015). "Technical Design Report for the Upgrade of the Online-Offline Computing System". In.

Busza, W., K. Rajagopal, and W. van der Schee (2018). "Heavy Ion Collisions: The Big Picture and the Big Questions". In: Annual Review of Nuclear and Particle Science 68.1, pp. 339–376. DOI: 10.1146/annurev-nucl-101917-020852. eprint: https://doi.org/10.1146/annurev-nucl-101917-020852. URL: https://doi.org/10.1146/annurev-nucl-101917-020852.

Caron, J.-L. (1993). "Diagram of LHC injection accelerator complex". AC Collection. Legacy of AC. Pictures from 1992 to 2002. URL: https://cds.cern.ch/record/841568.

— (May 1998). "Overall view of LHC experiments.. Vue d'ensemble des experiences du LHC." AC Collection. Legacy of AC. Pictures from 1992 to 2002. URL: http://cds.cern.ch/record/841555.

Cohen-Tannoudji, C., B. Diu, and F. Laloë (1977). "Quantum mechanics". Trans. of : Mécanique quantique. Paris : Hermann, 1973. New York, NY: Wiley. URL: https://cds.cern.ch/record/101367.

Colella, D. (Nov. 2020). ALICE Collaboration, "ALICE ITS Upgrade for LHC Run 3: Commissioning in the Laboratory". In: JPS Conf. Proc. 34. 8 pages, 5 figures, proceedings at The 29th International Workshop on Vertex Detectors (VERTEX) held virtually on October 5th-8th 2020, 010004. 8 p. DOI: 10.7566/JPSCP.34.010004. arXiv: 2012.01564. URL: https://cds.cern.ch/record/2746554.

Collins, J. C. and M. J. Perry (May 1975). "Superdense Matter: Neutrons or Asymptotically Free Quarks?" In: Phys. Rev. Lett. 34 (21), pp. 1353–1356. DOI: 10.1103/PhysRevLett.34.1353. URL: https://link.aps.org/doi/10.1103/PhysRevLett.34.1353.

Collins, J. (1997). "Light-cone Variables, Rapidity and All That". DOI: 10.48550/ARXIV.HEP-PH/9705393. URL: https://arxiv.org/abs/hep-ph/9705393.

Coupard, J. et al. (Apr. 2016). "LHC Injectors Upgrade, Technical Design Report: v.2: Ions". In.

Cui, P. (2022). ALICE, "Production of strange hadrons in jets and underlying events in pp and p–Pb collisions with ALICE". In: Phys. Scripta 97.5, p. 054009. DOI: 10.1088/1402-4896/ac5e59. arXiv: 2201.12578 [hep-ex].

Damerau, H. et al. (2014). "LHC Injectors Upgrade, Technical Design Report: v.1: Protons". In: ed. by H. Damerau et al. DOI: 10.17181/CERN.7NHR.6HGC.

Efthymiopoulos, I. et al. (2021). "Bunch Luminosity Variations in LHC Run 2". In: JACoW IPAC2021, pp. 4094–4097. DOI: 10.18429/JACoW-IPAC2021-THPAB172.

Eulisse, M. R. G. et al. (Nov. 2018). "AliceO2Group/AliceO2: First stable release". Version O2-1.0.0. DOI: 10.5281/zenodo.1493333. URL: https://doi.org/10.5281/zenodo.1493333.

Fini, P. b. R. A. et al. (2001). WA97 Collaboration, "Strange baryon production in Pb Pb collisions at 158-A-GeV/c". In: J. Phys. G 27. Ed. by G. Odyniec, pp. 375–381. DOI: 10.1088/0954-3899/27/3/315.

Greensite, J. (2011). "An introduction to the confinement problem". Vol. 821. DOI: 10.1007/978-3-642-14382-3.

Griffiths, D. (2008). "Introduction to elementary particles". ISBN: 978-3-527-40601-2.

Gupta, M. (July 2010). "Calculation of radiation length in materials". Tech. rep. Geneva: CERN. URL: https://cds.cern.ch/record/1279627.

Hanratty, L. D. (2014). "Λ and K_S^0 production in Pb-Pb and pp collisions with ALICE at the LHC". PhD thesis. Birmingham U.

Heinz, U. and M. Jacob (2000). "Evidence for a New State of Matter: An Assessment of the Results from the CERN Lead Beam Programme". DOI: 10.48550/ARXIV.NUCL-TH/0002042. URL: https://arxiv.org/abs/nucl-th/0002042.

Heinz, U. W. (Dec. 2005). "'RHIC serves the perfect fluid': Hydrodynamic flow of the QGP". In: Workshop on Extreme QCD, pp. 3–12. arXiv: nucl-th/0512051.

Herr, W. and B. Muratori (2006). "Concept of luminosity". In: DOI: 10.5170/CERN-2006-002.361. URL: https://cds.cern.ch/record/941318.

Koch, P. and J. Rafelski (1985). "Time evolution of strange-particle densities in hot hadronic matter". In: Nuclear Physics A 444.4, pp. 678–691. ISSN: 0375-9474. DOI: https://doi.org/10.1016/0375-9474(85)90112-5. URL: https://www.sciencedirect.com/science/article/pii/0375947485901125.

Kushpil, S. (2020). "Commissioning of the upgraded ALICE Inner Tracking System". In: Nuclear Instruments and Methods in Physics Research Section A: Accelerators, Spectrometers, Dete 979, p. 164421. ISSN: 0168-9002. DOI: https://doi.org/10.1016/j.nima.2020.164421. URL: https://www.sciencedirect.com/science/article/pii/S0168900220308184.

Lange, J. S. (2004). "A Comparison Between An Ultra-Relativistic Au+Au Collision and the Primordial Universe". DOI: 10.48550/ARXIV.HEP-PH/0403104. URL: https://arxiv.org/abs/hep-ph/0403104.

Lippmann, C. (Mar. 2014). ALICE Collaboration, "Upgrade of the ALICE Time Projection Chamber". In.

Liu, J. (2022). ALICE Collaboration, "Performance of the ALICE upgraded inner tracking system". In: JINST 17.04, p. C04032. DOI: 10.1088/1748-0221/17/04/C04032.

Maevskaya, A. I. (2019). ALICE Collaboration, "Fast Interaction Trigger for the upgrade of the ALICE experiment at CERN: design and performance". In: EPJ Web Conf. 204. Ed. by S.

Bondarenko, V. Burov, and A. Malakhov, p. 11003. DOI: `10.1051/epjconf/201920411003`. arXiv: `1812.00594 [physics.ins-det]`.

Matsui, T. and H. Satz (1986). "J/ψ Suppression by Quark-Gluon Plasma Formation". In: Phys. Lett. B 178, pp. 416–422. DOI: `10.1016/0370-2693(86)91404-8`.

Melikyan, Y. A. et al. (2020). "Performance of the cost-effective Planacon ® MCP-PMTs in strong magnetic fields". In: Nucl. Instrum. Meth. A 983, p. 164591. DOI: `10.1016/j.nima.2020.164591`.

Noferini, F. (2018). ALICE Collaboration, "ALICE results from Run-1 and Run-2 and perspectives for Run-3 and Run-4". In: J. Phys. Conf. Ser. 1014.1, p. 012010. DOI: `10.1088/1742-6596/1014/1/012010`.

Papoulis, A. and S. U. Pillai (2002). "Probability, Random Variables, and Stochastic Processes". Fourth. Boston: McGraw Hill. URL: `http://www.worldcat.org/search?qt=worldcat_org_all&q=0071226613`.

Perkins, D. H. (2000). "Introduction to High Energy Physics". 4th ed. Cambridge University Press. DOI: `10.1017/CBO9780511809040`.

Podolanski, J. and R. Armenteros (1954). "III. Analysis of V-events". In: The London, Edinburgh, and Dub 45.360, pp. 13–30. DOI: `10.1080/14786440108520416`. eprint: `https://doi.org/10.1080/14786440108520416`. URL: `https://doi.org/10.1080/14786440108520416`.

Rafelski, J. (Jan. 2020). "Discovery of Quark-Gluon Plasma: Strangeness Diaries". In: The European Physic 229.1, pp. 1–140. DOI: `10.1140/epjst/e2019-900263-x`. URL: `https://doi.org/10.1140%2Fepjst%2Fe2019-900263-x`.

Rafelski, J. and B. Muller (1982). "Strangeness Production in the Quark - Gluon Plasma". In: Phys. Rev. Lett. 48. [Erratum: Phys.Rev.Lett. 56, 2334 (1986)], p. 1066. DOI: `10.1103/PhysRevLett.48.1066`.

Rodríguez, P. B. et al. (2021). "Calibration of the momentum scale of a particle physics detector using the Armenteros-Podolanski plot". In: JINST 16.06, P06036. DOI: `10.1088/1748-0221/16/06/P06036`. arXiv: `2012.03620 [physics.ins-det]`.

Rohr, D. et al. (Nov. 2018). ALICE Collaboration, "Track Reconstruction in the ALICE TPC using GPUs for LHC Run 3". In: 4th International Workshop Connecting The Dots 2018. arXiv: `1811.11481 [physics.ins-det]`.

Rojas Torres, S. (2021). ALICE Collaboration, "The Forward Diffractive Detector for ALICE". In: PoS LHCP2020, 221. 4 p. DOI: `10.22323/1.382.0221`. URL: `http://cds.cern.ch/record/2773642`.

— (2022). ALICE Collaboration, "Status of the Fast Interaction Trigger detector for the ALICE upgrade". In: PoS EPS-HEP2021, p. 795. DOI: `10.22323/1.398.0795`.

Sauli, F. (Feb. 1997). "GEM: A new concept for electron amplification in gas detectors". In: Nuclear Instruments and Methods in Physics Research Section A: Accelerators, Spectrometers, Dete 386.2-3, pp. 531–534. DOI: `10.1016/s0168-9002(96)01172-2`. URL: `https://doi.org/10.1016/s0168-9002(96)01172-2`.

Shahoyan, R. (2022a). "AliceO2 - DCA Fitter". https://github.com/AliceO2Group/AliceO2/blob/8a79977

— (2022b). "AliceO2 - Secondary Vertexer". `https://github.com/AliceO2Group/AliceO2/blob/8a79977a615de5909d89a6b8e4c414ec19e6c144/Detectors/Vertexing/src/SVertexer.cxx`. GitHub repository.

Shuryak, E. V. (Oct. 2004). "The QCD vacuum, hadrons and the superdense matter". Vol. 71. DOI: `10.1142/5367`.

Tanabashi, M. et al. (2018). Particle Data Group, "Review of Particle Physics". In: Phys. Rev. D98.3, p. 030001. DOI: `10.1103/PhysRevD.98.030001`.

Torrieri, G. (2004). "Statistical hadronization phenomenology in heavy ion collisions at SPS and RHIC energies". DOI: `10.48550/ARXIV.NUCL-TH/0405026`. URL: `https://arxiv.org/abs/nucl-th/0405026`.

Torrieri, G. and J. Rafelski (2001). "Search for QGP and thermal freeze-out of strange hadrons". In: New J. Phys. 3, p. 12. DOI: `10.1088/1367-2630/3/1/312`. arXiv: `hep-ph/0012102`.

Ullrich, T. and Z. Xu (2007). "Treatment of Errors in Efficiency Calculations". DOI: `10.48550/ARXIV.PHYSICS/0701199`. URL: `https://arxiv.org/abs/physics/0701199`.

Wilk, G. and Z. Włodarczyk (Mar. 2000). "Interpretation of the Nonextensivity Parameter q in Some Applications of Tsallis Statistics and Lévy Distributions". In: Phys. Rev. Lett. 84 (13), pp. 2770–2773. DOI: `10.1103/PhysRevLett.84.2770`. URL: `https://link.aps.org/doi/10.1103/PhysRevLett.84.2770`.

I – Appendix A - Signal extraction fits

Figure A.1: Fits (red line) of the invariant mass distributions (black data points) of K_S^0 measured over the p_T bins used for the analysis
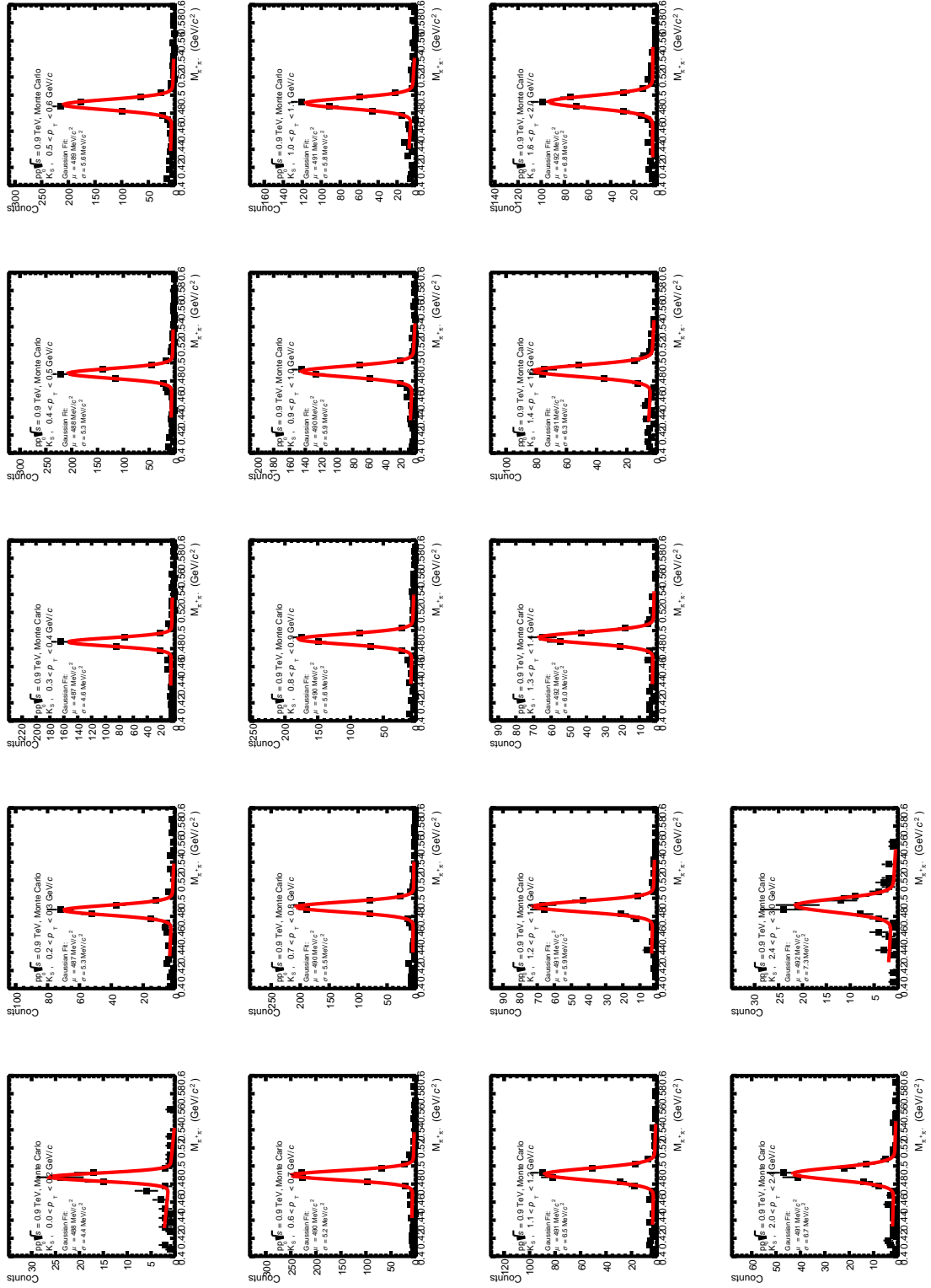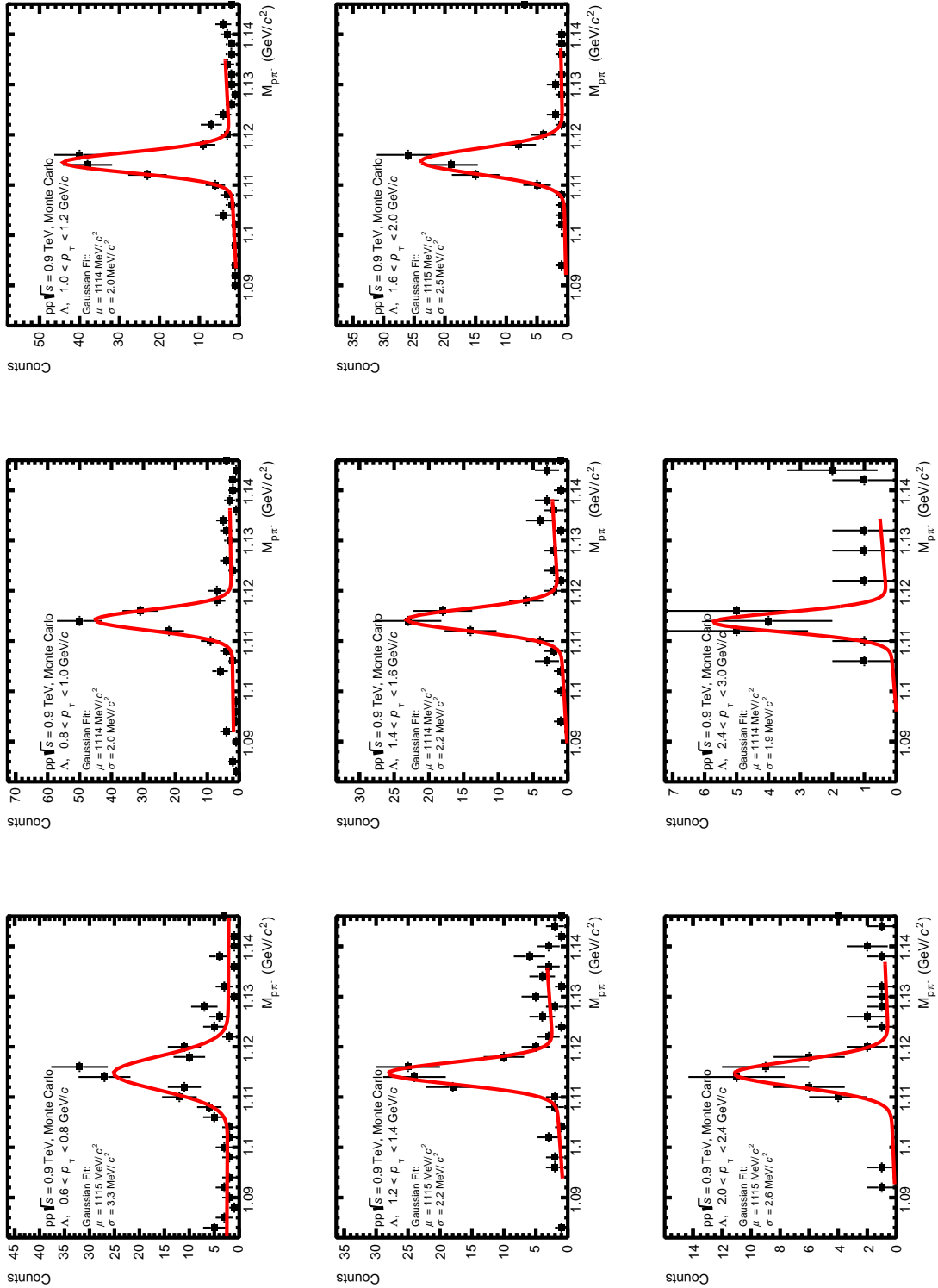
Figure A.2: Fits (red line) of the invariant mass distributions (black data points) of Λ measured over the p_{T} bins used for the analysis

Figure A.3: Fits (red line) of the invariant mass distributions (black data points) of $\overline{\Lambda}$ measured over the p_{T} bins used for the analysis

II − Appendix B - Software details

The analysis of the AO2D produced by the reconstruction process is done with the O2Physics package, version nightly-20220715. O2Physics is a framework for the analysers that hides most of the complexity and makes writing an analysis task easier. In this framework an analysis task is created by the combination of workflows. Those workflows subscribe to various tables saved in the AO2D (see section 2.3) or created by other workflows, and produce new tables or histograms that are saved in a .root file. Those files can be read using the ROOT framework, used by CERN and many (particle) physics experiments for data processing.

The workflow used is as follows:

```
o2-analysis-lf-lambdakzerobuilder -b --configuration json://MyJson.json \
| o2-analysis-event-selection -b --configuration json://MyJson.json \
| o2-analysis-timestamp -b --configuration json://MyJson.json \
| o2-analysis-trackextension -b --configuration json://MyJson.json \
| o2-analysis-lf-lambdakzeroanalysis-mc -b --configuration json://MyJson.json \
| o2-analysis-pid-tpc -b --configuration json://MyJson.json \
| o2-analysis-multiplicity-table -b --configuration json://MyJson.json \
| o2-analysis-fdd-converter -b --configuration json://MyJson.json
```

where MyJson.json is a configuration text file detailed at the end of this appendix.

The plots presented in section 3.2 have been made using my own post processing code, reading the histograms filled by the analysis and calculating the various quantities (spectra, efficiencies, uncertainties, etc ...). They have been written using the ROOT framework.

MyJson.json file

```
{
    "internal-dpl-clock": "",
    "internal-dpl-aod-reader": "",
    "internal-dpl-aod-spawner": "",
    "fdd-converter": "",
    "timestamp-task": {
        "verbose": "false",
        "rct-path": "RCT\/RunInformation\/",
```

```
        "orbit-reset-path": "CTP\/Calib\/OrbitReset",
        "ccdb-url": "http:\/\/alice-ccdb.cern.ch",
        "isRun2MC": "false"
    },
    "internal-dpl-aod-index-builder": "",
    "track-extension": "",
    "lambdakzero-builder": {
        "dcanegtopv": "0.1",
        "dcapostopv": "0.1",
        "mincrossedrows": "70",
        "isRun2": "0",
        "d_bz": "-999",
        "v0cospa": "0.97",
        "dcav0dau": "1",
        "v0radius": "0.5",
        "useMatCorrType": "1",
        "rejDiffCollTracks": "0",
        "processRun2": "true",
        "processRun3": "false"
    },
    "bc-selection-task": {
        "processRun2": "false",
        "processRun3": "true"
    },
    "event-selection-task": {
        "syst": "pp",
        "muonSelection": "0",
        "customDeltaBC": "300",
        "isMC": "true",
        "processRun2": "false",
        "processRun3": "true"
    },
    "lambdakzero-initializer": "",
    "multiplicity-table": {
        "doVertexZeq": "1",
        "processRun2": "false",
        "processRun3": "true"
    },
    "lambdakzero-particle-count-mc": {
```

```json
        "rapidityMCcut": "0.75",
        "eventSelectionMC": "false",
        "eventSelectionMC_posZ": "true"
    },
    "tpc-pid": {
        "param-file": "",
        "ccdb-url": "http:\/\/alice-ccdb.cern.ch",
        "ccdbPath": "Analysis\/PID\/TPC\/Response",
        "ccdb-timestamp": "-1",
        "useNetworkCorrection": "false",
        "autofetchNetworks": "true",
        "networkPathLocally": "network.onnx",
        "enableNetworkOptimizations": "true",
        "networkPathCCDB": "Analysis\/PID\/TPC\/ML",
        "pid-el": "-1",
        "pid-mu": "-1",
        "pid-pi": "-1",
        "pid-ka": "-1",
        "pid-pr": "-1",
        "pid-de": "-1",
        "pid-tr": "-1",
        "pid-he": "-1",
        "pid-al": "-1"
    },
    "lambdakzero-analysis-mc": {
        "dca-binning": {
            "values": [
                "200",
                "0",
                "1"
            ]
        },
        "pt-binning": {
            "values": [
                "200",
                "0",
                "10"
            ]
        },
```

```
"K0S-mass-binning": {
    "values": [
        "400",
        "0.4",
        "0.6"
    ]
},
"Lambda-mass-binning": {
    "values": [
        "200",
        "1.015",
        "1.215"
    ]
},
"tpcRows-binning": {
    "values": [
        "200",
        "0",
        "200"
    ]
},
"v0cospa": "0.97",
"dcav0dau": "0.75",
"dcanegtopv": "0.1",
"dcapostopv": "0.1",
"v0radius": "0.5",
"rapidity": "0.75",
"saveDcaHist": "1",
"TpcPidNsigmaCut": "5",
"boolArmenterosCut": "false",
"paramArmenterosCut": "0.2",
"eventSelection": "false",
"eventSelection_posZ": "true",
"lifetimecut": {
    "labels_rows": "",
    "labels_cols": [
        "lifetimecutLambda",
        "lifetimecutK0S"
    ],
```

```
            "values": [
                [
                    "1000",
                    "1000"
                ]
            ]
        },
        "processRun3": "true",
        "processRun2": "false"
    },
    "lambdakzero-qa": "",
    "internal-dpl-aod-global-analysis-file-sink": "",
    "internal-dpl-aod-writer": ""
}
```

III – Request for ethical approval

Ethics ETH1920-1788: Mr Aimeric Landou

Date Created	10 Jan 2020
Date Submitted	11 Feb 2020
Date forwarded to committee	02 Mar 2020
Researcher	Mr Aimeric Landou
	Lee Barnby
Student ID	
Category	Postgraduate research student
	Researcher
Supervisor	Lee Barnby
Project	Strangeness reconstruction in the ALICE Run 3 continuous readout environment
College	College of Science and Engineering
Current status	Approved

Ethics application

Project information

Project title
Online reconstruction in the ALICE Run 3 continuous readout environment

What is the aim of your study?
Answer ALICE's need for an online analysis code in the upcoming continuous readout environment in RUN 3.

What are the objectives for your study?
- Develop then optimise using simulations a code for the reconstruction of tracks of daughter particles originated from V0 events in a continuous readout environment

- Develop a code to associate these particles to the correct initial collision events in this continuous readout environment

- Develop extension to algorithms for other decay topologies

- Test those codes with the first data of RUN 3

Are there any research partners (NOT including your supervisor) within the University of Derby involved in the project?
Lee Barnby

Are there any research partners external to the University of Derby involved in the project?
Yes

If yes, please provide details

ALICE

Initial screening

Does this project involve human participants?
No

If yes, should your research adhere to the British Psychology Society (BPS) code of ethics and conduct?

Does your study involve data collection with any persons who could be considered vulnerable (under 18 years or the elderly, or those with physical or mental disabilities)?
No

Does your project involve collecting data within NHS organisations or from any NHS employees or patients?
No

Does it involve collecting or analysing primary or unpublished data about people who have died, other than data that is already in the public domain?
No

Does your study involve direct access to an external organisation?
No

Does your study involve species not covered by the Animals Scientific Procedures Act (1993)?
No

Does your study involve ionising radiation?
No

Does your study involve the evaluation of medical devices, or the testing of medicinal and pharmaceutical products?
No

Does your study involve Her Majesty's Prison and Probation Service?
No

Does your study involve serving offenders, professionals who work with them, or questions relating to criminal offences?
No

Does your study involve a need to see, acquire or store material that could be viewed as illegal or that may attract the interest of the police, security or intelligence services?
No

Will your study have any impact on the natural or built environment?
No

Funding and previous applications

Has this research been funded by an external organisation (e.g. a research council or public sector body)?
No

If yes, please provide the name of funder:
College of Engineering and Technology

Has this research been funded internally?
Yes

Name of internal fund
College Internal Fund

Funding amount
14777

Term of funding
PGTA?

Date funding agreed
22 Nov 2018

Have you submitted previous requests for ethical approval to the Committee that relate to this research project?
No

If yes, please provide previous application reference:

Study

Brief review of relevant literature and rationale for study
Several signs of an unconventional state of matter have been spotted in multiple high-energy physics experiments before ALICE. The quark-gluon plasma, assumed to have existed in the very first instants of the universe, is a very interesting and peculiar state of matter, consisting in unconfined quarks and gluon interacting with each other in, as opposed to the bound state that are the norm in colder matter. This state can be reached in the few instants after a nuclei collision (1)

The study of this quark-gluon plasma was one of the main missions of ALICE, which probes matter through high-energy lead-lead collisions as well as proton-proton collisions for comparison with the former (2).

The experiment is now entering a phase of shutdown to allow for the upgrade of the detector. Run 3, the name of the period of activity ALICE will enter in 2021, will record collision events inside the Inner

Tracking system and the Time Particle Chamber at an increased rate of 50kHz, to be compared with the 500Hz rate in Run 2 (3). This will allow for the detection of rarer, more exotic decays, but also significantly increase the number of collision events recorded every second, to a point where an almost real-time processing of the data will be needed in order not to lose too many events worth of information, as would happen with the current offline analysis (4). Indeed, with an event representing roughly 20 Mbytes of data, storing every event for an offline analysis would require facilities that could handle 1TB/s of data flow accumulating over several years (3). Online reconstruction is needed in order to be able to compress the data of every event into a limited number of its most important features, for a later offline refined analysis.

Simultaneously to the online reconstruction, switching to a continuous readout from the current trigger method is necessary (3): reducing the dead-time in the detector is very important as the study of these decays require very large statistics, their signal-to-background ratio being very small. The trigger method currently in use has a lot of advantages in that it allows us to easily distinguish between two collision events. Unfortunately, this method introduces a lot of dead-time, and thus reduces the number of events actually seen. This is where the continuous readout environment steps in. The detector outputs are read continuously, regardless of the detection of the occurrence of an interaction.

Unfortunately, this makes it much more difficult to attribute a track or vertex to the collision event it originates from, where the trigger method made sure to capture only single collision events.

The reconstruction of primary tracks from collisions is known to be achievable, but there has been little work done on secondary tracks. One such kind of events are decays of neutral particles into two daughters with charges of opposite signs, called V0 events, with a very characteristic detector signature of two tracks of opposite curvature originating from the same point seemingly disconnected from any other track.

Cited references for any sources in the sections on rationale, methods etc.

1. The quest for the quark-gluon plasma. Braun-Munzinger, Peter et Stachel, Johanna. s.l. : Nature Publishing Group, 7 2007, Nature, Vol. 448, p. 302.

2. The ALICE experiment at the CERN LHC. Collaboration, The A. L. I. C. E., et al. s.l. : IOP Publishing, 8 2008, Journal of Instrumentation, Vol. 3, pp. S08002--S08002.

3. Upgrade of the ALICE Experiment: Letter Of Intent. B. Abelev. s.l. : IOP Publishing, 7 2014, Journal of Physics G: Nuclear and Particle Physics, Vol. 41, p. 087001.

4. Buncic, P., Krzewicki, M. et Vande Vyvre, P. Technical Design Report for the Upgrade of the Online-Offline Computing System. 2015. Tech. rep.

Outline of study design
Acquisition of data using the ALICE detector, and simulation of data using standard High Energy Physics tools.

Outline of study methods
Aanalysis of the data using standard High Energy Physics computing tools.

Do you propose to carry out your project partly in a non-English language?

No

If yes, please provide details

Ethical considerations

Research undertaken in public places
No

GDPR - collecting personal data
Not collecting personal data

Basis for collecting data
Not applicable (only use when no data is being collected)

Data retention
Not applicable

Rights of data subject
Not applicable

Commercial sensitivity
Not applicable - we have a Memorandum of Understanding

Are you using non-standard software to store or analyse data?
No

Are there other ethical implications that are additional to this list?
No

If yes, please provide details

Have/do you intend to request ethical approval from any other body/organisation?
No

If yes, please provide details

Do you intend to publish your research?
Yes

Have the activities associated with this research project been risk-assessed?
Yes

Attachments

Informed consent from other parties/organisations
Relevant testing materials

Other

Attached files

MoU_Associate_UniversityDerby.pdf

Memorandum of Understanding

for Collaboration in the ALICE Experiment

Associate Membership of

University of Derby

1. Introduction

1.1 In a letter addressed to Dr. P. Giubellino, Spokesperson of the ALICE Collaboration, the University of Derby, represented by Prof. Nikos Antonopoulos, expressed its wish to join the ALICE Collaboration.

1.2 As its particular field of interest, the University of Derby has chosen to collaborate to the software framework and applications of the O^2 project.

1.3 The purpose of this memorandum is to lay down the terms of collaboration between University of Derby and the ALICE Collaboration.

1.4 It is agreed by the Parties that this memorandum is not legally binding.

2. Approval of Collaboration

2.1 After due consideration of the contributions offered to ALICE, the scientific potential and the human resources available at the University of Derby, the ALICE Collaboration is welcoming the participation of the University of Derby, as a new collaborating institution.

2.2 The participation of the University of Derby, in the ALICE Collaboration has formally been approved by the Collaboration Board at its meeting on 26 June 2015 under the terms laid down in this document.

A Large Ion Collider Experiment

3.   Term and Terms of Collaboration

3.1 This memorandum of understanding shall remain in place until the 26th June 2020, unless terminated earlier by either Party, giving to the other no less than 6 months' notice.

3.2 The University of Derby is represented by Prof. Nikos Antonopoulos.

3.3 At the time of signing this document the following members of the University of Derby, are considered as members of the ALICE Collaboration:

- Prof. Nikos Antonopoulos (Team Leader, Senior Professor & Dean)

3.4 Duties and rights of Associate Membership in the ALICE Collaboration:

3.4.1 By becoming Associate Member of the ALICE Collaboration, the above listed members of the University of Derby are granted:

3.4.2 access to the internal ALICE documentation and software;

3.4.3 access to ALICE meetings;

3.4.4 access to ALICE scientific data;

3.4.5 certification for the use of the ALICE GRID for computing;

3.4.6 non-voting membership of the ALICE Collaboration Board for the team leader.

3.4.7 While in general ALICE members from Associate Institutions do not sign scientific papers, they can sign the ones to which they have given a substantial contribution.

XVIII

By becoming Associate Member to the ALICE Collaboration, the University of Derby engages itself to contributing to the activities of the collaboration. In particular, the University of Derby will contribute to the software framework and applications of the O^2 project.

4.   Signatures

Location, date

Prof. Nikos Antonopoulos   Dr. Paolo Giubellino

ALICE University of Derby Team Leader   Spokesperson, ALICE Collaboration

Mr. Hari Punchihewa

Deputy Chief Executive & Finance Director, University of Derby

Prof. Kathryn Mitchell

Vice-Chancellor, University of Derby

IV – Confirmation of ethical approval

Kedleston Road, Derby
DE22 1GB, UK

T: +44 (0)1332 591060
E: researchoffice@derby.ac.uk
Sponsor License No: QGN14R294

Dear Aimeric

ETH1920-1788

Thank you for submitting your application to the College of Engineering and Technology Research Ethics Committee, which has now been reviewed and considered.

The outcome of your application is:

approved.

Feedback on your application is available here.

If any changes to the study described in the application are necessary, you must notify the Committee and may be required to make a resubmission of the application.

On behalf of the Committee, we wish you the best of luck with your study.

Yours sincerely

Kam Beesla

Research Student Office

UNIVERSITY
of DERBY

derby.ac.uk